Synthesis and characterizations of defect-rich Martian regolith constituents

Dissertation

Zur Erlangung des Doktorgrades der Naturwissenschaften
-Dr. rer. nat.-

Fachbereich 02 (Biologie/Chemie)
Der Universität Bremen

Vorgelegt von

M.Sc. Muchammad Izzuddin Jundullah Hanafi

Bremen, Dezember 2024

Diese Arbeit wurde in der Arbeitsgruppe „Chemische Kristallographie fester Stoffe“ von Herrn Prof. Dr. Thorsten M. Gesing an der Universität Bremen im Zeitraum von Dezember 2020 bis September 2024 angefertigt.

Begutachtung des schriftlichen Teils:

1. Gutachter: Prof. Dr. Holger Kohlmann, Universität Leipzig

2. Gutachter: Prof. Dr. Ronald Miletich-Pawliczek, Universität Wien

Begutachtung des schriftlichen Teils: Abgabe 30.09.2024

Datum der Verteidigung: 12.12.2024

Mitglieder des Prüfungsausschusses:

1. Prof. Dr. Tim Neudecker, Fachbereich 02 Biologie/Chemie, Institut für Physikalische und Theoretische Chemie, Universität Bremen
2. Prof. Dr. Thorsten M. Gesing, Fachbereich 02 Biologie/Chemie, Institut für Anorganische Chemie und Kristallographie, Chemische Kristallographie fester Stoffe, Universität Bremen
3. Prof. Dr.-Ing. Lucio Colombi Ciacchi, Fachbereich 04 Produktionstechnik -Maschinenbau & Verfahrenstechnik-, Hybrid Materials Interfaces Group, Universität Bremen
4. Prof. Dr. Ella Schmidt, Fachbereich 05 Geowissenschaften, Fachgebiet Kristallographie und Geomaterialforschung, Universität Bremen
5. PD Dr. Michael Fischer, Fachbereich 05 Geowissenschaften, Fachgebiet Kristallographie und Geomaterialforschung, Universität Bremen
6. B.Sc. Moritz Hornig, Fachbereich 02 Biologie und Chemie, Masterstudent, Universität Bremen

Erklärungen

Versicherung des Eides Statt

Hiermit versichere ich, Muchammad Izzuddin Jundullah Hanafi

An Eides statt durch meine Unterschrift, dass ich die vorliegende Arbeit mit dem Titel „Synthesis and characterizations of defect-rich Martian regolith constituents“ selbstständig und ohne fremde Hilfe angefertigt und alle Stellen, die ich wörtlich dem Sinne nach aus Veröffentlichungen entnommen habe, als solche kenntlich gemacht habe, mich auch keiner anderen als der angegebenen Literatur oder sonstiger Hilfsmittel bedient habe.

Ich versichere an Eides statt, dass ich die vorgenannten Angaben nach bestem Wissen und Gewissen gemacht habe und dass die Angaben der Wahrheit entsprechen und ich nichts verschwiegen habe.

Die Strafbarkeit einer falschen eidesstattlichen Versicherung ist mit bekannt, namentlich die Strafanordnung gemäß § 156 StGB bis zu drei Jahren Freiheitsstrafe oder Geldstrafe bei vorsätzlicher Begehung der Tat bzw. gemäß § 161 Abs. 1 StGB bis zu einem Jahr Freiheitsstrafe oder Geldstrafe bei fahrlässiger Begehung.

Muchammad Izzuddin Jundullah Hanafi Bremen, 30.09.2024

Acknowledgements

First of all, I would like to thank my supervisor, Prof. Dr. Thorsten M. Gesing for the opportunity to work in his group and valuable supports and suggestions throughout the research. Many thanks to Prof. Dr. M. Mangir Murshed and Dr. Lars Robben for guidance and inspiring discussions to improve my manuscripts. I am also grateful to Mrs. Gabriele Ebert and Mrs. Isabelle de Bloom for their kind help during my PhD time.

I am honored that Prof. Dr. Holger Kohlmann from University of Leipzig and Prof. Dr. Ronald Miletich-Pawliczek from University of Vienna are willing to serve as the reviewer of my dissertation. I appreciate their time and suggestions for improving my dissertation.

I thank everyone who is involved in the collaboration works, Prof. Dr.-Ing. Lucio Colombi Ciacchi and Dr. Wilke Dononelli (HMI, University of Bremen), Prof. Dr. Nicola Marzari (Excellence Chair University of Bremen) and his PhD student Lorenzo Bastonero, as well as Dr. Andrea Kirsch (University of Copenhagen).

I would also like to thank all my colleagues from AG Gesing for the discussions, cooperation, and a good working atmosphere. Special thanks to everyone for having lots of fun together and also being helpful in my non-scientific issues.

I would like to express my gratitude to the state of Bremen for financial support within the “Humans on Mars” initiative for APF “Materials on demand” S1P3. Thank you to the University of Bremen for their financial support for conference trips (DGK 2022, DGK 2023).

Last but not the least, I am grateful to my parents and family for keep encouraging me, in particular, my beloved wife and the little one who always cheer me up unconditionally. Thank you to all my friends and Indonesian Muslim Community in Bremen who have provided a good place to fulfill spiritual needs and maintain the inner peace.

Declaration on the contribution of the candidate to a multi-author article/manuscript which is included as a chapter in the submitted doctoral thesis

Chapter 3:

Contribution of the candidate in % of the total workload (up to 100 % for each of the following categories):

Experimental concept and design: ca. 80 %
Experimental work and/or acquisition of (experimental) data: ca. 100 %
Data analysis and interpretation: ca. 80 %
Preparation of Figures and Tables: ca. 90 %
Drafting of the manuscript: ca. 75 %

Chapter 4:

Contribution of the candidate in % of the total workload (up to 100 % for each of the following categories):

Experimental concept and design: ca. 80 %
Experimental work and/or acquisition of (experimental) data: ca. 85 %
Data analysis and interpretation: ca. 70 %
Preparation of Figures and Tables: ca. 90 %
Drafting of the manuscript: ca. 70 %

Chapter 5:

Contribution of the candidate in % of the total workload (up to 100 % for each of the following categories):

Experimental concept and design: ca. 80 %
Experimental work and/or acquisition of (experimental) data: ca. 90 %
Data analysis and interpretation: ca. 75 %
Preparation of Figures and Tables: ca. 100 %
Drafting of the manuscript: ca. 75 %

Date: 30.09.2024

Detail of the declaration on own contributions to the publications

The previously published work which is presented in **chapter 3** (Mg-Fe Olivine) is divided in the following parts where I conducted:

- Synthesis of Mg-Fe olivine solid solution
- Measurements of XRPD, Raman, and UV/Vis spectroscopy. Additionally, the data evaluation and interpretation, the structural determination and refinements
- Writing of the main manuscript (in cooperation with Prof. Dr. Thorsten M. Gesing, Prof. Dr. Mangir Murshed, and Dr. Lars Robben)
- Generation of the figures

The previously published work which is presented in **chapter 4** (defective forsterite) is divided in the following parts where I conducted:

- Synthesis of different forsterites
- Measurements of XRPD and Raman spectroscopy. Additionally, the data evaluation and interpretation, the structural determination and refinements
- Writing of the main manuscript (in cooperation with Prof. Dr. Thorsten M. Gesing, Prof. Dr. Mangir Murshed, Dr. Lars Robben, Lorenzo Bastonero, Dr. Wilke Dononelli, and Dr. Andrea Kirsch (University of Copenhagen))
- Generation of the figures

And parts where I did not conduct:

- X-ray synchrotron total scattering measurements (Dr. Andrea Kirsch, University of Copenhagen)
- Generate initial script for DFT-PDF optimization (Dr. Wilke Dononelli)
- Formation energy and theoretical Raman calculations (Lorenzo Bastonero)

The previously published work which is presented in **chapter 5** (Plagioclase feldpsar) is divided in the following parts where I conducted:

- Synthesis of plagioclase-type phases
- Measurements of SEM/EDX, XRPD, and Raman spectroscopy. Additionally, the data evaluation and interpretation, the structural determination and refinements
- Writing of the main manuscript (in cooperation with Prof. Dr. Thorsten M. Gesing, Prof. Dr. Mangir Murshed, and Dr. Lars Robben)
- Generation of the figures

And parts where I did not conduct:

- XRPD measurements on Stadi MP (Dr. Lars Robben and Konrad Krämer)

Table of content

Publications

[1] A. Kvaratskheliya, A. Filimonov, B. Bianchini, **M.I. Jundullah Hanafi**, T.M. Gesing, T. Sasaki, P. Gargarella, L. Mädler, I. Okulov, "Making Parts on Mars: Laser processing of iron contaminated by regolith", *Materials Today Advances* (2024, submitted)

[2] R. Fayaz, F. La Mantia, M. Baune, A. Carissimo, G. Pillot, **M.I. Jundullah Hanafi**, T.M. Gesing, S. Kerzenmcher, J. Thöming, "Electrochemical Iron Recovery from Biologically Produced Magnetite via Iron Oxide/Hydroxide Conversion: First Steps towards Terrestrial and Martian Applications", *Scientific Reports* (2024, submitted)

[3] **M.I. Jundullah Hanafi**, L. Bastonero, M.M. Murshed, L. Robben, W. Dononelli, A. Kirsch, N. Marzari, T.M. Gesing, "Synthesis, structural and spectroscopic characterization of defect-rich forsterite as representative phase of Martian regolith", *IUCrJ* (2024, under review)

[4] **M.I. Jundullah Hanafi**, M.M. Murshed, L. Robben, T.M. Gesing, "Mechanochemical synthesis of $(Mg_{1-x}Fe_x)_2SiO_4$ olivine phases relevant to Martian regolith: structural and spectroscopic characterizations", *Zeitschrift für Kristallographie - Crystalline Materials* 239 (2024) 1-11. DOI:10.1515/zkri-2024-0078

[5] K. Kulkarni, M. Fabien Franke, **M.I. Jundullah Hanafi**, T.M. Gesing, P. Zabel, "Optimizing lunar regolith beneficiation for ilmenite enrichment", *Frontiers in Space Technologies* 4 (2024) 1328341. DOI:10.3389/frspt.2023.1328341

[6] R. Fayaz, I. Bösing, F. La Mantia, M. Baune, **M.I. Jundullah Hanafi**, T.M. Gesing, J. Thöming, "Deoxidation Electrolysis of Hematite in Alkaline Solution: Impact of Cell Configuration and Process Parameters on Reduction Efficiency", *ChemElectroChem* 10(22) (2023) e202300451. DOI:10.1002/celc.202300451

List of abbreviations

ACS	average crystallite size
ADP	atomic displacement parameters
ASE	atomistic simulation environment
BM	ball mill
BVS	bond valence sum
CFO	crushed forsterite
CFSE	crystal field stabilization energy
CSD	crystallite size distribution
DASF	derivation of absorption spectrum fitting
DC	degree of crystallinity
DFT	density functional theory
EDX	energy dispersive X-ray
FWHM	full-width at half-maximum
GGA	generalized gradient approximation
GOSWD	geometry-optimized structure without defects
HFO	healed forsterite
LCS	log-normal crystallite size
MSL	Mars science laboratory
MGS-1	Mars global simulant
MOACS	maximum observable average crystallite size
PBC	periodic boundary conditions
PBE	Perdew–Burke–Ernzerhof functional
PDF	pair distribution function
PES	potential energy surface

PFO	pristine forsterite
RATD	reflectance – absorbance – Tauc – DASF
RFO	RSC synthesized forsterite
RSC	reverse strike co-precipitation
SEM	scanning electron microscopy
SOF	site occupancy factor
TEOS	tetraethyl orthosilicate
UV/Vis	ultra-violet/ visible
WC	tungsten carbide
wt-%	weight percentage
XRPD	X-ray powder diffraction

Thesis structure

This dissertation is submitted as cumulative research work based on three manuscripts. At the time this thesis was handed in at the University of Bremen, the first manuscript was already published (DOI:10.1515/zkri-2024-0078). The second manuscript was submitted to IUCrJ and currently under review, while the third manuscript is in preparation. **Chapter 1** introduces the general motivation of this research, Martian regolith phase constituents, and a review of their crystal structure as well as the reported synthesis techniques. **Chapter 2** refers to the experimental methods used for synthesis, characterizations, and the associated instrumental setups. **Chapter 3** introduces the synthesis and characterizations of $(Mg_{1-x}Fe_x)_2SiO_4$ olivine solid solution (DOI:10.1515/zkri-2024-0078). **Chapter 4** focuses on the structural differences between defect-rich and defect-poor forsterite (Mg_2SiO_4) endmember. **Chapter 5** describes the synthesis and characterizations of plagioclase feldspars $(Ca_{1-x}Na_x)(Al_{2-x}Si_{2+x})O_8$: mechanical weathering relevant to Martian regolith. **Chapter 6** concludes the PhD work with a short outlook. Respective cited references are presented at the end of each chapter.

Summary

Martian regolith draws intensive research attention for the future human settlement on Mars. Its defect-rich and highly concentrated amorphous features were present due to long-lasting space weathering by the solar wind radiation and mechanical impact from extraterrestrial objects. Within the frame of in-situ resource utilization, fundamental knowledge of the structures of the phase constituents and their defect variants are of critical importance. In contrast to naturally occurring minerals, the usage of laboratory synthesized samples has an advantage of providing pure, single-phase materials. This doctoral thesis focuses on the synthesis and characterization of olivines and plagioclase feldspars as representative major phases in Martian regolith. In addition, the impact of mechanical weathering using high-energy ball mill on selective synthesized phases are investigated here.

Mechanochemical synthesis of the complete $(Mg_{1-x}Fe_x)_2SiO_4$ olivine solid solution was carried out (**Chapter 3**) to cover the wide range of olivine composition on Mars. The synthesized olivines exhibit degrees of crystallinity (DC) of 92 wt.-% – 97 wt.-%, suggesting relatively low amount of the amorphous scattering contents. Olivines with higher Fe content (x = 0.5 - 1) are likely to form larger crystallites (> 150 nm). Substitution of Mg with Fe on the $M1$-site ($4a$: 0,0,0) is preferred against the as well octahedrally coordinated $M2$-site ($4c$: $x,y,\frac{1}{4}$). Regression equations are demonstrated based on the X-ray reflection intensity and characteristic Raman modes for easy calculation of Mg/Fe-concentration in Martian olivines.

Chapter 4 focuses on the structural differences between defect-rich and defect-poor forsterite (Mg_2SiO_4) endmember. The defect-rich forsterite is obtained by mechanical weathering using a ball mill. Implementing PDF-Rietveld refinements on X-ray synchrotron data indicated a complex disorder structure in the defect-rich forsterite. Raman peaks broadening and global red-shifts complemented the structural features of the defective phases. The defect-rich structural motifs are deduced by density functional theory assisted pair distribution function

(DFT-PDF) refinements. DFT-PDF refinements indicate that post-processed forsterite contains Mg Frenkel-type and Mg^{2+} interstitial defects with concentrations of 23(3) and 10(3) wt.-%, respectively. DFT calculations confirmed that the defective structure models are energetically stable.

A series of $(Ca_{1-x}Na_x)(Al_{2-x}Si_{2+x})O_8$ plagioclase feldspars are synthesized using conventional solid-state method with subsequent calcination schemes (**Chapter 5**). The bulk chemical compositions obtained from energy dispersive X-ray spectroscopy has been served for Al/Si ratio in the sample. The synthesized plagioclase feldspars exhibit DC of 73 wt.-% – 84 wt.-%, suggesting substantial amount of the amorphous scattering contents. Selective plagioclase feldspar members (x = 0, 0.4 and 1) were mechanically weathered using a ball mill. Implementing PDF-Rietveld refinements on Mo X-ray data indicates disorder structure, in particular of post-milled albite endmember. Raman peaks broadening and frequency shifts again complemented the structural features of the defective phases.

Zusammenfassung

Mars-Regolith weckt im Hinblick auf die zukünftige menschliche Besiedlung des Mars intensives Forschungsinteresse. Seine defektreichen Kristallstrukturen in Verbindung mit hohen amorphen Anteilen sind auf die langanhaltende Weltraumverwitterung durch Sonnenwindstrahlung und die mechanische Einwirkunge durch interstellare Objekte zurückzuführen. Aus Sicht einer In-situ-Ressourcennutzung sind grundlegende Kenntnisse über die Strukturen der Phasenbestandteile und ihre Defektvarianten von entscheidender Bedeutung. Im Gegensatz zu natürlich vorkommenden Mineralien hat die Verwendung von im Labor synthetisierten Proben den Vorteil, reine, einphasige Materialien zu liefern. Diese Doktorarbeit konzentriert sich auf die Synthese und Charakterisierung von Olivinen und Plagioklas-Feldspaten als repräsentative Hauptphasen im Mars-Regolith. Darüber hinaus werden die Auswirkungen der mechanischen Verwitterung mit Hochenergie-Kugelmühlen auf selektiv synthetisierte Phasen untersucht.

Es wurde eine mechanochemische Synthese der vollständigen $(Mg_{1-x}Fe_x)_2SiO_4$ Olivin festen Lösung durchgeführt (**Kapitel 3**), um das breite Spektrum der Olivinzusammensetzung auf dem Mars abzudecken. Die synthetisierten Olivine weisen einen Grad der Kristallinität (DC) von 92 Gew.-% – 97 Gew.-% auf, was auf einen relativ geringen Anteil amorpher Streuanteile schließen lässt. Olivine mit höherem Fe-Gehalt (x = 0,5 - 1) bilden dabei offensichtlich größere Kristallite (> 150 nm). Die Substitution von Mg durch Fe auf der *M*1-Position (4*a*: 0,0,0) ist gegenüber der ebenfalls oktaedrisch koordinierten *M*2-Position (4*c*: *x*,*y*,¼) bevorzugt. Regressionsgleichungen werden auf Grundlage der Röntgenreflexionsintensität und charakteristischen Raman-Moden zur einfachen Berechnung der Mg/Fe-Konzentration in Mars-Olivinen abgeleitet.

Kapitel 4 konzentriert sich auf die strukturellen Unterschiede zwischen defektreichen und defektarmen Forsterit-Endgliedern (Mg_2SiO_4). Der defektreiche Forsterit wird durch

mechanische Verwitterung in einer Kugelmühle gewonnen. Die Implementierung von PDF-Rietveld-Verfeinerungen an Röntgen-Synchrotron-Daten deutete auf eine komplexe Unordnungsstruktur im defektreichen Forsterit hin. Die Verbreiterung der Raman-Peaks und die globalen Rotverschiebungen ergänzten die Strukturmerkmale der defekten Phasen. Die defektreichen Strukturmotive werden durch Verfeinerungen der durch die Dichtefunktionaltheorie unterstützten Paarverteilungsfunktion (DFT-PDF) abgeleitet. DFT-PDF-Verfeinerungen zeigen, dass der nachbearbeitete Forsterit Mg-Frenkel-artige und Mg^{2+}-Zwischengitterdefekte mit Konzentrationen von 23(3) bzw. 10(3) Gew.-% enthält. DFT-Berechnungen bestätigten, dass die Strukturen der unterschiedlichen Defektmodelle energetisch stabil sind.

Eine Reihe von $(Ca_{1-x}Na_x)(Al_{2-x}Si_{2+x})O_8$-Plagioklas-Feldspäten wird unter Verwendung herkömmlicher Festkörpermethoden mit anschließenden Kalzinierungsschemata synthetisiert (**Kapitel 5**). Die durch Energiedispersive Röntgenspektroskopie erhaltenen chemischen Massenzusammensetzungen wurden für das Al/Si-Verhältnis in der Probe verwendet. Die synthetisierten Plagioklas-Feldspäte weisen einen DC von 73 Gew.-% – 84 Gew.-% auf, was auf einen moderaten Anteil amorpher Streuanteile schließen lässt. Ausgewählte Plagioklas-Feldspat-Zusammensetzungen (x = 0, 0,4 und 1) wurden mithilfe einer Kugelmühle mechanisch verwittert. Die Implementierung von PDF-Rietveld-Verfeinerungen basierend auf Röntgen-Mo-Daten deutet auf eine Unordnungsstruktur hin, insbesondere bei nachgemahlenen Albit-Endelementen. Die Verbreiterung der Raman-Moden und Frequenzverschiebungen ergänzten wiederum die Strukturmerkmale der defekten Phasen.

Chapter 1 – Introduction

For years, Mars has been an object of interest to a wide variety of researchers. Orbitals, landers, and rovers have been launched to obtain a large amount of valuable data and images, including the chemical [1-5] and mineralogical [6-10] composition of the Martian soils. These makes Mars arguably the second most understood planet by humans after the Earth. In the future, Mars exploration missions involving various countries worldwide will continue to lay the foundation for further realization of sending humans to Mars. Moreover, the recent increase in the number of privately funded space programs [11] has awakened the public's desire for space exploration to fulfill the vision of a multi-planetary future [12]. The ambitious plans to establish the first human settlement on Mars are often presented as the next great leap for humankind [13]. However, building up a habitat requires collective work from multiple disciplinary. It is important to note that eliminating entire supply from Earth is a long-term goal and will not be achievable in the early stages of a crewed mission [14]. By continually improving technology and adopting sustainable practices, Mars' self-sufficiency can be gradually increased and dependence on Earth can be minimized. For that reason, in-depth knowledge about available natural resources on Mars would be of uttermost importance within the frame of in-situ resource utilization (ISRU) process for oxygen and metal production [15, 16]. The local production of essential metals such as iron on Mars is emerging as a key factor for colonization and long-term sustainable habitation [17]. Under extraterrestrial conditions where the resources are limited, raw materials in the form of Martian regolith can be used [18].

Martian regolith is a collective term for materials that are naturally available on the surface of Mars. These can have a grain size of several meters for rocks, over several centimeters for boulders, several millimeters for sands down to micrometer-sized dusts. Martian regolith has been extensively investigated using X-ray diffraction data from the *Mars Science Laboratory* (MSL) [19] on the *Curiosity* rover [20, 21]. The analysis of this diffraction data estimated [7, 22-

24] approximately 28 wt.-% to 45 wt.-% amorphous fraction in the Martian regolith. Such defect-rich and highly concentrated amorphous phases in Martian regolith can be explained due to an extreme space weathering [24] largely by mechanical destruction in the course of impacts of meteorites and micrometeorites as well as the high-energy solar wind radiation. Within its crystalline phases, Ehlmann and Edwards [25] classified the mineral constituents into two categories: primary and secondary minerals. Framework silicates of $(Mg,Fe)_2SiO_4$ olivines, $(Ca,Na)(Al,Si)AlSi_2O_8$ plagioclase feldspars, $(K,Na)AlSi_3O_8$ alkali feldspars, $((Mg,Fe)_{0.95+x}Ca_{0.05-x})Si_2O_6$ orthopyroxenes, sulfides of $Fe_{1-x}S$ pyrrhotite and FeS_2 pyrite, as well as oxides of $(Fe_{1-x}Ti_x)_3O_4$ magnetite and $FeTiO_3$ ilmenite belong to the primary minerals. The secondary class includes phyllosilicates (clay minerals), carbonates, sulfates, chlorides, perchlorates, Fe_2O_3 hematite, FeOOH goethite, and akagaenite Fe(O,OH,Cl).

Based on this knowledge, several Martian regolith simulants have been produced on Earth for further specific testing and development. The simulants serve as an analogue to give a preview of the environment a space mission will encounter on Mars. On the one hand, the simulated regolith can be used to meet scientific research needs: such as astrobiology experiments, international space station experiments, wind tunnel experiments, infrastructure development, etc. Biologist conducted experiments to investigate whether the regolith have potential nutrients as resource for growing plants [26-28]. Another essential aspect reported by Wan et al. [29] is, that the Martian regolith constituents can be utilized for a multitude of building structures application [29]. On the other hand, the simulant can also be applied for the landing, moving and drilling test experiments of the probe on the surface of Mars. For instance, space engineers used it to test the traction of wheels on a rover in a specific terrain [30, 31].

Currently, there are more than 40 types of Martian regolith simulants covering different parts on the surface of Mars [32]. Karl et al. [33] categorized these simulants into three different generation. The so-called first-generation simulants are materials collected from a single location source [32, 33] (often further processed by grinding and sieving). The earliest simulant employing this concept was JSC Mars-1 based on a single source tephra from Hawaii [34].

Second-generation simulants use different minerals as the raw material according to material composition of the simulated soil [32, 33]. After drying, the raw materials are crushed and screened into semi-finished products of different sizes, followed by mixing to mimic mineralogical distribution and elemental abundances more closely [32, 33].

Third-generation simulants follow the second-generation mixing concept and further enhance physical- (texture and particle size distribution) and geo-mechanical properties using a binder to fuse single grains from different materials into large multi-mineral granules [33]. This approach was first introduced for asteroid simulants [35] and subsequently used for Mars global simulant (MGS-1) [23]. MGS-1 was developed in recent years as a high-fidelity mineralogical analogy to regolith in Mars [23].

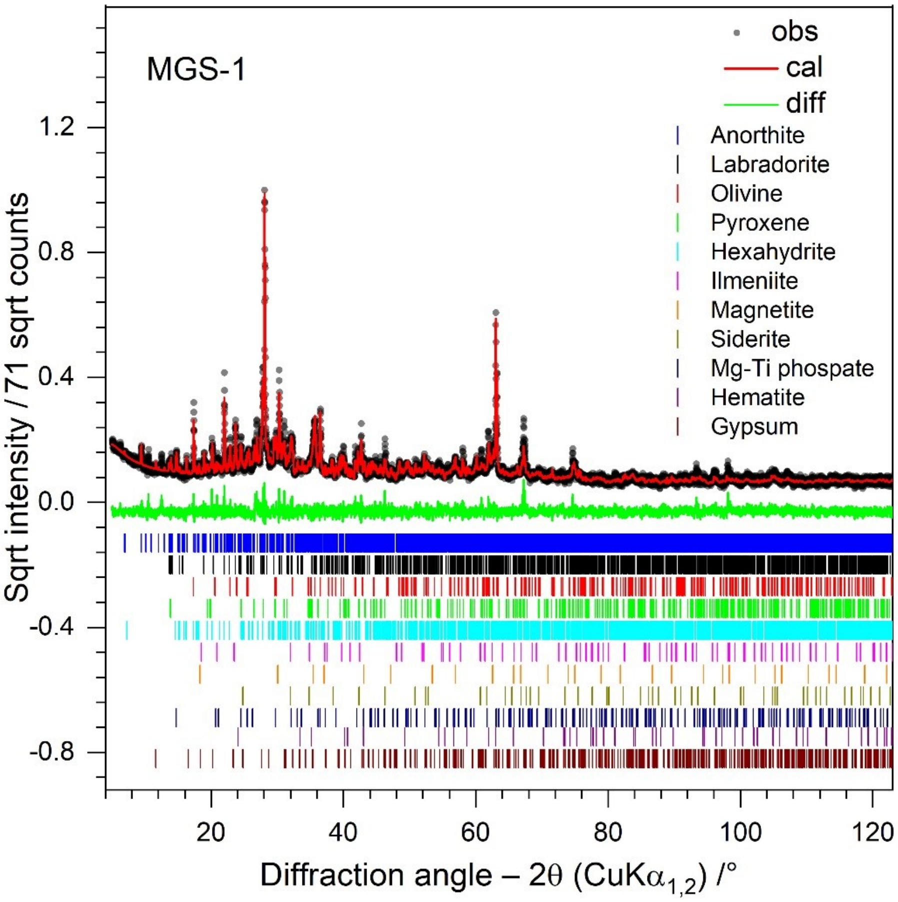

Figure 1. X-ray powder data Rietveld plot of MGS-1.

Table 1. Crystalline phase composition of MGS-1 obtained from X-ray powder diffraction Rietveld refinement.

Phase	Chemical formula	Fraction /wt.-%
Anorthite	$CaAl_2Si_2O_8$	52(1)
Labradorite	$(Ca_{0.63}Na_{0.37})(Al_{1.63}Si_{2.37})O_8$	17(1)
Olivine	$(Mg_{0.9}Fe_{0.1})_2SiO_4$	12(1)
Clinopyroxene	$(Fe_{1.6}Ca_{0.4})(SiO_3)_2$	9.1(8)
Hexahydrite	$MgSO_4.6H_2O$	4.4(1)
Ilmenite	$FeTiO_3$	1.4(3)
Magnetite	Fe_3O_4	1.4(3)
Siderite	$Fe(CO)_3$	0.8(2)
Mg-Ti Phosphate	$Mg_{0.5}Ti_2(PO_4)_3$	0.8(3)
Hematite	Fe_2O_3	0.6(4)
Gypsum	$CaSO_4.2H_2O$	0.5(2)

MGS-1 has been measured by in-house X-ray diffraction as preliminary characterization. The X-ray powder diffraction data Rietveld refinement plot of MGS-1 is shown in **Figure 1**. It provides MGS-1 to consist of 11 crystalline phases, which are dominated by $(Ca,Na)(Al,Si)AlSi_2O_8$ plagioclase feldspars and $(Mg,Fe)_2SiO_4$ olivine group minerals (**Table 1**). Due to their presence as major phase and vast chemical variety, olivine and plagioclase feldspars are chosen as representative phases in this thesis.

The main aim of this work is to synthesize highly-pure Martian regolith constituents, e.g. plagioclase feldspars and olivines. After successful synthesis, representative samples are post-processed using ball mill to mimic mechanical weathering occurred in Mars. Of particular notes, this study focuses on the difference between defect-poor and defect-rich phases. Successful syntheses are followed by the structural and spectroscopic analysis. Details of the post-weathered structural and spectroscopic characterizations offer great additional values to human's mission on Mars. Enabling an available (open source) data base, different Martian deposits can automatically be analyzed and validated.

1.1. Olivine

Olivine (M_2SiO_4) crystallizes in the orthorhombic space group *Pbnm* [36-38], as displayed in **Figure 2**. The *M*-cations mainly consist of Mg^{2+}, Fe^{2+} and trace amounts of Mn^{2+}, Ca^{2+}, Ni^{2+}, and Co^{2+} [39] located at the center of the edge-sharing MO_6 octahedra. The crystal structure is realized by one-dimensional octahedral chains running parallel to the crystallographic ***c***-axis, comparable to those found in the mullite-type phase [40-47]. A single $(SiO_4)^{4-}$ tetrahedra link the octahedral chains in the ***a***-direction, where the oxygen atoms are shared by three octahedral cations [48, 49]. The respective link in the ***b***-direction is realized by two non-equivalent octahedral sites: the first site (*M*1, chain octahedra) has inversion symmetry, while the other site (*M*2, linking octahedra) possesses mirror symmetry [50]. The coordinated octahedra around *M*1 and *M*2 are not identical, and the latter ones are slightly larger than the former ones [49]. Both sites can be occupied by various cations forming various endmembers such as forsterite (Mg_2SiO_4) [51-53], fayalite (Fe_2SiO_4) [54-56], tephroite (Mn_2SiO_4) [57-59], larnite (Ca_2SiO_4) [60-62], liebenbergite (Ni_2SiO_4) [63, 64], and cobalt olivine (Co_2SiO_4) [64, 65], or their solid solutions [66-69].

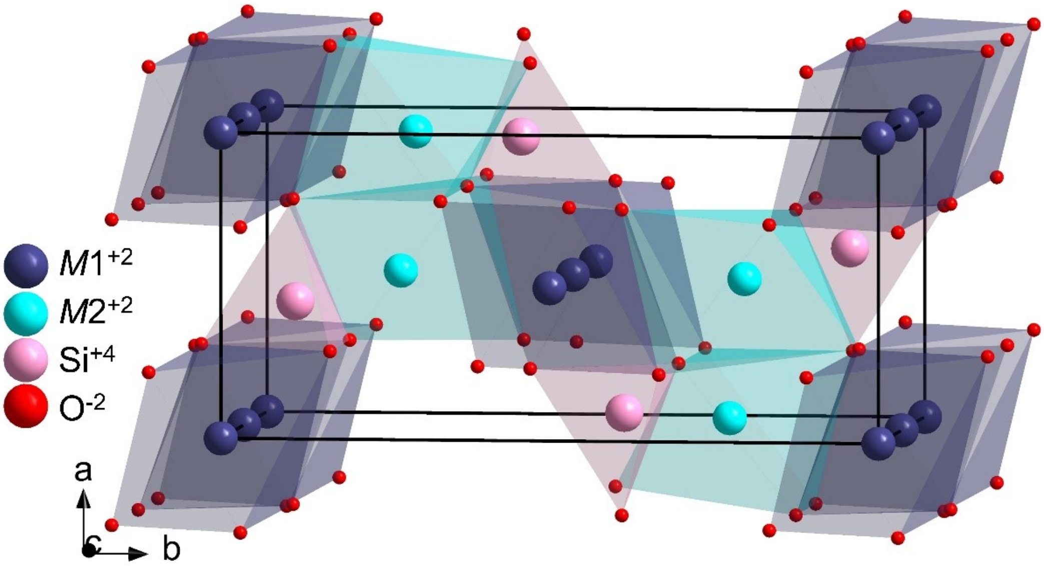

Figure 2. Crystal structure of M_2SiO_4 olivine.

Many studies have been carried out on available natural [70, 71] and synthetic olivine single crystals [72-75] with different compositions. In addition, attempts to synthesize powder samples using solution combustion technique [76-78], sol-gel method [79], mechanical activation followed by heat treatment [80-83], and reverse strike co-precipitation (RSC) [48] have been reported earlier. However, to the best of our knowledge, the full solid-solution powder data of olivine-type samples are still missing. Such polycrystalline olivine powders can better serve as representatives to characterize Martian olivine. Factors such as high-energy impact and mechanical stress from ball milling can simulate the mechanical weathering [84], inducing mechanically-induced defects [85, 86], amorphous contents and crystallite size distributions of the Martian materials.

Chapter 3 describes mechanochemical synthesis of the complete $(Mg_{1-x}Fe_x)_2SiO_4$ olivine solid solution to cover the wide range of olivine composition on Mars. The synthesis method, end products, as well as their structural- and spectroscopic characterizations are reported in a manuscript [87].

Moreover, forsterite endmember was post-processed using ball mill to mimic mechanical weathering process occurred in Mars. The structural differences between defect-rich and defect-poor forsterite as representative phase of Martian regolith is described in **Chapter 4**. The defect-rich structural motifs are deduced by density functional theory assisted pair distribution function (DFT-PDF) refinements.

1.2. Plagioclase feldspar

Plagioclase feldspars belong to MT_4O_8 aluminosilicates group, with a structure consisting of corner-sharing AlO_4 and SiO_4 tetrahedra (T) linked in an infinite three-dimensional array [88] as shown in **Figure 3**. The tetrahedra are arranged in four-membered rings which are stacked to form crankshafts parallel to the crystallographic **a**–axis. The crankshafts are connected together in an open structure with large cavities to accommodate alkali- or alkaline earth metals

(*M*). The structural complexity of plagioclase feldspar arises from the interplay between the Al/Si ordering among these tetrahedral and the displacive distortions of the entire framework [89]. Due to variation of the Al/Si molar ratio in the $(Ca_{1-x}Na_x)(Al_{2-x}Si_{2+x})O_8$ plagioclase feldspars, a different type of tetrahedra ordering occurs within the solid solution [90-92]. Of particular crystal-chemical aspects, the anorthite ($CaAl_2Si_2O_8$) endmember with Al:Si = 2:2 allows for a complete long range order with $I\bar{1}$ [93] symmetry, whereas the albite ($NaAlSi_3O_8$) endmember with Al:Si = 1:3 crystallizes in the space group $C\bar{1}$ [94] with short-range order. Kroll and Müller [95] suggested that the $I\bar{1} \leftrightarrow C\bar{1}$ transformation occurs between $x = 0.3$ and $x = 0.4$. Later, Carpenter and McConnell [96] determined this transformation as a steep line on the anorthite-albite binary phase diagram that passes through the points $\sim x = 0.41$ at 1273 K and $\sim x = 0.23$ at 1713 K.

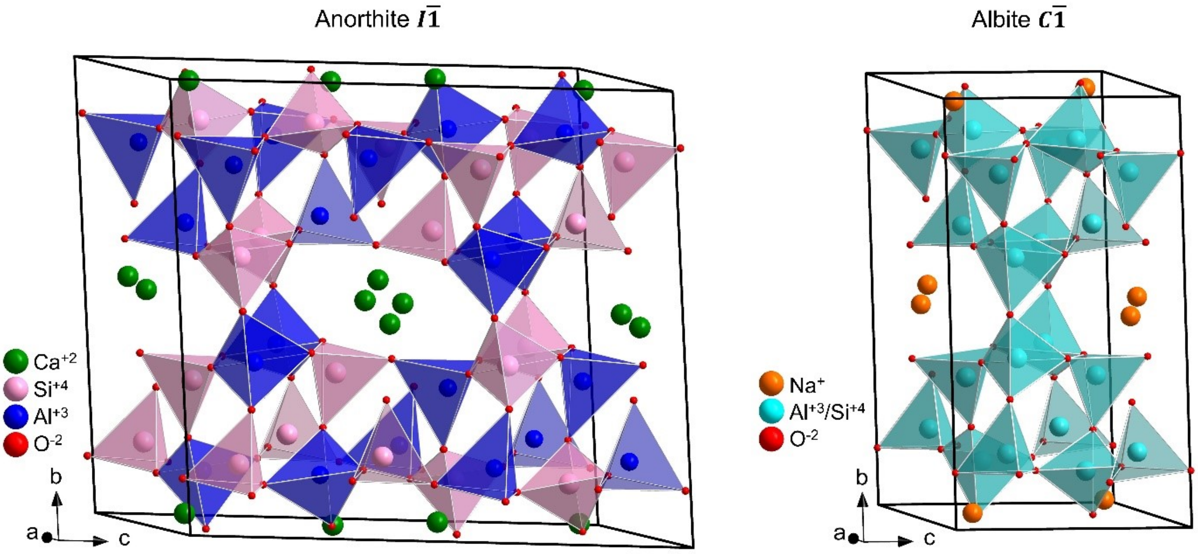
Anorthite $\boldsymbol{I\bar{1}}$

Albite $\boldsymbol{C\bar{1}}$

Figure 3. Crystal structures of anorthite (left) and albite (right).

Several studies have been conducted on naturally occurred plagioclase feldspars with particular interests on its bulk moduli [97], thermodynamic properties [98] and dissolution rate [99]. Synthesis of both single crystals [100, 101] and polycrystalline plagioclase feldspars ceramics [102-104] by various techniques have been reported earlier. Nonetheless, a systematic crystal-chemical study is still missing for a complete solid solution of plagioclase feldspars and their post-mechanical weathering effect relevant to Martian regolith. In **Chapter 5**, $(Ca_{1-x}Na_x)(Al_{2-x}Si_{2+x})O_8$ plagioclase feldspar solid solution and selective mechanically-weathered members are reviewed, in particular on their crystal structures and Raman spectroscopic features.

Reference

[1] I. Fleischer, J. Brueckner, C. Schröder, W. Farrand, E. Treguier, R.V. Morris, G. Klingelhoefer, K. Herkenhoff, D. Mittlefehldt, J. Ashley, Mineralogy and chemistry of cobbles at Meridiani Planum, Mars, investigated by the Mars Exploration Rover Opportunity, Journal of Geophysical Research: Planets 115(E7) (2010). Doi:10.1029/2010JE003621

[2] C. Fabre, S. Maurice, A. Cousin, R. Wiens, O. Forni, V. Sautter, D. Guillaume, Onboard calibration igneous targets for the Mars Science Laboratory Curiosity rover and the Chemistry Camera laser induced breakdown spectroscopy instrument, Spectrochimica Acta Part B: Atomic Spectroscopy 66(3-4) (2011) 280-289. Doi:10.1016/j.sab.2011.03.012

[3] R.B. Anderson, J.F. Bell III, Correlating multispectral imaging and compositional data from the Mars Exploration Rovers and implications for Mars Science Laboratory, Icarus 223(1) (2013) 157-180. Doi:10.1016/j.icarus.2012.11.029

[4] R. Gellert, B.C. Clark III, MSL, M.S. Teams, In situ compositional measurements of rocks and soils with the alpha particle X-ray spectrometer on NASA's Mars rovers, Elements 11(1) (2015) 39-44. Doi:10.2113/gselements.11.1.39

[5] M. Konstantinidis, E.A. Lalla, M.G. Daly, G. Lopez-Reyes, J. Stromberg, K. Cote, E. Cloutis, Elemental estimation of terrestrial analogues from the CanMars rover field campaign using LiRS: Implications for detecting silica-rich deposits on Mars, Icarus 358 (2021) 114113. Doi:10.1016/j.icarus.2020.114113

[6] D.L. Bish, D.F. Blake, D.T. Vaniman, S.J. Chipera, R.V. Morris, D.W. Ming, A.H. Treiman, P. Sarrazin, S.M. Morrison, R.T. Downs, C.N. Achilles, A.S. Yen, T.F. Bristow, J.A. Crisp, J.M. Morookian, J.D. Farmer, E.B. Rampe, E.M. Stolper, N. Spanovich, X-ray Diffraction Results from Mars Science Laboratory: Mineralogy of Rocknest at Gale Crater, Science 341(6153) (2013) 1238932. Doi:10.1126/science.1238932

[7] C.N. Achilles, R.T. Downs, D.W. Ming, E.B. Rampe, R.V. Morris, A.H. Treiman, S.M. Morrison, D.F. Blake, D.T. Vaniman, R.C. Ewing, S.J. Chipera, A.S. Yen, T.F. Bristow, B.L. Ehlmann, R. Gellert, R.M. Hazen, K.V. Fendrich, P.I. Craig, J.P. Grotzinger, D.J. Des Marais, J.D. Farmer, P.C. Sarrazin, J.M. Morookian, Mineralogy of an active eolian

sediment from the Namib dune, Gale crater, Mars, Journal of Geophysical Research: Planets 122(11) (2017) 2344-2361. Doi:10.1002/2017je005262

[8] M.C. De Sanctis, F. Altieri, E. Ammannito, D. Biondi, S. De Angelis, M. Meini, G. Mondello, S. Novi, R. Paolinetti, M. Soldani, Ma_MISS on ExoMars: mineralogical characterization of the martian subsurface, Astrobiology 17(6-7) (2017) 612-620. Doi:10.1089/ast.2016.1541

[9] E.B. Rampe, D.F. Blake, T. Bristow, D.W. Ming, D. Vaniman, R. Morris, C. Achilles, S. Chipera, S. Morrison, V. Tu, Mineralogy and geochemistry of sedimentary rocks and eolian sediments in Gale crater, Mars: A review after six Earth years of exploration with Curiosity, Geochemistry 80(2) (2020) 125605. Doi:10.1016/j.chemer.2020.125605

[10] S.M. Morrison, D.F. Blake, T.F. Bristow, N. Castle, S.J. Chipera, P.I. Craig, R.T. Downs, A. Eleish, R.M. Hazen, J.M. Meusburger, Expanded insights into Martian mineralogy: Updated analysis of Gale crater's mineral composition via CheMin crystal chemical investigations, Minerals 14(8) (2024) 773. Doi:10.3390/min14080773

[11] K. Olsson-Francis, P.T. Doran, V. Ilyin, F. Raulin, P. Rettberg, G. Kminek, M.-P.Z. Mier, A. Coustenis, N. Hedman, O. Al Shehhi, The COSPAR Planetary Protection Policy for robotic missions to Mars: A review of current scientific knowledge and future perspectives, Life Sciences in Space Research 36 (2023) 27-35. Doi:10.1016/j.lssr.2022.12.001

[12] E. Musk, Making humans a multi-planetary species, New Space 5(2) (2017) 46-61. Doi:10.1089/space.2017.29009.emu

[13] K. Szocik, K. Lysenko-Ryba, S. Banaś, S. Mazur, Political and legal challenges in a Mars colony, Space Policy 38 (2016) 27-29. Doi:10.1016/j.spacepol.2016.05.012

[14] C. Gross, M. Al-Samir, J.L. Bishop, F. Poulet, F. Postberg, D. Schubert, Prospecting in-situ resources for future crewed missions to Mars, Acta Astronautica (2024). Doi:10.1016/j.actaastro.2024.07.003

[15] P. Gayen, S. Sankarasubramanian, V.K. Ramani, Fuel and oxygen harvesting from Martian regolithic brine, Proceedings of the National Academy of Sciences 117(50) (2020) 31685-31689. Doi:10.1073/pnas.2008613117

[16] M. Hecht, J. Hoffman, D. Rapp, J. McClean, J. SooHoo, R. Schaefer, A. Aboobaker, J. Mellstrom, J. Hartvigsen, F. Meyen, Mars oxygen ISRU experiment (MOXIE), Space Science Reviews 217 (2021) 1-76. Doi:10.1007/s11214-020-00782-8

[17] E. Hinterman, J.A. Hoffman, Simulating oxygen production on Mars for the Mars oxygen in-situ resource utilization experiment, Acta Astronautica 170 (2020) 678-685. Doi:10.1016/j.actaastro.2020.02.043

[18] L. Schlüter, A. Cowley, Review of techniques for In-Situ oxygen extraction on the moon, Planetary and Space Science 181 (2020) 104753. Doi:10.1016/j.pss.2019.104753

[19] J.P. Grotzinger, J. Crisp, A.R. Vasavada, R.C. Anderson, C.J. Baker, R. Barry, D.F. Blake, P. Conrad, K.S. Edgett, B. Ferdowski, R. Gellert, J.B. Gilbert, M. Golombek, J. Gómez-Elvira, D.M. Hassler, L. Jandura, M. Litvak, P. Mahaffy, J. Maki, M. Meyer, M.C. Malin, I.

Mitrofanov, J.J. Simmonds, D. Vaniman, R.V. Welch, R.C. Wiens, Mars Science Laboratory Mission and Science Investigation, Space Science Reviews 170(1-4) (2012) 5-56. Doi:10.1007/s11214-012-9892-2

[20] R. Welch, D. Limonadi, R. Manning, Systems engineering the curiosity rover: A retrospective, 2013 8th international conference on system of systems engineering, IEEE, 2013, pp. 70-75. Doi:10.1109/SYSoSE.2013.6575245

[21] A.R. Vasavada, Mission overview and scientific contributions from the Mars Science Laboratory Curiosity rover after eight years of surface operations, Space Science Reviews 218(3) (2022) 14. Doi:10.1007/s11214-022-00882-7

[22] D.T. Vaniman, D.L. Bish, D.W. Ming, T.F. Bristow, R.V. Morris, D.F. Blake, S.J. Chipera, S.M. Morrison, A.H. Treiman, E.B. Rampe, M. Rice, C.N. Achilles, J.P. Grotzinger, S.M. McLennan, J. Williams, J.F.I. Bell, H.E. Newsom, R.T. Downs, S. Maurice, P. Sarrazin, A.S. Yen, J.M. Morookian, J.D. Farmer, K. Stack, R.E. Milliken, B.L. Ehlmann, D.Y. Sumner, G. Berger, J.A. Crisp, J.A. Hurowitz, R. Anderson, D.J. Des Marais, E.M. Stolper, K.S. Edgett, S. Gupta, N. Spanovich, M.S. Team, Mineralogy of a Mudstone at Yellowknife Bay, Gale Crater, Mars, Science 343 (2014). Doi:10.1126/science.1243480.

[23] K.M. Cannon, D.T. Britt, T.M. Smith, R.F. Fritsche, D. Batcheldor, Mars global simulant MGS-1: A Rocknest-based open standard for basaltic martian regolith simulants, Icarus 317 (2019) 470-478. Doi:10.1016/j.icarus.2018.08.019

[24] G. Certini, S. Karunatillake, Y.-Y.S. Zhao, P.-Y. Meslin, A. Cousin, D.R. Hood, R. Scalenghe, Disambiguating the soils of Mars, Planetary and Space Science 186 (2020). Doi:10.1016/j.pss.2020.104922

[25] B.L. Ehlmann, C.S. Edwards, Mineralogy of the Martian surface, Annual Review of Earth and Planetary Sciences 42 (2014) 291-315. Doi:10.1146/annurev-earth-060313-055024

[26] S. Silverstone, M. Nelson, A. Alling, J. Allen, Soil and crop management experiments in the Laboratory Biosphere: an analogue system for the Mars on Earth® facility, Advances in Space Research 35(9) (2005) 1544-1551. Doi:10.1016/j.asr.2005.06.008

[27] G.W. Wamelink, J.Y. Frissel, W.H. Krijnen, M.R. Verwoert, P.W. Goedhart, Can plants grow on Mars and the moon: a growth experiment on Mars and moon soil simulants, PLoS One 9(8) (2014) e103138. Doi:10.1371/journal.pone.0103138

[28] C. Verseux, M. Baqué, K. Lehto, J.-P.P. de Vera, L.J. Rothschild, D. Billi, Sustainable life support on Mars–the potential roles of cyanobacteria, International Journal of Astrobiology 15(1) (2016) 65-92. Doi:10.1017/S147355041500021X

[29] L. Wan, R. Wendner, G. Cusatis, A novel material for in situ construction on Mars: experiments and numerical simulations, Construction and Building Materials 120 (2016) 222-231. Doi:10.1016/j.conbuildmat.2016.05.046

[30] N. Cabrol, G. Chong-Diaz, C. Stoker, V. Gulick, R. Landheim, P. Lee, T. Roush, A. Zent, C.H. Lameli, A.J. Iglesia, Nomad rover field experiment, Atacama Desert, Chile: 1. Science

results overview, Journal of Geophysical Research: Planets 106(E4) (2001) 7785-7806. Doi:10.1029/1999JE001166

[31] T.P. Gouache, N. Patel, C. Brunskill, G.P. Scott, C.M. Saaj, M. Matthews, L. Cui, Soil simulant sourcing for the ExoMars rover testbed, Planetary and Space Science 59(8) (2011) 779-787. Doi:10.1016/j.pss.2011.03.006

[32] J. Liu, H. Li, L. Sun, Z. Guo, J. Harvey, Q. Tang, H. Lu, M. Jia, In-situ resources for infrastructure construction on Mars: A review, International journal of transportation science and technology 11(1) (2022) 1-16. Doi:10.1016/j.ijtst.2021.02.001

[33] D. Karl, K.M. Cannon, A. Gurlo, Review of space resources processing for Mars missions: Martian simulants, regolith bonding concepts and additive manufacturing, Open Ceramics 9 (2022) 100216. Doi:10.1016/j.oceram.2021.100216

[34] C.C. Allen, K.M. Jager, R.V. Morris, D.J. Lindstrom, M.M. Lindtsrom, J.P. Lockwood, Martian soil simulant available for scientific, educational study, Eos, Transactions American Geophysical Union 79(34) (1998) 405-409. Doi:10.1029/98EO00309

[35] D.T. Britt, K.M. Cannon, K. Donaldson Hanna, J. Hogancamp, O. Poch, P. Beck, D. Martin, J. Escrig, L. Bonal, P.T. Metzger, Simulated asteroid materials based on carbonaceous chondrite mineralogies, Meteoritics & Planetary Science 54(9) (2019) 2067-2082. Doi:10.1111/maps.13345

[36] K. Hanke, Beiträge zu Kristallstrukturen vom Olivin-typ, Beiträge zur Mineralogie und Petrographie 11(6) (1965) 535-558. Doi:10.1007/BF01110836

[37] M. Müller-Sommer, R. Hock, A. Kirfel, Rietveld refinement study of the cation distribution in (Co, Mg)-olivine solid solution, Physics and Chemistry of Minerals 24(1) (1997) 17-23. Doi:10.1007/s002690050013

[38] H.-R. Wenk, K. Raymond, Four new structure refinements of olivine, Zeitschrift für Kristallographie-Crystalline Materials 137(1-6) (1973) 86-105. Doi:10.1524/zkri.1973.137.1.86

[39] L. Zhang, J.R. Smyth, Crystal chemistry of metal element substitution in olivine and its high-pressure polymorphs: Implications for the upper-mantle and the mantle transition zone, Earth-Science Reviews 232 (2022) 104127. Doi:10.1016/j.earscirev.2022.104127

[40] R.J. Angel, C.T. Prewitt, Crystal structure of mullite: A re-examination of the average structure, American Mineralogist 71(11-12) (1986) 1476-1482.

[41] N. Bowen, J. Greig, E. Zies, Mullite, a silicate of alumina, Journal of the Washington Academy of Sciences 14(9) (1924) 183-191.

[42] R. Cong, T. Yang, K. Li, H. Li, L. You, F. Liao, Y. Wang, J. Lin, Mullite-type $Ga_4B_2O_9$: structure and order–disorder phenomenon, Acta Crystallographica Section B: Structural Science 66(2) (2010) 141-150. Doi:10.1107/S0108768110000650

[43] R.X. Fischer, H. Schneider, T.M. Gesing, Temperature-dependent X-ray Diffraction Studies of Mullite-type $(Bi_{1-x}Sr_x)_2M_4O_9$ Phases, Acta Crystallographica A-Foundation and Advances, 2009, pp. 232-233. Doi:10.1107/S010876730909521X

[44] M. Gogolin, M.M. Murshed, M. Ende, R. Miletich, T.M. Gesing, Uniaxial negative thermal expansion in the mullite-and borax-type $PbAlBO_4$ polymorphs, Journal of Materials Science 55(1) (2020) 177-190. Doi:10.1007/s10853-019-04013-6

[45] C.S. Reuter, M.M. Murshed, M. Fischer, T.M. Gesing, Synthesis, characterization and structure-property relations in mullite-type $Pb_2(Pb_{1-x}Sn_x)O_4$ solid solution, Zeitschrift für Kristallographie - Crystalline Materials (2024). Doi:10.1515/zkri-2024-0088

[46] S. Wittmann, M.M. Murshed, L. Schumacher, A. Koldemir, R. Pöttgen, T.M. Gesing, Synthesis and characterization of mullite-type Sn $(Cr_{1-x}V_x)BO_4$: Structural, vibrational, magnetic, and thermal properties, Journal of the American Ceramic Society (2024). Doi:10.1111/jace.19928

[47] K. Ghosh, M.M. Murshed, M. Fischer, T.M. Gesing, Aluminum to germanium inversion in mullite-type RAlGeO$_5$: Characterization of a rare phenomenon for R= Y, Sm–Lu, Journal of the American Ceramic Society 105(1) (2022) 728-741. Doi:10.1111/jace.18085

[48] R.Y.S. Zampiva, L.H. Acauan, L.M. dos Santos, R.H.R. de Castro, A.K. Alves, C.P. Bergmann, Nanoscale synthesis of single-phase forsterite by reverse strike co-precipitation and its high optical and mechanical properties, Ceramics International 43(18) (2017) 16225-16231. Doi:10.1016/j.ceramint.2017.08.201

[49] S. Demouchy, Defects in olivine, Eur. J. Mineral. 33(3) (2021) 249-282. Doi:10.5194/ejm-33-249-2021

[50] H. Yang, J. Shi, M. Gong, K.W. Cheah, Synthesis and photoluminescence of Eu^{3+}- or Tb^{3+}-doped Mg_2SiO_4 nanoparticles prepared by a combined novel approach, Journal of Luminescence 118(2) (2006) 257-264. Doi:10.1016/j.jlumin.2005.09.005

[51] N.L. Bowen, The ternary system; diopside-forsterite-silica, American Journal of Science 4(225) (1914) 207-264.

[52] G.A. Lager, F.K. Ross, F. Rotella, J. Jorgensen, Neutron powder diffraction of forsterite, Mg_2SiO_4: a comparison with single-crystal investigations, Journal of Applied Crystallography 14(2) (1981) 137-139. Doi:10.1107/S0021889881008935

[53] R. Van der Wal, A. Vos, A. Kirfel, Conflicting results for the deformation properties of Forsterite, Mg_2SiO_4, Acta Crystallographica Section B: Structural Science 43(2) (1987) 132-143. Doi:10.1107/S0108768187098161

[54] A. Lacroix, A fayalite rock, Comptes Rendus Hebdomadaires Des Seances De L Academie Des Sciences 130 (1900) 1778-1780.

[55] R.M. Hazen, Effects of temperature and pressure on the crystal structure of ferromagnesian olivine, American Mineralogist 62(3-4) (1977) 286-295.

[56] Y. Kudoh, H. Takeda, Single crystal X-ray diffraction study on the bond compressibility of fayalite, Fe_2SiO_4 and rutile, TiO_2 under high pressure, Physica B+C 139-140 (1986) 333-336. Doi:10.1016/0378-4363(86)90591-7

[57] K. Fujino, S. Sasaki, Y. Takeuchi, R. Sadanaga, X-ray determination of electron distributions in forsterite, fayalite and tephroite, Acta Crystallographica Section B: Structural Crystallography and Crystal Chemistry 37(3) (1981) 513-518. Doi:10.1107/S0567740881003506

[58] S. Parker, C. Catlow, A. Cormack, Structure prediction of silicate minerals using energy-minimization techniques, Acta Crystallographica Section B: Structural Science 40(3) (1984) 200-208. Doi:10.1107/S0108768184001981

[59] Z. Ye, J. Xu, D. Fan, D. Zhang, W. Zhou, H. Xie, Amorphous Mn_2SiO_4: A potential manganese phase in the stagnant slab, American Mineralogist 108(11) (2023) 2121-2130. Doi:10.2138/am-2022-8606

[60] D.K. Smith, A. Majumdar, F. Ordway, The crystal structure of γ-dicalcium silicate, Acta Crystallographica 18(4) (1965) 787-795. Doi:10.1107/S0365110X65001780

[61] R. Czaya, Refinement of the structure of γ-Ca_2SiO_4, Acta Crystallographica Section B 27(4) (1971) 848-849. Doi:10.1107/S0567740871003030

[62] A.E. Zadov, V.M. Gazeev, N.N. Pertsev, A.G. Gurbanov, N.A. Yamnova, E.R. Gobechiya, N.V. Chukanov, Discovery and investigation of a natural analog of calcio-olivine (γ-Ca_2SiO_4), Doklady Earth Sciences 423(2) (2008) 1431-1434. Doi:10.1134/s1028334x08090237

[63] D. Zhang, Y. Hu, J. Xu, R.T. Downs, J.E. Hammer, P.K. Dera, High-pressure behavior of liebenbergite: The most incompressible olivine-structured silicate, American Mineralogist 104(4) (2019) 580-587. Doi:10.2138/am-2019-6680

[64] O. Tamada, K. Fujino, S. Sasaki, Structures and electron distributions of α-Co_2SiO_4 and α-Ni_2SiO_4 (olivine structure), Acta Crystallographica Section B: Structural Science 39(6) (1983) 692-697. Doi:10.1107/S0108768183003250

[65] N. Morimoto, M. Tokonami, M. Watanabe, K. Koto, Crystal Structures of Three Polymorphs of Co_2SiO_4, American Mineralogist 59(5-6) (1974) 475-485.

[66] M. Miyake, H. Nakamura, H. Kojima, F. Marumo, Cation ordering in Co-Mg olivine solid-solution series, American Mineralogist 72(5-6) (1987) 594-598.

[67] D. Boström, Single crystal x-ray diffraction studies of synthetic (Co, Mg)-olivine solid solutions, Acta Chem Scand 43 (1989) 121-127. Doi:10.3891/acta.chem.scand.43-0121

[68] H.J. Rösler, Lehrbuch der Mineralogie, Dt. Verlag für Grundstoffindustrie1991.

[69] O. Qafoku, E.S. Ilton, M.E. Bowden, L. Kovarik, X. Zhang, R.K. Kukkadapu, M.H. Engelhard, C.J. Thompson, H.T. Schaef, B.P. McGrail, Synthesis of nanometer-sized

fayalite and magnesium-iron (II) mixture olivines, Journal of colloid and interface science 515 (2018) 129-138. Doi:10.1016/j.jcis.2018.01.036

[70] T. Mouri, M. Enami, Raman spectroscopic study of olivine-group minerals, Journal of Mineralogical and Petrological Sciences 103(2) (2008) 100-104. Doi:10.2465/jmps.071015

[71] B. Kolesov, C. Geiger, A Raman spectroscopic study of Fe–Mg olivines, Physics and Chemistry of Minerals 31(3) (2004) 142-154. Doi:10.1007/s00269-003-0370-y

[72] Y. Sumino, O. Nishizawa, T. Goto, I. Ohno, M. Ozima, Temperature variation of elastic constants of single-crystal forsterite between -190° and 400°C, Journal of Physics of the Earth 25(4) (1977) 377-392. Doi:10.4294/jpe1952.25.377

[73] Y. Sumino, The elastic constants of Mn_2SiO_4, Fe_2SiO_4 and Co_2SiO_4, and the elastic properties of olivine group minerals at high temperature, Journal of Physics of the Earth 27(3) (1979) 209-238. Doi:10.4294/jpe1952.27.209

[74] Z. Mao, D. Fan, J.-F. Lin, J. Yang, S.N. Tkachev, K. Zhuravlev, V.B. Prakapenka, Elasticity of single-crystal olivine at high pressures and temperatures, Earth and Planetary Science Letters 426 (2015) 204-215. Doi:10.1016/j.epsl.2015.06.045

[75] P. Raterron, E. Amiguet, J. Chen, L. Li, P. Cordier, Experimental deformation of olivine single crystals at mantle pressures and temperatures, Physics of the Earth and Planetary Interiors 172(1-2) (2009) 74-83. Doi:10.1016/j.pepi.2008.07.026

[76] R. Naik, S.C. Prashantha, H. Nagabhushana, S.C. Sharma, H.P. Nagaswarupa, K.S. Anantharaju, B.M. Nagabhushana, H.B. Premkumar, K.M. Girish, A single phase, red emissive Mg_2SiO_4:Sm^{3+} nanophosphor prepared via rapid propellant combustion route, Spectrochim Acta A Mol Biomol Spectrosc 140 (2015) 516-23. Doi:10.1016/j.saa.2015.01.011

[77] K. Mondal, P. Kumari, J. Manam, Influence of doping and annealing temperature on the structural and optical properties of Mg_2SiO_4:Eu^{3+} synthesized by combustion method, Current Applied Physics 16(7) (2016) 707-719. Doi:10.1016/j.cap.2016.04.001

[78] S.C. Prashantha, B.N. Lakshminarasappa, B.M. Nagabhushana, Photoluminescence and thermoluminescence studies of Mg_2SiO_4:Eu^{3+} nano phosphor, Journal of Alloys and Compounds 509(42) (2011) 10185-10189. Doi:10.1016/j.jallcom.2011.03.148

[79] S. Ni, L. Chou, J. Chang, Preparation and characterization of forsterite (Mg_2SiO_4) bioceramics, Ceramics International 33(1) (2007) 83-88. Doi:10.1016/j.ceramint.2005.07.021

[80] M.H. Fathi, M. Kharaziha, Mechanically activated crystallization of phase pure nanocrystalline forsterite powders, Materials Letters 62(27) (2008) 4306-4309. Doi:10.1016/j.matlet.2008.07.015

[81] F. Tavangarian, R. Emadi, Synthesis of nanocrystalline forsterite (Mg_2SiO_4) powder by combined mechanical activation and thermal treatment, Materials Research Bulletin 45(4) (2010) 388-391. Doi:10.1016/j.materresbull.2009.12.032

[82] M.H. Fathi, M. Kharaziha, The effect of fluorine ion on fabrication of nanostructure forsterite during mechanochemical synthesis, Journal of Alloys and Compounds 472(1-2) (2009) 540-545. Doi:10.1016/j.jallcom.2008.05.032

[83] V. Sepelak, M. Myndyk, M. Fabian, K.L. Da Silva, A. Feldhoff, D. Menzel, M. Ghafari, H. Hahn, P. Heitjans, K.D. Becker, Mechanosynthesis of nanocrystalline fayalite, Fe_2SiO_4, Chem Commun (Camb) 48(90) (2012) 11121-3. Doi:10.1039/c2cc36370d

[84] M.-C.M. Eppes, Mechanical Weathering: A Conceptual Overview, Treatise on Geomorphology 3 (2022) 30-45. Doi:10.1016/B978-0-12-818234- 5.00200-5

[85] J. López-García, V. Sánchez-Alarcos, V. Recarte, J.A. Rodríguez-Velamazán, I. Unzueta, J. García, F. Plazaola, P. La Roca, J. Pérez-Landazábal, Effect of high-energy ball-milling on the magnetostructural properties of a Ni45Co5Mn35Sn15 alloy, Journal of Alloys and Compounds 858 (2021) 158350. Doi:10.1016/j.jallcom.2020.158350

[86] W. Ashraf, A. Khan, S. Bansal, M. Khanuja, Mechanical ball milling: A sustainable route to induce structural transformations in tungsten disulfide for its photocatalytic applications, Physica E: Low-dimensional Systems and Nanostructures 140 (2022) 115152. Doi:10.1016/j.physe.2022.115152

[87] M.I. Jundullah Hanafi, M.M. Murshed, L. Robben, T.M. Gesing, Mechanochemical synthesis of $(Mg_{1-x}Fe_x)_2SiO_4$ olivine phases relevant to Martian regolith: structural and spectroscopic characterizations, Zeitschrift für Kristallographie - Crystalline Materials 239 (2024) 1-11. Doi:10.1515/zkri-2024-0078

[88] P.H. Ribbe, The Crystal Structures of the Aluminum-Silicate Feldspars, in: I. Parsons (Ed.), Feldspars and their Reactions, Springer Netherlands, Dordrecht, 1994, pp. 1-49. Doi:10.1007/978-94-011-1106-5_1

[89] R. Angel, High-pressure structure of anorthite, American Mineralogist 73(9-10) (1988) 1114-1119.

[90] E.R. Myers, V. Heine, M.T. Dove, Thermodynamics of Al/Al avoidance in the ordering of Al/Si tetrahedral framework structures, Physics and Chemistry of Minerals 25 (1998) 457-464. Doi:10.1007/s002690050136

[91] V.L. Vinograd, The description of Al, Si ordering in aluminosilicates using the cluster variation method, American Mineralogist 84(3) (1999) 311-324. Doi:10.2138/am-1999-0314

[92] V.L. Vinograd, A. Putnis, A two-dimensional spin model of Al/Si order in feldspars: visualization of short-range and long-range order, European Journal of Mineralogy 13(2) (2001) 273-288. Doi:10.1127/0935-1221/01/0013-0273

[93] R.J. Angel, M. Carpenter, L. Finger, Structural variation associated with compositional variation and order-disorder behavior in anorthite-rich feldspars, American Mineralogist 75(1-2) (1990) 150-162.

[94] N. Organova, I. Marsii, N. Zakharov, V. Nasedkin, S. Borisovskii, I. Rozhdestvenskaya, T. Ivanova, Structures of the K-and Na-components of two-phase feldspar from Primorskii Krai, Crystallography Reports 44 (1999). Doi:10.1134/1.171098

[95] H. Kroll, W.F. Müller, X-ray and electron-optical investigation of synthetic high-temperature plagioclases, Physics and Chemistry of Minerals 5 (1980) 255-277. Doi:10.1007/BF00348574

[96] M.A. Carpenter, J.D.C. McConnell, Experimental delineation of the C 1⇋ I 1 transformation in intermediate plagioclase feldspars, American Mineralogist 69(1-2) (1984) 112-121.

[97] R.J. Angel, Equations of state of Plagioclase Feldspars, Contributions to Mineralogy and Petrology 146(4) (2004) 506-512. Doi:10.1007/s00410-003-0515-5

[98] M.A. Carpenter, J.D.C. McConnell, A. Navrotsky, Enthalpies of ordering in the plagioclase feldspar solid solution, Geochimica et Cosmochimica Acta 49(4) (1985) 947-966. Doi:10.1016/0016-7037(85)90310-2

[99] A. Perez, D. Daval, M. Fournier, M. Vital, J.-M. Delaye, S. Gin, Comparing the reactivity of glasses with their crystalline equivalents: The case study of plagioclase feldspar, Geochimica et Cosmochimica Acta 254 (2019) 122-141. Doi:10.1016/j.gca.2019.03.030

[100] W. Flehmig, The synthesis of feldspars at temperatures between 0–80 C, their ordering behaviour and twinning, Contributions to Mineralogy and Petrology 65(1) (1977) 1-9. Doi:10.1007/BF00373564

[101] G. Lofgren, An experimental study of plagioclase crystal morphology; isothermal crystallization, American journal of Science 274(3) (1974) 243-273.

[102] M.M. Krzmanc, M. Valant, D. Suvorov, A structural and dielectric characterization of $Na_xCa_{1-x}Al_{2-x}Si_{2+x}O_8$ (x=0 and 1) ceramics, Journal of the European Ceramic Society 25(12) (2005) 2835-2838. Doi:10.1016/j.jeurceramsoc.2005.03.151

[103] W. Li, Z.X. Yue, F. Zhao, J. Pei, L.T. Li, Structure and Microwave Properties of $Na_xCa_{1-x}Al_{2-x}Si_{2+x}O_8$ (0< x< 0.67) Plagioclase Feldspar, Key Engineering Materials 368 (2008) 185-187. Doi:10.4028/scientific.net/KEM.368-372.185

[104] M.M. Krzmanc, M. Valant, B. Jancar, D. Suvorov, Sub-Solidus Synthesis and Microwave Dielectric Characterization of Plagioclase Feldspars, Journal of the American Ceramic Society 88(9) (2005) 2472-2479. Doi:10.1111/j.1551-2916.2005.00461.x

Chapter 2 – Experimental methods

2.1. Synthesis

2.1.1. Olivine solid solution

The olivine $(Mg_{1-x}Fe_x)_2SiO_4$ solid solution with $\Delta x = 0.1$ was synthesized via ball milling with subsequent calcination at high temperature. MgO (Merck > 97 %), Fe (Merck >97 %), Fe_2O_3 (Riedel-de Haën >99 %) and amorphous SiO_2 obtained from TEOS hydrolysis [1] were used as starting materials. A stoichiometric powder mixture with 10 wt-% of extra SiO_2 were mixed and ground together in an agate mortar. The extra amount of SiO_2 was necessary to overcome the gained mass from water absorption. The mixture was then placed in the grinding jar together with 10 g tungsten carbide (WC) balls. The powder was milled for 3 h with a rotational frequency of 15 Hz. Finally, the milled powder was collected from the grinding jar and heated in a corundum boat at 1373 K under forming gas (5 % H_2 / 95 % N_2) atmosphere for 6 h. The heating and cooling rate was set to 10 K/min and 5 K/min, respectively. Each obtained powder sample was hand ground in an agate mortar for further characterization.

2.1.2. Forsterite

In addition to mechanochemical method, forsterite endmember was also synthesized with reverse strike co-precipitation (RSC) method [2]. Magnesium nitrate hexahydrate ($Mg(NO_3)_2 \cdot 6H_2O$) 99.9 % and tetraethyl orthosilicate (TEOS) 98 % were purchased from VWR Chemicals and used as received. Stoichiometric amounts of $Mg(NO_3)_2 \cdot 6H_2O$ and TEOS were dissolved in a solution of 40 ml of ethanol and 3 ml of HNO_3 (≥ 65 %) under magnetic stirring for 1 h. The precursor solution was slowly dripped into 50 ml of 25 % NH_4OH under continuous stirring. The base solution formed a colloid while the precursor solution was being dripped, until the last drop forming a white precipitate. Simultaneously, several drops of concentrated NH_4OH were added to keep the pH > 8. Thereafter, the precipitate was centrifuged at 60 Hz for 5 min. The supernatant was removed, and ethanol was used to wash the precipitated powder. The centrifugation was repeated three times. Finally, the precipitated solid was placed in a furnace at 473 K for 16 h. The resulting solid was ground in a mortar and calcined at 1373 K for 1 h after reaching the temperature with a heating and cooling rate of 15 K/min and 5 K/min, respectively.

Defect-rich forsterite was prepared by crushing a pure as-synthesized forsterite by ball milling. The pure forsterite (1 g) was placed into the grinding jar with 20 g WC balls. The powder was milled at 15 Hz for 1 h. Thereafter, one half of the milled powder was kept separately and labeled as crushed forsterite. The other half was calcined at 1373 K for 1 h under air to heal the introduced defects, hence labeled as healed forsterite.

2.1.3. Plagioclase feldspar solid solution

The plagioclase feldspar $(Ca_{1-x}Na_x)(Al_{2-x}Si_{2+x})O_8$ solid solution with $\Delta x = 0.1$ was synthesized via conventional solid-state method with subsequent calcination schemes. Calcium carbonate ($CaCO_3$, ChemPUR 99 %), sodium carbonate ($NaCO_3$, ORG Laborchemie 99.5 %) Kaolin ($Al_2Si_2O_5(OH)_4$, Sigma-Aldrich) and amorphous SiO_2 (Thermo scientific 99.9 %) were used as starting materials. Stoichiometric amount of aforementioned starting materials was ground in an agate mortar. The mixed powder was transferred to a porcelain crucible and calcined in a muffle furnace at 1173 K for 12 h. The obtained solid was ground and pressed into a pellet using uniaxial force of 10 kN in a 20 mm diameter cylinder mold for 5 minutes. The pellets were placed on a platinum sheet and calcined in air for 5 days at various final firing temperature, ranging from 1273 - 1673 K. The solid was then hammered into coarse pieces and finely ground for further characterization. Selective members (x = 0, 0.4 and 1) were mechanically weathered using high energy ball mill. Each powder was milled with tungsten carbide (WC) jar and balls. The ball to powder ratio was set to 5:1, while milling frequency and time were set for 15 Hz and 1 h, respectively.

2.2. X-ray powder diffraction

X-ray powder diffraction (XRPD) data collections were carried out on a Bruker D8 Discover diffractometer using Cu$K_{\alpha 1,2}$ radiation ($\lambda_{K\alpha 1}$ = 154.05929(5) pm, $\lambda_{K\alpha 2}$ = 154.4414(2) pm) in Bragg–Brentano geometry. Data were collected at ambient condition from 5° to 85° 2θ with a step width of 0.0149° 2θ and a measurement time of 1.2 s per step. XRPD data Rietveld refinements were carried out using TOPAS V6.0 (Bruker AXS, Germany). During the Rietveld refinements, the background, sample displacement, metric, atomic positional and profile parameters were optimized. The amorphous fraction of the samples was quantified from the degree of crystallinity (DC) as implemented in the TOPAS software. For these calculations it was assumed that the average scattering power of the crystalline fraction of the sample was identical to that of the amorphous fraction. The latter one could consist of either glassy or quantum-crystalline (a few nanometric coherence length) contributions [3]. Using the fundamental parameter approach [4] with a used maximum observable average crystallite size (MOACS) of 290 nm for copper radiation, the apparent average crystallite size (ACS) was calculated from all the observed X-ray reflections, which is described as $L_{Vol}(IB)$ by the TOPAS suite. $L_{Vol}(IB)$ refers to the volume-weighted mean of the coherently diffracting domain size using the integral breadth for the description of the reflection profile. The respective pseudo-Voigt profile function was deconvoluted into Gaussian and Lorentzian components, describing the ACS and the micro-strain (ε_0), respectively. The information deduced during these (classical) Rietveld refinements are, except the DC, based on the appearance of the Bragg reflections and an ideal arrangement of atoms in a unit-cell only [5].

To confirm the average crystallite size without any restrictions of the Scherrer equation and to get further information of the crystallite size distribution, the obtained diffraction data are reduced on their $\lambda_{K\alpha 2}$ contribution and analyzed using the EnvACS approach [6]. As such, the X-ray diffraction data are converted to pair distribution function data using pdfgetx3 [7] followed by applying the Envelope model which combines the broadest and the narrowest possible distributions of the crystallites using the equation of Howel et al. [8] for spherical crystallites.

2.3. X-ray total scattering

Total scattering data were collected in order to calculate the respective atomic pair distribution functions (PDF). X-ray total scattering experiments were carried out using two instruments:

1) P02.1@PETRA-III beamline, DESY, Hamburg [9] with a fixed energy of 60 keV (λ = 20.734(2) pm). The beamline was equipped with a Varex XRD 4343CT detector (pixel size 150 µm x 150 µm, 2880 x 2880 pixels). Each sample was measured in 1 mm Kapton capillaries and exposed to the radiation for 300 s within a set-up particularly optimized for rapid in-situ measurement.
2) Stoe STADI MP diffractometer (Stoe & Cie. GmbH, Darmstadt, Germany) in Debye–Scherrer geometry. Powder samples were placed in a borosilicate glass capillary of 0.5 mm outer diameter and 0.01 mm wall thickness. Thereafter, they were mounted on the diffractometer. Homogeneous irradiation of the powders was achieved with a sample spinner. Ge(111) monochromatized MoK$_{\alpha1}$ radiation was used for the measurement with a MYTHEN 4K (Dectris) detector from 3° to 105° 2θ and a step width of 0.015° 2θ. The measurement time per data point were in the range of 33,390 - 57,240 s (total measurement time of 70 - 120 h).

Each measured dataset was background corrected with an empty capillary. The pair distribution function *G(r)* was calculated using the program PDFgetX3 [10]. Structure model fitting against PDF data was performed using PDFgui [11].

2.4. UV/Vis spectroscopy

The UV/Vis diffuse reflectance spectra were carried out using a UV-2600 spectrophotometer (Shimadzu, Japan) equipped with an ISR-2600 plus two-detector integrating sphere (Pike Technologies, USA). Barium sulphate ($BaSO_4$) powder was used as reference for the baseline correction. The data were collected from 190 nm to 850 nm with a step of 1 nm. Each spectral dataset is the mean-averaged of ten repetitions for a better signal/noise ratio. The change of the light source occurred at 323 nm. The Kubelka−Munk function [12] was implemented to approximate the optical absorption from the reflectance data. Direct and indirect band-gap energies were calculated using the Tauc method [13, 14] and compared with the value obtained from the "derivation of absorption spectrum fitting" (DASF) [15] method, which enable to determine the type of optical transition without presuming the nature of transition. The full analysis of band-gap transition type and band-gap energy is combined in the RATD (reflectance–absorbance–Tauc–DASF) analysis [6].

2.5. Raman spectroscopy

Raman spectra were recorded on a LabRam ARAMIS (Horiba Jobin – Yvon) micro-Raman spectrometer equipped with a green laser (λ_{ex} = 532 nm and < 20 mW). A 100x objective (Olympus) with a numerical aperture of 0.9 provides a focus spot of 721 nm diameter when closing the confocal hole to 200 µm. Each spectrum ranged between 100 cm^{-1} and 1000 cm^{-1} with a spectral resolution of approximately 1.2 cm^{-1} using a grating of 1800 grooves/mm and a thermoelectrically cooled CCD detector (Synapse, 1024 x 256 pixels).

2.6. Scanning electron microscope (SEM) and energy dispersive X-ray (EDX) spectroscopy

Elemental analysis was employed on the synthesized plagioclase feldspars by scanning electron microscopy/energy dispersive X-ray (SEM/EDX) spectroscopy. SEM was carried out using a JMS-6510 (JEOL GmbH, Munich, Germany) equipped with an X-Flash 410-M detector (Bruker) for EDX spectroscopy. A small amount of powder sample was taken on conducting carbon tabs and sputtered with gold for 20 s with a JFC-1200 coater (JEOL) followed by inserting it into the SEM chamber. EDX spectra were collected using an excitation voltage of 20 kV.

Reference

[1] D. Qi, C. Lin, H. Zhao, H. Liu, T. Lü, Size regulation and prediction of the SiO_2 nanoparticles prepared via Stöber process, Journal of Dispersion Science and Technology 38(1) (2017) 70-74. Doi:10.1080/01932691.2016.1143373

[2] R.Y.S. Zampiva, L.H. Acauan, L.M. dos Santos, R.H.R. de Castro, A.K. Alves, C.P. Bergmann, Nanoscale synthesis of single-phase forsterite by reverse strike co-precipitation and its high optical and mechanical properties, Ceramics International 43(18) (2017) 16225-16231. Doi:10.1016/j.ceramint.2017.08.201

[3] T.M. Gesing, M.M. Murshed, S. Schuh, O. Thüringer, K. Krämer, T. Neudecker, C.B. Mendive, L. Robben, Nano-crystalline precursor formation, stability, and transformation to mullite-type visible-light photocatalysts, Journal of Materials Science 57 (2022) 1-20. Doi:10.1007/s10853-022-07854-w

[4] J.P. Cline, D.R. Black, D. Gil, A. Henins, D. Windover, The application of the fundamental parameters approach as implemented in TOPAS to divergent beam powder diffraction data, Materials Science Forum 651 (2010) 201-219. Doi:10.4028/www.scientific.net/MSF.651.201

[5] H.M. Rietveld, A profile refinement method for nuclear and magnetic structures, Journal of applied Crystallography 2(2) (1969) 65-71. Doi:10.1107/S0021889869006558

[6] T.M. Gesing, L. Robben, Determination of the average crystallite size and the crystallite size distribution: The envelope function approach EnvACS, Journal of Applied Crystallography (2024). Doi:10.1107/S1600576724007362

[7] P. Juhás, T. Davis, C.L. Farrow, S.J. Billinge, PDFgetX3: a rapid and highly automatable program for processing powder diffraction data into total scattering pair distribution functions, Journal of Applied Crystallography 46(2) (2013) 560-566. Doi:10.1107/S0021889813005190

[8] R.C. Howell, T. Proffen, S.D. Conradson, Pair distribution function and structure factor of spherical particles, Physical Review B 73(9) (2006) 094107. Doi:10.1103/PhysRevB.73.094107

[9] A.-C. Dippel, H.-P. Liermann, J.T. Delitz, P. Walter, H. Schulte-Schrepping, O.H. Seeck, H. Franz, Beamline P02.1 at PETRA III for high-resolution and high-energy powder diffraction, Journal of Synchrotron Radiation 22(3) (2015) 675-687. Doi:10.1107/S1600577515002222

[10] P. Juhás, T. Davis, C.L. Farrow, S.J. Billinge, PDFgetX3: a rapid and highly automatable program for processing powder diffraction data into total scattering pair distribution functions, Journal of Applied Crystallography 46(2) (2013) 560-566. Doi:10.1107/S0021889813005190

[11] C. Farrow, P. Juhas, J. Liu, D. Bryndin, E. Božin, J. Bloch, T. Proffen, S. Billinge, PDFfit2 and PDFgui: computer programs for studying nanostructure in crystals, Journal of Physics: Condensed Matter 19(33) (2007) 335219. Doi:10.1088/0953-8984/19/33/335219

[12] P. Kubelka, Ein beitrag zur optik der farbanstriche, Z. tech. Phys 12 (1931) 593-601.

[13] J. Tauc, R. Grigorovici, A. Vancu, Optical Properties and Electronic Structure of Amorphous Germanium, physica status solidi (b) 15(2) (1966) 627-637. Doi:10.1002/pssb.19660150224

[14] J. Tauc, A. Menth, States in the gap, Journal of non-crystalline solids 8 (1972) 569-585. Doi:10.1016/0022-3093(72)90194-9

[15] D. Souri, Z.E. Tahan, A new method for the determination of optical band gap and the nature of optical transitions in semiconductors, Applied Physics B 119(2) (2015) 273-279. Doi:10.1007/s00340-015-6053-9

Chapter 3

Mechanochemical synthesis of $(Mg_{1-x}Fe_x)_2SiO_4$ olivine phases relevant to Martian regolith: structural and spectroscopic characterizations

Reproduced with kind permission from DeGruyter and upon approval of the co-authors.

Published in: Z. Kristallogr.

https://www.degruyter.com/document/doi/10.1515/zkri-2024-0078/html

Md. Izzuddin Jundullah Hanafi, M. Mangir Murshed*, Lars Robben, Thorsten M. Gesing

University of Bremen, Institute of Inorganic Chemistry and Crystallography, Leobener Straße 7, D-28359 Bremen, Germany

University of Bremen, MAPEX Center for Materials and Processes, Bibliothekstraße 1, D-28359 Bremen, Germany

*Corresponding author: e-mail: murshed@uni-bremen.de, phone: +49 (0)421 218 63144

ORCID:

MIJH: 0009-0005-7842-6751

MMM: 0000-0002-9063-372X

LR: 0000-0002-0534-9573

TMG: 0000-0002-4119-2219

Abstract

To fabricate metals from the base materials for future Mars exploration, synthesis of representative olivine phases and their structural and spectroscopic characterizations are of crucial importance. Using mechanochemical technique that mimics the mechanical weathering, a complete solid solution of $(Mg_{1-x}Fe_x)_2SiO_4$ has been synthesized to investigate the associated crystal chemical properties. X-ray powder diffraction data Rietveld analysis confirms that each polycrystalline sample crystallizes in space group *Pbnm*. The average crystallite size ranges between 80(1) nm and 223(4) nm. Each lattice parameter increases with increasing Fe-content due to the larger Fe^{2+} radius than that of Mg^{2+}, following Vegard's rule. For a given nominal chemical composition, substitution of Mg with Fe at the *M*1-site (4*a*: 0,0,0) is preferred to the *M*2-site (4*c*: *x*,*y*,¼). As a consequence, the average Fe-content lies slightly below the equivalence line for x = 0.2 – 0.8, indicating that the Fe/Mg ratio in the amorphous scattering content is most likely greater than unity. Characteristic Raman spectral features of the olivines have been explained in terms of the chemical composition (x). Simple regression models are demonstrated based on both X-ray diffraction and Raman spectroscopic data for the calculation of Mg/Fe in olivines. Diffuse reflectance UV/Vis spectra RATD analysis shows each olivine phase possesses direct band-gap between 3.38(3) eV and 4.90(3) eV. This study could keep valuable information to relevant databases for future human missions on Mars, in particular, for precise estimation of the representative olivines from the remote X-ray diffraction and spectroscopic data.

Keywords: Martian olivine, mechanochemical, X-ray, Raman, UV/Vis

1. Introduction

For years, the Martian surface has been an object of interest to a wide variety of researchers. Landers and rovers have been launched to investigate the chemical and mineralogical composition of the Martian soils, including remote and contact analysis [1]. In-situ X-ray diffraction data from the *Mars Science Laboratory* (MSL) on the rover *Curiosity* [2] suggested the composition of the Martian surface [3-5]. Ehlmann and Edwards [6] classified $(Mg,Fe)_2SiO_4$ olivines as primary minerals along with $(Ca,Na,K)(Al,Si)AlSi_2O_8$ feldspars and $(Ca,Mg,Fe)Si_2O_6$ pyroxenes. Assuming future human settlement on Mars, in-situ resource utilization (ISRU) of these olivines would be of great research attention as a base material to fabricate metals in future Mars exploration. As such, synthesis of representative olivines and their detailed structural and spectroscopic characterizations are of crucial importance, the more as full solid-solution powder data of olivine-type samples are still missing.

Earlier Martian meteorites investigations [7, 8] indicate the presence of mostly Mg-rich olivine and smaller number of Fe-rich one. Additionally, measured thermal infrared spectroscopic data [9] suggests that some olivine-bearing materials on the surface of Mars may be more Fe-rich than indicated by the Martian meteorites. Olivines are unevenly distributed in Martian surface [10]; Mg-rich olivines are predominantly found throughout the highland with some localized spots scattered in the northern plains [9, 10], whereas Fe-rich olivines are mainly found in the *Syrtis Major* area [11]. The olivine composition becomes progressively more Fe-rich from west to east across the *Nili Fossae* region [11], with global abundance of 22 wt-% – 30 wt-% [3, 4, 11]. Therefore, an investigation of the complete $(Mg_{1-x}Fe_x)_2SiO_4$ olivine-type solid solution is necessary to cover the wide range of olivine composition on Mars.

Olivine (M_2SiO_4) crystallizes in the orthorhombic space group *Pbnm* [12-14]. The crystal structure is shown in **Figure 1**, where *M* represents the divalent cations located at the center of the edge-sharing MO_6 octahedra. The isolated SiO_4 tetrahedra are connected to the MO_6 octahedra by sharing the oxygen vertices in the nesosilicate. The *M*-cations (Mg^{2+}, Fe^{2+}) are located on two non-equivalent octahedral sites, commonly named as *M*1- and *M*2- site. The *M*1-site belongs to the chain of edge-sharing octahedra running parallel to the crystallographic *c*-axis, having an inversion symmetry. The *M*2-site belongs to linking octahedra with a mirror symmetry [15]. The coordinated octahedra around *M*1 and *M*2 are not identical, and the latter ones are slightly larger than the former ones [16]. These olivines are assumed to form continuous solid solution between forsterite (Mg_2SiO_4) [17] and fayalite (Fe_2SiO_4) [18] with different Mg/Fe ratios [19].

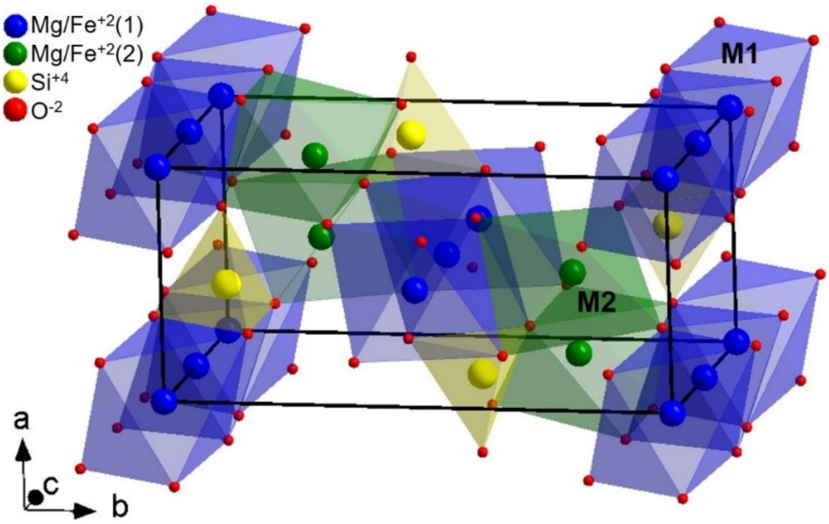

Figure 1. Crystal structure of $(Mg_{1-x}Fe_x)_2SiO_4$ olivine.

Many studies have been carried out on available natural and synthetic olivine single crystals with variable compositions [20-25]. Moreover, attempts to synthesize powder samples of both end-members have been reported earlier. Mechanochemical synthesis of Fe_2SiO_4 from stoichiometric mixtures of Fe, Fe_2O_3 and SiO_2 was employed by Sepelak et al. [26]. Similarly, Tavangarian and Emadi [27] also reported mechanochemical synthesis of Mg_2SiO_4 using talc ($Mg_3Si_4O_{10}(OH)_2$) and periclase (MgO). However, to the best of our knowledge, there are no reports on complete olivine-type solid-solution powders. The polycrystalline powder samples of a complete solid solution can better serve as representatives to characterize Martian olivine.

Additionally, factors such as high-energy impact and mechanical stress from ball milling can simulate the mechanical weathering [28], inducing mechanically-induced defects [29, 30], amorphous contents and crystallite size distributions of the Martian materials.

The present work is focused on the mechanochemical synthesis and the characterization of olivine-type $(Mg_{1-x}Fe_x)_2SiO_4$ for $x = 0 – 1.0$ with a chemical slice $\Delta x = 0.1$. Details of the structural features of each member of the solid solution have been characterized using X-ray powder diffraction (XRPD) followed by Rietveld analysis as well as Raman and UV/Vis diffuse reluctance spectroscopy.

2. Materials and methods

2.1. Synthesis

MgO (Merck > 97 %), Fe (Merck >97 %), Fe_2O_3 (Riedel-de Haën >99 %) and amorphous SiO_2 obtained from TEOS hydrolysis [31] were used as starting materials. Each olivine phase for a given composition ($x = 0 – 1.0$ with $\Delta x = 0.1$) of the $(Mg_{1-x}Fe_x)_2SiO_4$ solid solution was synthesized via ball milling with subsequent calcination at high temperature. A stoichiometric powder mixture with 10 wt-% of extra SiO_2 were mixed and ground together in an agate mortar. The extra amount of SiO_2 was necessary to overcome the gained mass from water absorption. The mixture was then placed in the grinding jar together with 10 g tungsten carbide (WC) balls. The powder was milled for 3 h with a rotational frequency of 15 Hz. Finally, the milled powder was collected from the grinding jar and heated in a corundum boat at 1373 K under forming gas (5 % H_2 / 95 % N_2) atmosphere for 6 h. The heating and cooling rate was set to 10 K/min and 5 K/min, respectively. Each obtained powder sample was hand ground in an agate mortar for further characterization.

2.2. X-ray powder diffraction

X-ray powder diffraction (XRPD) data collections were carried out on a Bruker D8 Discover diffractometer using CuK$_{\alpha 1,2}$ radiation ($\lambda_{K\alpha 1}$ = 154.05929(5) pm, $\lambda_{K\alpha 2}$ = 154.4414(2) pm) in Bragg–Brentano geometry. Data were collected at ambient condition from 5° to 85° 2θ with a step width of 0.0149° 2θ and a measurement time of 1.2 s per step. XRPD data Rietveld refinements were carried out using TOPAS V6.0 (Bruker AXS, Germany). During the Rietveld refinements, the background, sample displacement, metric, atomic positional and profile parameters were optimized. The amorphous fraction of the samples was quantified from the degree of crystallinity (DC) as implemented in the TOPAS software. For these calculations it was assumed that the average scattering power of the crystalline fraction of the sample was identical to that of the amorphous fraction. The latter one could consist of either glassy or quantum-crystalline (a few nanometric coherence length) contributions [32]. Using the fundamental parameter approach [33] with a used maximum observable average crystallite size (MOACS) of 290 nm for copper radiation, the apparent average crystallite size (ACS) was calculated from all the observed X-ray reflections, which is described as $L_{Vol}(IB)$ by the TOPAS suite. $L_{Vol}(IB)$ refers to the volume-weighted mean of the coherently diffracting domain size using the integral breadth for the description of the reflection profile. The respective pseudo-Voigt profile function was deconvoluted into Gaussian and Lorentzian components, describing the ACS and the micro-strain (ε_0), respectively. The information deduced during these (classical) Rietveld refinements are, except the DC, based on the appearance of the Bragg reflections and an ideal arrangement of atoms in a unit-cell only [34].

To confirm the average crystallite size without any restrictions of the Scherrer equation and to get further information of the crystallite size distribution, the obtained diffraction data are reduced on their $\lambda_{K\alpha 2}$ contribution and analyzed using the EnvACS approach [35]. As such, the X-ray diffraction data are converted to pair distribution function data using pdfgetx3 [36] followed by applying the Envelope model which combines the broadest and the narrowest possible distributions of the crystallites [37].

2.3. UV/Vis spectroscopy

The UV/Vis diffuse reflectance spectra were carried out using a UV-2600 spectrophotometer (Shimadzu, Japan) equipped with an ISR-2600 plus two-detector integrating sphere (Pike Technologies, USA). Barium sulphate ($BaSO_4$) powder was used as reference for the baseline correction. The data were collected from 190 nm to 850 nm with a step of 1 nm. Each spectral dataset is the mean-averaged of ten repetitions for a better signal/noise ratio. The change of the light source occurred at 323 nm. The Kubelka−Munk function [38] was implemented to approximate the optical absorption from the reflectance data. Direct and indirect band-gap energies were calculated using the Tauc method [39, 40] and compared with the value obtained from the “derivation of absorption spectrum fitting” (DASF) [41] method, which enable to determine the type of optical transition without presuming the nature of transition. The full analysis of band-gap transition type and band-gap energy is combined in the RATD (reflectance–absorbance–Tauc–DASF) analysis [32].

2.4. Raman spectroscopy

Raman spectra were recorded on a LabRam ARAMIS (Horiba Jobin – Yvon) micro-Raman spectrometer equipped with a green laser (λ_{ex} = 532 nm and < 20 mW). A 100x objective (Olympus) with a numerical aperture of 0.9 provides a focus spot of 721 nm diameter when closing the confocal hole to 200 µm. Each spectrum ranged between 100 cm^{-1} and 1000 cm^{-1} with a spectral resolution of approximately 1.2 cm^{-1} using a grating of 1800 grooves/mm and a thermoelectrically cooled CCD detector (Synapse, 1024 x 256 pixels).

3. Results and discussion

3.1. Sample formation

Conventional solid-state reactions only using mortar and pestle for sample homogenization were attempted as direct comparison with the proposed mechanochemical synthesis. These solid-state reactions yielded olivine-type phases of approximately 40 wt-% - 55 wt-% within the samples. On contrary, the mechanochemical synthesis leads to each $(Mg_{1-x}Fe_x)_2SiO_4$ olivine member to be > 99(1) wt-% phase pure. The trace impurities consist of unreacted precursors (MgO, Fe, SiO_2) and WC from the ball mill, which can form $FeWO_4$ upon calcination. While the end-member Mg_2SiO_4 appears to be white, the change of the color is clear with successive incorporation of Fe in the solid solution, as depicted in **Figure 2**.

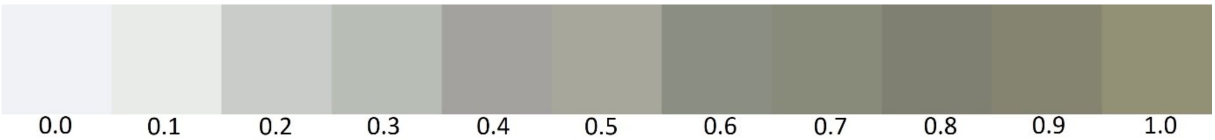

Figure 2. Photographic color of $(Mg_{1-x}Fe_x)_2SiO_4$ with respect to the chemical composition (x-values). Each picture was recorded with micro-USB camera, where the white-balance was corrected using $BaSO_4$ powder.

Mechanochemical synthesis utilize force to enhance required contact for initiating a chemical reaction [42]. During the ball milling process, the precursors are crushed between balls and accumulate potential energy, leading to bond breakage, defects and other changes on their surface [43]. Therefore, this process not only reduces the particle and crystallite size, but also enhances reactivity by generation of active sites [43]. In contrast to conventional solid-state reactions, mechanochemical synthesis allows control of energy input by adjusting milling frequency and time, hence results in better reproducibility. In the context of sustainability and green chemistry, mechanical activation is highly favorable due to its solvent-free conditions [44] as well as its role to shorten required calcination time. For instance, Redfern et al. [45] performed solid-state reactions which requires three periods of calcination at 1573 K for 4 h each with intermittent grinding and pelletization to synthesize $(MgFe)SiO_4$. Oppositely, the present mechanochemical synthesis requires only single calcination for 6 h even without pelletization. The mechanochemical activation and the short heating time most probably results in narrow crystallite size distribution with a broadening parameter of 0.1 [35], as shown in **Figure 3**. The endmember forsterite (Mg_2SiO_4) keeps an average crystallite size (ACS) of

77.8(7) nm obtained by the EnvACS approach [35]. Of notes, due to the narrow crystallite size distribution (**Fig. 3, top-inset**) the mode of the respective log-normal crystallite size distribution is obtained at 77.0(7) nm).

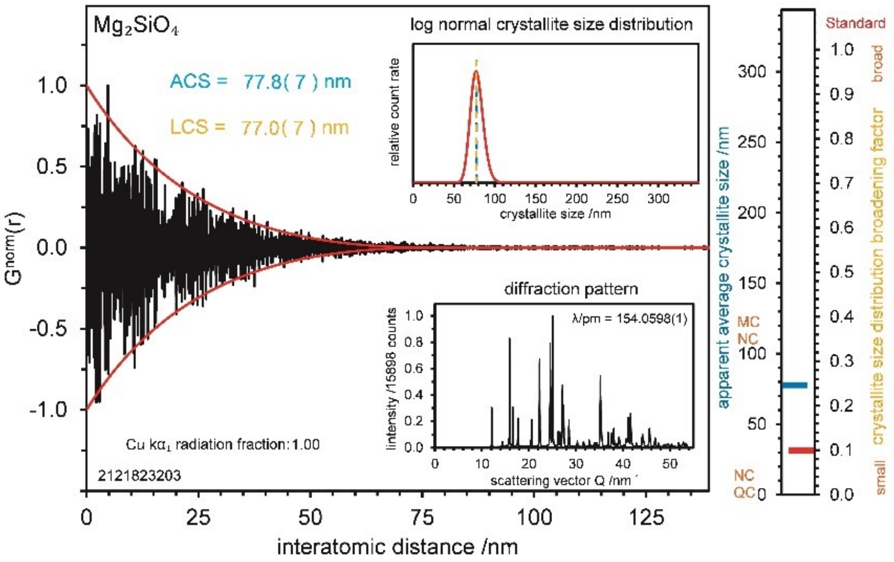

Figure 3. EnvACS analysis of Mg_2SiO_4. The envelope function (red) of the pair distribution function G(r) data (black) are given together with the values for the average crystallite size (ACS) and log-normal crystallite size maximum (LCS). Inserts show the log-normal distribution of the crystallites (top) and the collected background corrected diffraction data (bottom).

3.2. Crystal structure

X-ray powder diffraction (XRPD) data Rietveld analysis confirm that each polycrystalline sample crystallizes in space group *Pbnm* as also reported earlier [45]. A representative Rietveld plot of the $(Mg_{0.5}Fe_{0.5})_2SiO_4$ olivine is shown in **Figure 4**. The XRPD stack plots of all olivine phases can be compared in **Figure S1** (Supplementary Information). Rietveld refinements[1] indicate that Mg_2SiO_4 crystallizes with an ACS of approximately 80(1) nm, while the other end-member Fe_2SiO_4 with 164(3) nm.

There is hardly any trend for ACS of the synthesized $(Mg_{1-x}Fe_x)_2SiO_4$ olivine solid solution, as shown in **Figure 5**. In general, olivines with higher Fe-contents (x = 0.5 – 1.0) are likely to form larger crystallites (> 150 nm) whereas Mg-rich olivine tends to crystallize smaller (<150 nm),

---

[1] Further details of the crystal structural data will be available at the Fachinformationszentrum Karlsruhe with respective ICSD-numbers 2357288 – 2357298.

except *x* = 0.2. Earlier studies [19, 46-49] reported that the Fe-rich olivines can be synthesized with relatively lower calcination temperature, hence a bigger crystallite size is expected for the Fe-rich composition. The micro-strain shows an overall decreasing trend with increasing Fe-content. The synthesized olivines exhibit DC of 92 wt.-% – 97 wt.-%, suggesting diffuse scattering contributions by the associated amorphous contents. The amorphous fraction is relatively low compared to expected highly amorphous Martian regolith [50, 51]. A complete list of synthesized olivines and their XRPD characterization results is given in **Table 1**.

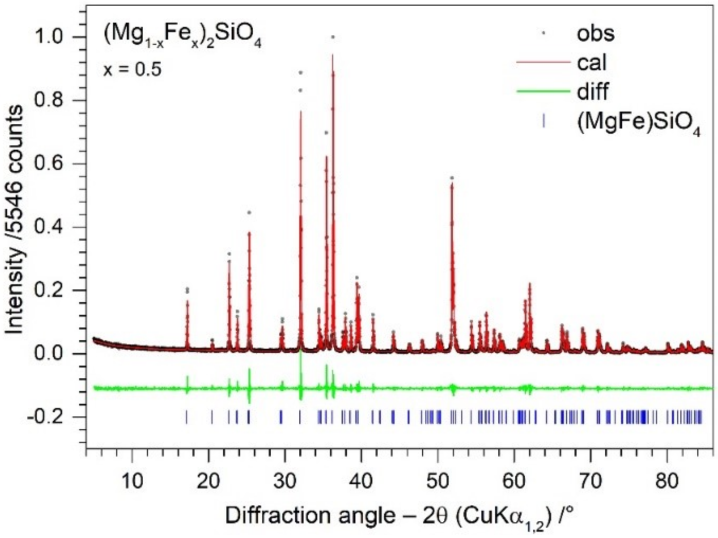

Figure 4. Representative X-ray powder data Rietveld plot of $(MgFe)SiO_4$.

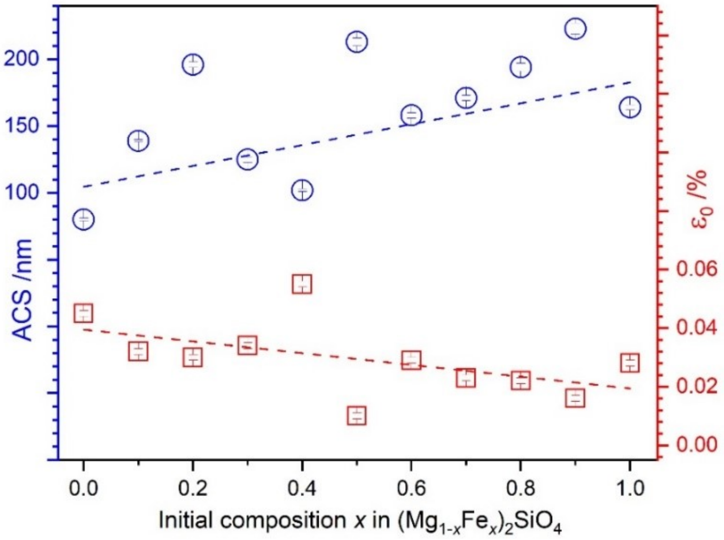

Figure 5. Changes of the average crystallite size (ACS) and microstrain (ε_0) with respect to chemical composition *x* in $(Mg_{1-x}Fe_x)_2SiO_4$. The given lines might be used as guidelines to the eye.

Table 1. Average crystallite size (ACS) and micro-strain (ε_0) of $(Mg_{1-x}Fe_x)_2SiO_4$ olivines along with the degree of crystallinity (DC) obtained from the XRPD data Rietveld refinements.

x	Phase fraction /wt.-%		ACS /nm	ε_0 /%	DC /%
0	Mg_2SiO_4	99.9(1)	80(1)	0.047(1)	97(5)
	MgO	0.1(1)			
0.1	$(Mg_{0.9}Fe_{0.1})_2SiO_4$	99.9(1)	139(1)	0.031(1)	95(5)
	MgO	0.1(1)			
0.2	$(Mg_{0.8}Fe_{0.2})_2SiO_4$	99.5(1)	196(2)	0.030(1)	96(5)
	MgO	0.4(1)			
	Fe	0.1(1)			
0.3	$(Mg_{0.7}Fe_{0.3})_2SiO_4$	99.1(1)	125(2)	0.035(1)	92(5)
	SiO_2 low quartz	0.7(1)			
	$FeWO_4$	0.2(1)			
0.4	$(Mg_{0.6}Fe_{0.4})_2SiO_4$	99.2(1)	102(1)	0.056(1)	97(5)
	MgO	0.8(1)			
0.5	$(Mg_{0.5}Fe_{0.5})_2SiO_4$	100.0(1)	213(3)	0.009(1)	97(5)
0.6	$(Mg_{0.4}Fe_{0.6})_2SiO_4$	99.4(1)	158(2)	0.030(1)	96(5)
	MgO	0.6(1)			
0.7	$(Mg_{0.3}Fe_{0.7})_2SiO_4$	99.1(1)	171(2)	0.022(1)	95(5)
	Fe	0.6(1)			
	MgO	0.3(1)			
0.8	$(Mg_{0.2}Fe_{0.8})_2SiO_4$	99.4(1)	194(3)	0.021(1)	96(5)
	$FeWO_4$	0.6(1)			
0.9	$(Mg_{0.1}Fe_{0.9})_2SiO_4$	99.7(1)	223(4)	0.018(1)	95(5)
	Fe	0.3(1)			
1	Fe_2SiO_4	99.8(1)	164(2)	0.028(1)	96(5)
	$FeWO_4$	0.2(1)			

The metric parameters of the two end-members Mg_2SiO_4 and Fe_2SiO_4 are in good agreement with those of the reported values of forsterite [13, 52, 53] and fayalite [49, 54, 55], respectively. The partial substitution of Mg^{2+} with Fe^{2+} cation leads to an elongation of each lattice parameter, eventually to larger unit cell volume, following Vegard's rule, as shown in **Figure 6**. The expansion of the metric parameters can be explained due to larger Fe^{2+} (78 pm) radius than that of Mg^{2+} (72 pm) [56] for octahedral coordination.

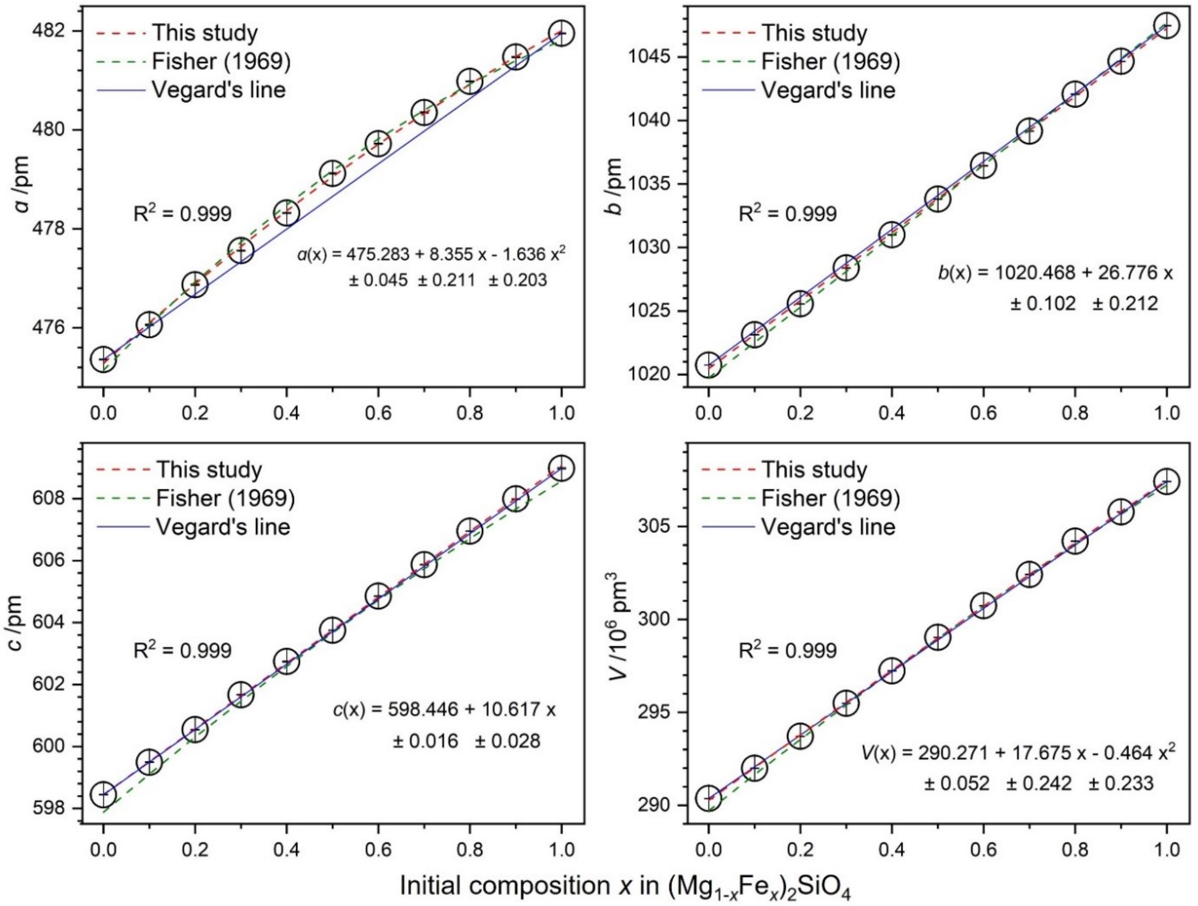

Figure 6. Evolution of the metric parameters while changing the compositional *x* in $(Mg_{1-x}Fe_x)_2SiO_4$.

The observed *a*-lattice parameter is slightly larger than its proportionate sum of the end member parameters, which follows the quadratic equation: $\mathrm{a}(x) = 482.00 - 5.08\,(1-x) - 1.64\,(1-x)^2$, for the compositional *x*-variable in $(Mg_{1-x}Fe_x)_2SiO_4$. The fit of the lattice parameter *a* for any given *x*-value lies close to that of the model line suggested by Fisher and Medaris [57]: $\mathrm{a}(x) = 481.81 - 3.86\,(1-x) - 2.81\,(1-x)^2$, where the compositional *x* is calculated from the d_{130}-spacing as: $\mathrm{x} = 15.8113\sqrt{3.0358 - \mathrm{d}_{130}} - 7.2250.$ The elongation of the lattice parameter *a* is influenced by the *M*1 octahedra and their linkage via SiO_4 tetrahedra. The *M*1 octahedra are slightly more distorted than *M*2 [58]. The size and distortion differences arise from the fact that the *M*1 octahedra have twice as many shared edges as *M*2 [58]. The metric parameter *b* can be fitted with the linear function: $b(x) = 1020.468 + 26.776\,x$, which is also in good agreement with the Fisher and Medaris model [57]. However, rather a different regression plot is observed for the *c* lattice parameter. While Fisher and Medaris [57] reported that *c* lattice parameter follows an exponential fit, this study suggests a linear fit. The model equations for the metric parameters are summarized in **Table 2**.

Table 2. Regression equations of $(Mg_{1-x}Fe_x)_2SiO_4$ olivine X-ray data Rietveld refined metric parameters against the chemical composition variable *x*. For comparison, equations of Fisher and Medaris (FM) [57] are listed as well.

Metric	This study	FM [57]
a /pm	$475.28 + 8.35\ x - 1.64\ x^2$ $482.00 - 5.08\ (1-x) - 1.64\ (1-x)^2$	$481.81 - 3.86\ (1-x) - 2.81\ (1-x)^2$
b /pm	$1020.47 + 26.78\ x$ $1047.24 - 26.78\ (1-x)$	$1047.67 - 27.94\ (1-x)$
c /pm	$598.45 + 10.62\ x$ $609.06 - 10.62\ (1-x)$	$608.57 - 8.90\ (1-x) - 1.79\ (1-x)^2$
V /10^6 pm^3	$290.27 + 17.67\ x - 0.46\ x^2$ $307.48 - 16.75\ (1-x) - 0.46\ (1-x)^2$	$307.23 - 15.49\ (1-x) - 2.02\ (1-x)^2$

The bond distances and bond valence sums (BVSs) [59] are given in **Table S1**. The *M*(1)-O and *M*(2)-O bond distances slightly differ due to different ionicity of the *M*-sites. As such, the <Mg(1)-O> bond length is slightly shorter than that of <Mg(2)-O> [13]. The isomorphic substitution of Mg^{2+} with Fe^{2+} gradually increases the average bond lengths for both *M*-sites, as seen in **Figure 7**. However, a slight discrepancy can be seen at $x = 0.9$ where both the <*M*(1)-O> and <*M*(2)-O> slightly depart from the respective linear trend. The *M*-site ionicity also play roles for the linked SiO_4 tetrahedra, eventually to <Si-O> lengths. The end-members keep a shorter <Si-O> distance, which exhibits slightly longer values for the mid-range *x*-values. The changes of the $M(1)O_6$, $M(2)O_6$ and SiO_4 polyhedral volumes with respect to compositional *x*-value are shown in **Figure S2**. The structural BVS of Mg/Fe fluctuates between 1.80(1) v.u. and 2.02(1) v.u., suggesting that the *M*-cations stay close to the formal oxidation state of 2+.

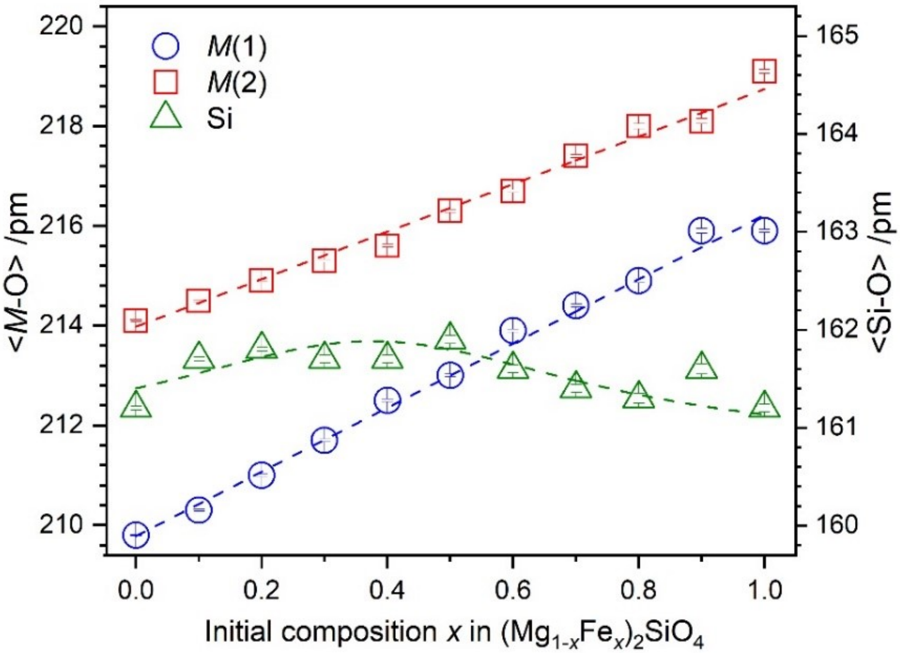

Figure 7. Evolution of the average bond distances with respect to feed composition *x* in $(Mg_{1-x}Fe_x)_2SiO_4$.

For a given nominal *x*-value, substitution of Mg with Fe at the *M*1-site (4*a*: 0,0,0) is preferred against the *M*2-site (4*c*: *x*,*y*,¼). For instance, for *x* = 0.5, the Fe/Mg ratio at the *M*1- and *M*2-site is found to be 1 and 0.75, respectively. As such, the average Fe-content lies below the equivalence line for *x* = 0.2 – 0.8, as shown in **Figure 8**, indicating the Fe/Mg ratio in the amorphous scattering content is most likely greater than unity. The preference of Fe^{2+} to the *M*1-site agrees well to earlier reports, for instance, of Morozov et al. [60] supported by ^{57}Fe Mössbauer spectroscopy, and of Heinemann et al. [61] studied by X-ray diffraction. Under a given reaction condition, cations with larger ionic radii usually prefer larger octahedral sites. However, the Fe^{2+} cations occupy the smaller but distorted *M*1-sites due to preferable crystal field stabilization energy (CFSE) [58, 62]. That is, between these two crystal chemical principles, the CFSE predominately controls the occupancy of Fe^{2+} cations in the *M*1-sites. The detail site occupancy factors are listed in **Table S2**. To get access to the *in-situ* evaluation of the iron content in the mineral phases, for instance, while exploring the Mars surface, an easy approach would be to analyze the X-ray diffraction data in a range where the intensity strongly depends on the Mg/Fe ratio. As such, the 2theta (CuK_{α} radiation) range between 22.2°

and 26.3° serves for the purpose, as shown in **Figure 8**, also visible in **Figure S1**. In this region, there are (021: 0*kl*) as well as (101), (111) and (120) (categorized as 1*kl*) reflections. Using a profile fitting (**Fig. 8**) the intensities of the (021) reflection ($\Sigma(I_1)$) and those of the (111) plus (120) reflections ($\Sigma(I_2)$) can be expressed as: $R_I(fit) = ln(\Sigma(I_1)/\Sigma(I_2))$. The Fe-content ($x$) thus could be directly calculated (**Fig. 8**) from the X-ray diffraction pattern using the expression: $x(Fe) = (0.646 - R_I(fit))/2.717$. The reverse calculations result in an average error of only 0.6 mol-%. Indeed, in this way a precise compositional x-value for $(Mg_{1-x}Fe_x)_2SiO_4$ can be calculated. Another simple expression: $R_I(sum) = ln(\Sigma(I_1)/\Sigma(I_2))$ has been also tested, where $\Sigma(I_1)$) and $\Sigma(I_2)$), respectively refer to summed over intensity from 22.2° to 23.2° (0*kl* range as $\Sigma(I_1)$) and from 23.2° to 26.3° 2Theta (1*kl* range as $\Sigma(I_2)$) for CuK_α radiation. With such mathematically ease this approach still offers a linear regression for the calculation of the Fe-content in the olivine solution: $x(Fe) = -R_I(sum)/1.5625$. This simple approach shows an average deviation of the expected Fe-content of less than 1 mol-%. Of notes, this second approach is only possible for phase pure (single phase) X-ray reflections in the given 2theta region. Should reflection overlapping occur for additional phases, only Rietveld refinement can give accurate information.

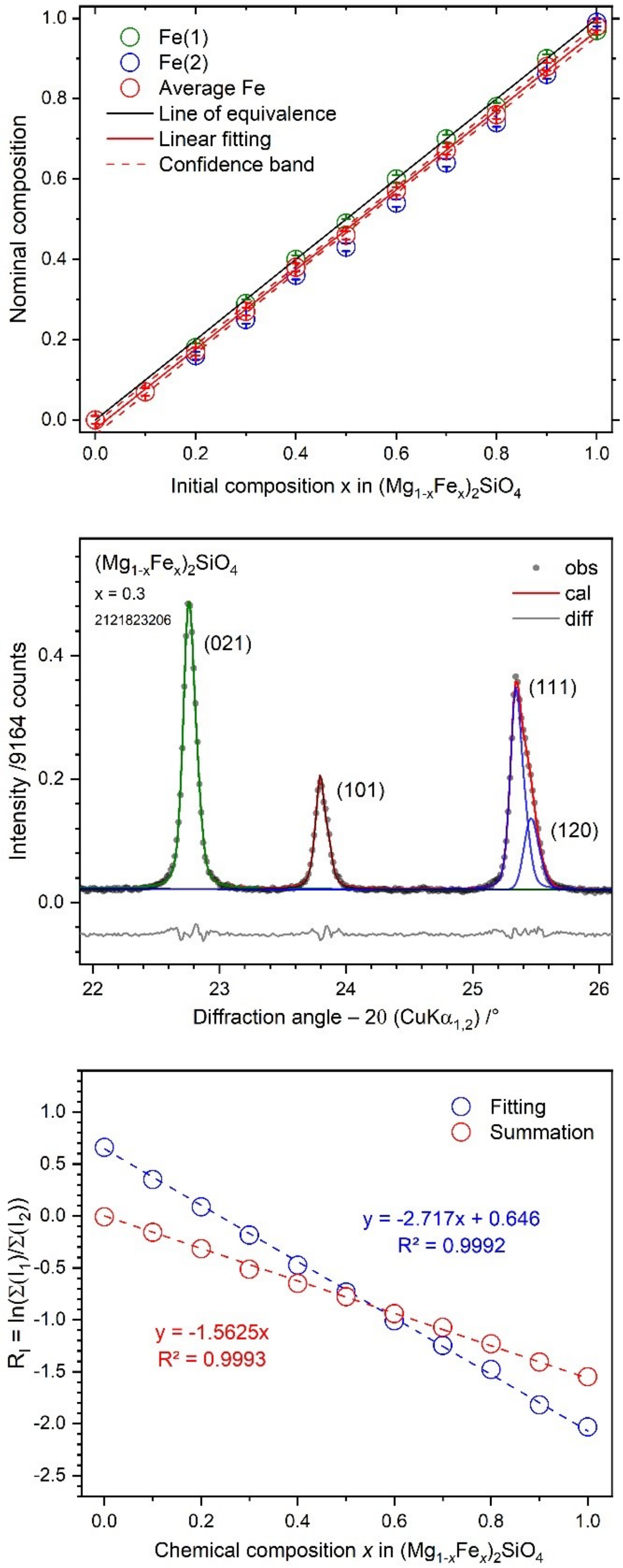

Figure 8. Refined site occupancy factors of Fe(1), Fe(2) and their average in $(Mg_{1-x}Fe_x)_2SiO_4$ olivine (top), analysis range based on X-ray reflection intensity (see text) for Fe-content (middle). Two linear regression lines represent the peak fitted intensity (blue) and the summed intensity ration (red) in a chosen range.

3.3. Raman spectroscopy

Raman spectra of $(Mg_{1-x}Fe_x)_2SiO_4$ olivines are shown as stack plots in **Figure 9**. A representative peak fitting is shown in **Figure S3**. Partial substitution of Mg^{2+} with Fe^{2+} leads to global red-shifts of the optical modes, as shown in **Figure 10**, which can be explained by the quasi-harmonic approach as Fe^{2+} possess bigger ionic radii [56] than that of Mg^{2+}.

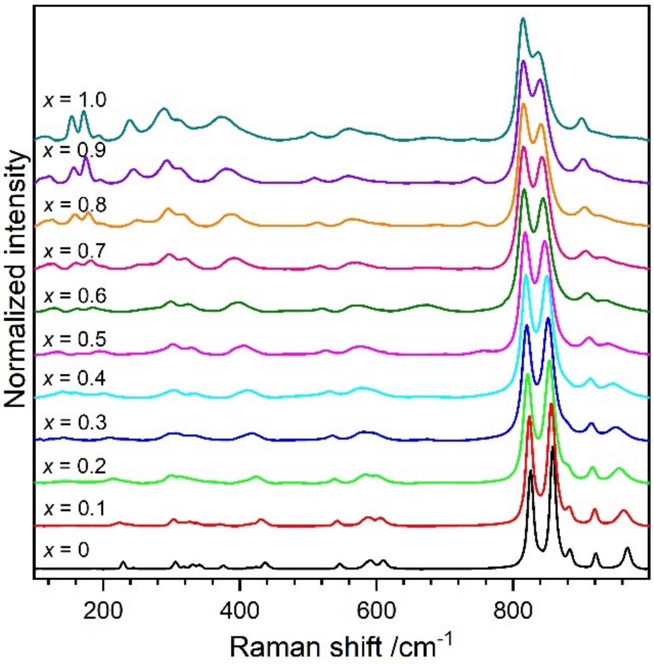

Figure 9. Raman spectra of olivines collected at ambient condition for $(Mg_{1-x}Fe_x)_2SiO_4$.

Factor group analysis predicts 36 Raman-active modes (11 A_g + 11 B_{1g} + 7 B_{2g} + 7 B_{3g}) [63, 64]. Typically, Raman spectra of olivine can be catagorized into three regions: < 400 cm^{-1}, 400 cm^{-1} - 700 cm^{-1} and > 700 cm^{-1}. The high-frequency region (> 700 cm^{-1}) can be attributed to the internal Si-O stretching vibrations of the SiO_4 tetrahedra [65, 66]. The dominant feature of the olivine Raman spectra are two intense modes observed between 815 cm^{-1} - 826 cm^{-1} and 838 cm^{-1} - 858 cm^{-1}, in agreement with previous reports [66-69]. The lower wavenumber mode follows a general red-shift trend until $x = 0.7$ and remain constant at 815.5(2) cm^{-1} for the higher Fe-content members. The mode at 858 cm^{-1} follows a linear trend for the frequency: $R(x) = 857.6(5) - 20.2(1)\,x$, for the compositional x-value in $(Mg_{1-x}Fe_x)_2SiO_4$. The mid-range modes (400 cm^{-1} - 700 cm^{-1}) show weaker intensities than those in the high-frequency region presumably due to respective lower Raman scattering cross-section. The spectral intensity in this region is mainly contributed by the bending motion of the *M*(2) with oxygen [65]. The frequency of two modes can be fitted with the linear functions: $R(x) = 546.9(2) - 42.1(1)\,x$ and $R(x) = 437.3(3) - 62.7(1)\,x$. The low-frequency region (< 400 cm^{-1}) is attributed to the vibrational modes of Mg/Fe with negligible contributions from the lighter silicon [65, 66]. While any trend line cannot be formulated for the low-frequency modes, the olivine composition can be reasonably predicted. The Fe-rich olivines ($x \geq 0.6$) show two doublets resolved at 155 cm^{-1} - 161 cm^{-1} and 175 cm^{-1} - 185 cm^{-1}, while Mg-rich olivines ($x \leq 0.1$) exhibit characteristic modes at 223 cm^{-1} - 228 cm^{-1}. Any noticeable changes in this low-frequency region can be associated with the substitution of the lighter Mg by the heavier Fe in the octahedral sites. **Table 3** summarized regression equations of $(Mg_{1-x}Fe_x)_2SiO_4$ olivine Raman spectroscopic peaks, which can well predict the olivine composition on the Martian surface.

Table 3. Selective regression equations of $(Mg_{1-x}Fe_x)_2SiO_4$ olivine Raman spectroscopic peaks.

Linear fitting equation	Assignment
$R(x) = 920.7(3) - 19.9(1)\,x$	B_{2g}
$R(x) = 857.6(5) - 20.2(1)\,x$	A_g
$R(x) = 546.9(2) - 42.1(1)\,x$	A_g
$R(x) = 437.3(3) - 62.7(1)\,x$	B_{1g}

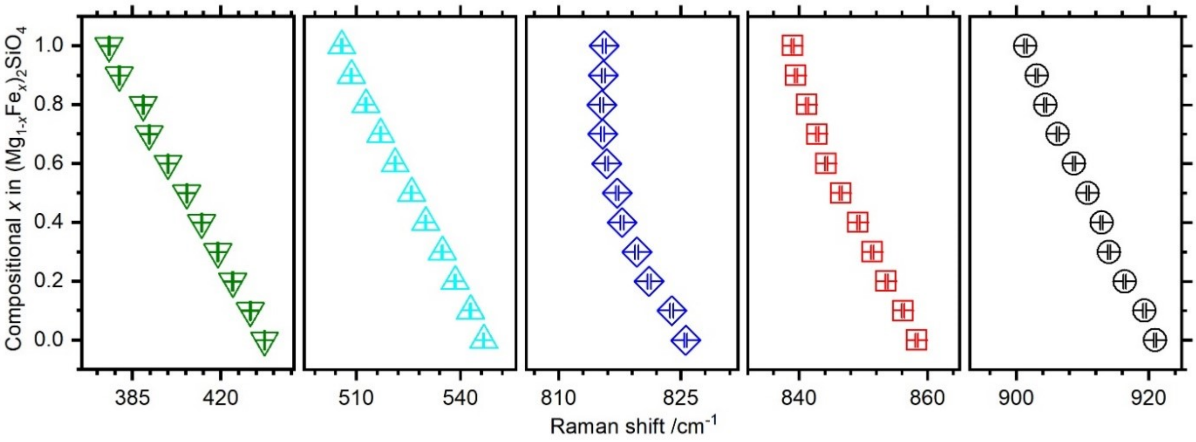

Figure 10. Selective Raman spectroscopic peak shifts with respect to compositional *x* in $(Mg_{1-x}Fe_x)_2SiO_4$ olivine.

3.4. UV/Vis spectroscopy

The optical properties of the olivine series $(Mg_{1-x}Fe_x)_2SiO_4$ are studied by UV/Vis diffuse reflectance spectroscopy to determine their optical band-gap energy. The RATD analysis [32] determines the nature of transition, as shown in **Figure S4**. The complete UV/Vis RATD analysis fit values are summarized in **Table S3**. Using the DASF method, the band-gap energy (E_g) of 4.90(3) and 3.38(3) eV are calculated for Mg_2SiO_4 and Fe_2SiO_4, respectively. On the other hand, the conventional Tauc method [39, 40] predicted the direct transition energy (E_d) of 4.75(3) and 3.46(3) eV and, the indirect transition energy (E_i) of 3.68(3) and 2.99(3) eV for Mg_2SiO_4 and Fe_2SiO_4, respectively. The closeness between E_g and E_d values suggests that the electronic band gap most likely arises from the respective direct transition. The nature and band-gap transition energy of Mg_2SiO_4 agrees well to the electronic band structure demonstrated by Yang and Zhan [70]. However, our experimental findings of Fe_2SiO_4 is clearly different from that of calculated by generalized gradient approximation (GGA) [71, 72] and Xiao et al. [73] as well. A low-intense transition peak can be seen between 1.5 eV – 1.8 eV for each Fe-containing olivine, which can be explained due to the d-d transition of Fe^{2+} within the $3d^6$ configuration [74]. **Figure 11** illustrates a decrease in the band-gap energy values upon increasing the Fe-content in the olivine series.

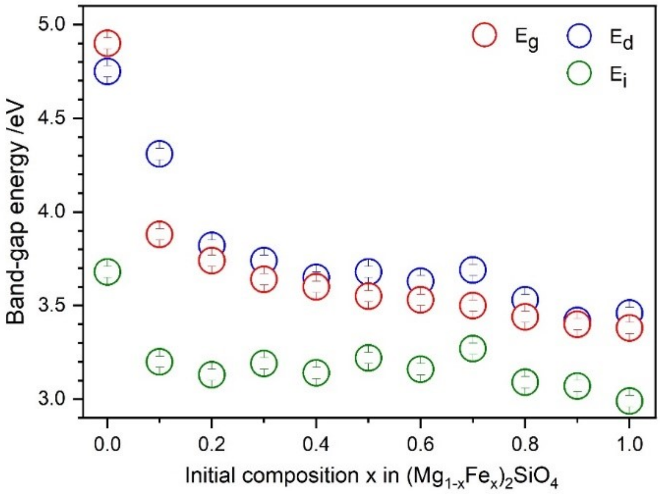

Figure 11. Change of band-gap energy (E_g) with respect to the chemical composition *x* in $(Mg_{1-x}Fe_x)_2SiO_4$, showing respective direct (E_d) and indirect (E_i) electron transfer to the conduction band.

4. Summary and outlook

The olivine-type $(Mg_{1-x}Fe_x)_2SiO_4$ solid solution was successfully synthesized by ball milling with subsequent calcination. Structural analysis was performed on X-ray powder diffraction data by means of Rietveld refinements. The synthesized olivines exhibit degrees of crystallinity of 92 wt.-% – 97 wt.-%, suggesting relatively low amount of the amorphous scattering contents. Olivines with higher Fe content ($x = 0.5$ - 1) are likely to form larger crystallites (> 150 nm). Substitution of Mg with Fe on the *M*1-site (4*a*: 0,0,0) is preferred against the as well octahedrally coordinated *M*2-site (4*c*: *x*,*y*,¼). Beside the Rietveld refinement, regression equations are demonstrated based on the X-ray reflection intensity for easy calculation of Mg/Fe-concentration in olivines on the Martian surface. Regression approach is also suggested for the characteristic Raman modes of olivines. The electronic band gap has been analyzed from the diffuse reflectance UV/Vis spectra. The present study offers a step forward characterizing tool to quantify similar olivines, or olivine component in multi-phase Martian regolith. Nevertheless, further investigations on relevant olivines with higher amorphous content is of crucial importance to better represent the Martian regolith.

ACKNOWLEDGEMENT

We acknowledge support by the state of Bremen within the “Humans on Mars” initiative for APF “Materials on demand” S1P3.

Reference

[1] A. Udry, G.H. Howarth, C.D.K. Herd, J.M.D. Day, T.J. Lapen, J. Filiberto, What Martian Meteorites Reveal About the Interior and Surface of Mars, Journal of Geophysical Research-Planets 125(12) (2020). Doi:10.1029/2020je006523

[2] J.P. Grotzinger, J. Crisp, A.R. Vasavada, R.C. Anderson, C.J. Baker, R. Barry, D.F. Blake, P. Conrad, K.S. Edgett, B. Ferdowski, R. Gellert, J.B. Gilbert, M. Golombek, J. Gómez-Elvira, D.M. Hassler, L. Jandura, M. Litvak, P. Mahaffy, J. Maki, M. Meyer, M.C. Malin, I. Mitrofanov, J.J. Simmonds, D. Vaniman, R.V. Welch, R.C. Wiens, Mars Science Laboratory Mission and Science Investigation, Space Science Reviews 170(1-4) (2012) 5-56. Doi:10.1007/s11214-012-9892-2

[3] D.L. Bish, D.F. Blake, D.T. Vaniman, S.J. Chipera, R.V. Morris, D.W. Ming, A.H. Treiman, P. Sarrazin, S.M. Morrison, R.T. Downs, C.N. Achilles, A.S. Yen, T.F. Bristow, J.A. Crisp, J.M. Morookian, J.D. Farmer, E.B. Rampe, E.M. Stolper, N. Spanovich, X-ray Diffraction Results from Mars Science Laboratory: Mineralogy of Rocknest at Gale Crater, Science 341(6153) (2013) 1238932. Doi:10.1126/science.1238932

[4] C.N. Achilles, R.T. Downs, D.W. Ming, E.B. Rampe, R.V. Morris, A.H. Treiman, S.M. Morrison, D.F. Blake, D.T. Vaniman, R.C. Ewing, S.J. Chipera, A.S. Yen, T.F. Bristow, B.L. Ehlmann, R. Gellert, R.M. Hazen, K.V. Fendrich, P.I. Craig, J.P. Grotzinger, D.J. Des Marais, J.D. Farmer, P.C. Sarrazin, J.M. Morookian, Mineralogy of an active eolian sediment from the Namib dune, Gale crater, Mars, Journal of Geophysical Research: Planets 122(11) (2017) 2344-2361. Doi:10.1002/2017je005262

[5] D.T. Vaniman, D.L. Bish, D.W. Ming, T.F. Bristow, R.V. Morris, D.F. Blake, S.J. Chipera, S.M. Morrison, A.H. Treiman, E.B. Rampe, M. Rice, C.N. Achilles, J.P. Grotzinger, S.M. McLennan, J. Williams, J.F.I. Bell, H.E. Newsom, R.T. Downs, S. Maurice, P. Sarrazin, A.S. Yen, J.M. Morookian, J.D. Farmer, K. Stack, R.E. Milliken, B.L. Ehlmann, D.Y. Sumner, G. Berger, J.A. Crisp, J.A. Hurowitz, R. Anderson, D.J. Des Marais, E.M. Stolper, K.S. Edgett, S. Gupta, N. Spanovich, M.S. Team, Mineralogy of a Mudstone at Yellowknife Bay, Gale Crater, Mars, Science 343 (2014). Doi:10.1126/science.1243480.

[6] B.L. Ehlmann, C.S. Edwards, Mineralogy of the Martian surface, Annual Review of Earth and Planetary Sciences 42 (2014) 291-315. Doi:10.1146/annurev-earth-060313-055024

[7] J. Papike, J. Karner, C. Shearer, P. Burger, Silicate mineralogy of martian meteorites, Geochimica et Cosmochimica Acta 73(24) (2009) 7443-7485. Doi:10.1016/j.gca.2009.09.008

[8] A. Peslier, D. Hnatyshin, C.D. Herd, E.L. Walton, A.D. Brandon, T. Lapen, J. Shafer, Crystallization, melt inclusion, and redox history of a Martian meteorite: Olivine-phyric shergottite Larkman Nunatak 06319, Geochimica et Cosmochimica Acta 74(15) (2010) 4543-4576. Doi:10.1016/j.gca.2010.05.002

[9] W.C. Koeppen, V.E. Hamilton, Global distribution, composition, and abundance of olivine on the surface of Mars from thermal infrared data, Journal of Geophysical Research: Planets 113(E5) (2008). Doi:10.1029/2007JE002984

[10] A. Ody, F. Poulet, J.P. Bibring, D. Loizeau, J. Carter, B. Gondet, Y. Langevin, Global investigation of olivine on Mars: Insights into crust and mantle compositions, Journal of Geophysical Research: Planets 118(2) (2013) 234-262. Doi:10.1029/2012JE004149

[11] H.Y. McSween, M.B. Wyatt, R. Gellert, J.F. Bell III, R.V. Morris, K.E. Herkenhoff, L.S. Crumpler, K.A. Milam, K.R. Stockstill, L.L. Tornabene, Characterization and petrologic interpretation of olivine-rich basalts at Gusev Crater, Mars, Journal of Geophysical Research: Planets 111(E2) (2006). Doi:10.1029/2005JE002477

[12] M. Müller-Sommer, R. Hock, A. Kirfel, Rietveld refinement study of the cation distribution in (Co, Mg)-olivine solid solution, Physics and Chemistry of Minerals 24(1) (1997) 17-23. Doi:10.1007/s002690050013

[13] K. Fujino, S. Sasaki, Y. Takeuchi, R. Sadanaga, X-ray determination of electron distributions in forsterite, fayalite and tephroite, Acta Crystallographica Section B 37(3) (1981) 513-518. Doi:10.1107/S0567740881003506

[14] G.A. Lager, F.K. Ross, F.J. Rotella, J.D. Jorgensen, Neutron powder diffraction of forsterite, Mg_2SiO_4: a comparison with single-crystal investigations, Journal of Applied Crystallography 14(2) (1981) 137-139. Doi:10.1107/S0021889881008935

[15] H. Yang, J. Shi, M. Gong, K.W. Cheah, Synthesis and photoluminescence of Eu^{3+}- or Tb^{3+}-doped Mg_2SiO_4 nanoparticles prepared by a combined novel approach, Journal of Luminescence 118(2) (2006) 257-264. Doi:10.1016/j.jlumin.2005.09.005

[16] S. Demouchy, Defects in olivine, Eur. J. Mineral. 33(3) (2021) 249-282. Doi:10.5194/ejm-33-249-2021

[17] N.L. Bowen, The ternary system; diopside-forsterite-silica, American Journal of Science 4(225) (1914) 207-264.

[18] A. Lacroix, A fayalite rock, Comptes Rendus Hebdomadaires Des Seances De L Academie Des Sciences 130 (1900) 1778-1780.

[19] O. Qafoku, E.S. Ilton, M.E. Bowden, L. Kovarik, X. Zhang, R.K. Kukkadapu, M.H. Engelhard, C.J. Thompson, H.T. Schaef, B.P. McGrail, Synthesis of nanometer-sized fayalite and magnesium-iron (II) mixture olivines, Journal of colloid and interface science 515 (2018) 129-138. Doi:10.1016/j.jcis.2018.01.036

[20] T. Mouri, M. Enami, Raman spectroscopic study of olivine-group minerals, Journal of Mineralogical and Petrological Sciences 103(2) (2008) 100-104. Doi:10.2465/jmps.071015

[21] Y. Sumino, O. Nishizawa, T. Goto, I. Ohno, M. Ozima, Temperature variation of elastic constants of single-crystal forsterite between -190° and 400°C, Journal of Physics of the Earth 25(4) (1977) 377-392. Doi:10.4294/jpe1952.25.377

[22] Y. Sumino, The elastic constants of Mn_2SiO_4, Fe_2SiO_4 and Co_2SiO_4, and the elastic properties of olivine group minerals at high temperature, Journal of Physics of the Earth 27(3) (1979) 209-238. Doi:10.4294/jpe1952.27.209

[23] B. Kolesov, C. Geiger, A Raman spectroscopic study of Fe–Mg olivines, Physics and Chemistry of Minerals 31(3) (2004) 142-154. Doi:10.1007/s00269-003-0370-y

[24] Z. Mao, D. Fan, J.-F. Lin, J. Yang, S.N. Tkachev, K. Zhuravlev, V.B. Prakapenka, Elasticity of single-crystal olivine at high pressures and temperatures, Earth and Planetary Science Letters 426 (2015) 204-215. Doi:10.1016/j.epsl.2015.06.045

[25] P. Raterron, E. Amiguet, J. Chen, L. Li, P. Cordier, Experimental deformation of olivine single crystals at mantle pressures and temperatures, Physics of the Earth and Planetary Interiors 172(1-2) (2009) 74-83. Doi:10.1016/j.pepi.2008.07.026

[26] V. Sepelak, M. Myndyk, M. Fabian, K.L. Da Silva, A. Feldhoff, D. Menzel, M. Ghafari, H. Hahn, P. Heitjans, K.D. Becker, Mechanosynthesis of nanocrystalline fayalite, Fe_2SiO_4, Chem Commun (Camb) 48(90) (2012) 11121-3. Doi:10.1039/c2cc36370d

[27] F. Tavangarian, R. Emadi, Synthesis of nanocrystalline forsterite (Mg_2SiO_4) powder by combined mechanical activation and thermal treatment, Materials Research Bulletin 45(4) (2010) 388-391. Doi:10.1016/j.materresbull.2009.12.032

[28] M.-C.M. Eppes, Mechanical Weathering: A Conceptual Overview, Treatise on Geomorphology 3 (2022) 30-45. Doi:10.1016/B978-0-12-818234- 5.00200-5

[29] J. López-García, V. Sánchez-Alarcos, V. Recarte, J.A. Rodríguez-Velamazán, I. Unzueta, J. García, F. Plazaola, P. La Roca, J. Pérez-Landazábal, Effect of high-energy ball-milling on the magnetostructural properties of a Ni45Co5Mn35Sn15 alloy, Journal of Alloys and Compounds 858 (2021) 158350. Doi:10.1016/j.jallcom.2020.158350

[30] W. Ashraf, A. Khan, S. Bansal, M. Khanuja, Mechanical ball milling: A sustainable route to induce structural transformations in tungsten disulfide for its photocatalytic applications, Physica E: Low-dimensional Systems and Nanostructures 140 (2022) 115152. Doi:10.1016/j.physe.2022.115152

[31] D. Qi, C. Lin, H. Zhao, H. Liu, T. Lü, Size regulation and prediction of the SiO_2 nanoparticles prepared via Stöber process, Journal of Dispersion Science and Technology 38(1) (2017) 70-74. Doi:10.1080/01932691.2016.1143373

[32] T.M. Gesing, M.M. Murshed, S. Schuh, O. Thüringer, K. Krämer, T. Neudecker, C.B. Mendive, L. Robben, Nano-crystalline precursor formation, stability, and transformation to mullite-type visible-light photocatalysts, Journal of Materials Science 57 (2022) 1-20. Doi:10.1007/s10853-022-07854-w

[33] J.P. Cline, D.R. Black, D. Gil, A. Henins, D. Windover, The application of the fundamental parameters approach as implemented in TOPAS to divergent beam powder diffraction data, Materials Science Forum 651 (2010) 201-219. Doi:10.4028/www.scientific.net/MSF.651.201

[34] H.M. Rietveld, A profile refinement method for nuclear and magnetic structures, Journal of applied Crystallography 2(2) (1969) 65-71. Doi:10.1107/S0021889869006558

[35] T.M. Gesing, L. Robben, Determination of the average crystallite size and the crystallite size distribution: The envelope function approach EnvACS, Journal of Applied Crystallography (2024) Doi:10.1107/S1600576724007362

[36] P. Juhás, T. Davis, C.L. Farrow, S.J. Billinge, PDFgetX3: a rapid and highly automatable program for processing powder diffraction data into total scattering pair distribution functions, Journal of Applied Crystallography 46(2) (2013) 560-566. Doi:10.1107/S0021889813005190

[37] R.C. Howell, T. Proffen, S.D. Conradson, Pair distribution function and structure factor of spherical particles, Physical Review B 73(9) (2006) 094107. Doi:10.1103/PhysRevB.73.094107

[38] P. Kubelka, Ein beitrag zur optik der farbanstriche, Z. tech. Phys 12 (1931) 593-601.

[39] J. Tauc, R. Grigorovici, A. Vancu, Optical Properties and Electronic Structure of Amorphous Germanium, physica status solidi (b) 15(2) (1966) 627-637. Doi:10.1002/pssb.19660150224

[40] J. Tauc, A. Menth, States in the gap, Journal of non-crystalline solids 8 (1972) 569-585. Doi:10.1016/0022-3093(72)90194-9

[41] D. Souri, Z.E. Tahan, A new method for the determination of optical band gap and the nature of optical transitions in semiconductors, Applied Physics B 119(2) (2015) 273-279. Doi:10.1007/s00340-015-6053-9

[42] A. Nasser, U. Mingelgrin, Mechanochemistry: A review of surface reactions and environmental applications, Applied Clay Science 67 (2012) 141-150. Doi:10.1016/j.clay.2011.11.018

[43] B. Szczęśniak, S. Borysiuk, J. Choma, M. Jaroniec, Mechanochemical synthesis of highly porous materials, Materials Horizons 7(6) (2020) 1457-1473. Doi:10.1039/D0MH00081G

[44] M. Leonardi, M. Villacampa, J.C. Menéndez, Multicomponent mechanochemical synthesis, Chemical Science 9(8) (2018) 2042-2064. Doi:10.1039/C7SC05370C

[45] S.A.T. Redfern, G. Artioli, R. Rinaldi, C.M.B. Henderson, K.S. Knight, B.J. Wood, Octahedral cation ordering in olivine at high temperature. II: an in situ neutron powder diffraction study on synthetic $MgFeSiO_4$ (Fa50), Physics and Chemistry of Minerals 27(9) (2000) 630-637. Doi:10.1007/s002690000109

[46] M.H. Fathi, M. Kharaziha, Mechanically activated crystallization of phase pure nanocrystalline forsterite powders, Materials Letters 62(27) (2008) 4306-4309. Doi:10.1016/j.matlet.2008.07.015

[47] S. Ni, L. Chou, J. Chang, Preparation and characterization of forsterite (Mg_2SiO_4) bioceramics, Ceramics International 33(1) (2007) 83-88. Doi:10.1016/j.ceramint.2005.07.021

[48] M.T. DeAngelis, A.J. Rondinone, M.D. Pawel, T.C. Labotka, L.M. Anovitz, Sol-gel synthesis of nanocrystalline fayalite (Fe_2SiO_4), American Mineralogist 97(4) (2012) 653-656. Doi:10.2138/am.2012.3899

[49] D. Jugović, M. Milović, V.N. Ivanovski, S. Škapin, T. Barudžija, M. Mitrić, Microsized fayalite Fe_2SiO_4 as anode material: the structure, electrochemical properties and working mechanism, Journal of Electroceramics 47(2) (2021) 31-41. Doi:10.1007/s10832-021-00260-9

[50] N. Demidov, A. Bazilevskii, R. Kuz'Min, Martian soils: Varieties, structure, composition, physical properties, drillability, and risks for landers, Solar System Research 49(4) (2015) 209-225. Doi:10.1134/S0038094615040024

[51] C. Achilles, G.W. Downs, R. Downs, R.V. Morris, E. Rampe, D. Ming, S.J. Chipera, D. Blake, D. Vaniman, T. Bristow, A. Yen, S.M. Morrison, A. Treiman, P. Craig, R. Hazen, V. Tu, N. Castle, Amorphous Phase Characterization Through X-Ray Diffraction Profile Modeling: Implications for Amorphous Phases in Gale Crater Rocks and Soils, 2018.

[52] J.R. Smyth, R.M. Hazen, The crystal structures of forsterite and hortonolite at several temperatures up to 900°C, American Mineralogist 58(7-8) (1973) 588-593.

[53] K. Hanke, Beiträge zu Kristallstrukturen vom Olivin-Typ, Beiträge zur Mineralogie und Petrographie 11(6) (1965) 535-558. Doi:10.1007/BF01110836

[54] R.M. Hazen, Effects of temperature and pressure on the crystal structure of ferromagnesian olivine, American Mineralogist 62(3-4) (1977) 286-295.

[55] Y. Kudoh, H. Takeda, Single crystal X-ray diffraction study on the bond compressibility of fayalite, Fe_2SiO_4 and rutile, TiO_2 under high pressure, Physica B+C 139-140 (1986) 333-336. Doi:10.1016/0378-4363(86)90591-7

[56] R.D. Shannon, Revised effective ionic radii and systematic studies of interatomic distances in halides and chalcogenides, Acta crystallographica section A: crystal physics, diffraction, theoretical and general crystallography 32(5) (1976) 751-767. Doi:10.1107/S0567739476001551

[57] G.W. Fisher, L.G. Medaris Jr, Cell dimensions and X-ray determinative curve for synthetic Mg-Fe olivines, American Mineralogist: Journal of Earth and Planetary Materials 54(5-6) (1969) 741-753.

[58] G.R. Lumpkin, P.H. Ribbe, Composition, order-disorder and lattice parameters of olivines; relationships in silicate, germanate, beryllate, phosphate and borate olivines, American Mineralogist 68(1-2) (1983) 164-176.

[59] N. Brese, M. O'Keeffe, Bond-valence parameters for solids, Acta Crystallographica Section B: Structural Science 47(2) (1991) 192-197. Doi:10.1107/S0108768190011041

[60] M. Morozov, C. Brinkmann, W. Lottermoser, G. Tippelt, G. Amthauer, H. Kroll, Octahedral cation partitioning in Mg, Fe^{2+}-olivine. Mössbauer spectroscopic study of synthetic $(Mg_{0.5}Fe^{2+0.5})_2SiO_4$ (Fa50), European journal of mineralogy 17(3) (2005) 495-500. Doi:10.1127/0935-1221/2005/0017-0495

[61] R. Heinemann, H. Kroll, A. Kirfel, B. Barbier, Order and anti-order in olivine I: Structural response to temperature, European journal of mineralogy 18(6) (2006) 673-689. Doi:10.1127/0935-1221/2006/0018-0673

[62] P.B. Moore, Natrophilite, NaMn(PO_4), Has Ordered Cations, American Mineralogist: Journal of Earth and Planetary Materials 57(9-10) (1972) 1333-1344.

[63] K. Iishi, Lattice Dynamics of Forsterite, American Mineralogist 63(11-12) (1978) 1198-1208.

[64] A.M. Hofmeister, Single-crystal absorption and reflection infrared spectroscopy of forsterite and fayalite, Physics and Chemistry of Minerals 14(6) (1987) 499-513. Doi:10.1007/BF00308285

[65] C. Stangarone, U. Böttger, D. Bersani, M. Tribaudino, M. Prencipe, Ab initio simulations and experimental Raman spectra of Mg_2SiO_4 forsterite to simulate Mars surface environmental conditions, Journal of Raman Spectroscopy 48(11) (2017) 1528-1535. Doi:10.1002/jrs.5127

[66] A. Chopelas, Single crystal Raman spectra of forsterite, fayalite, and monticellite, American Mineralogist 76(7-8) (1991) 1101-1109.

[67] A. Wang, B.L. Jolliff, L.A. Haskin, Raman spectroscopy as a method for mineral identification on lunar robotic exploration missions, Journal of Geophysical Research: Planets 100(E10) (1995) 21189-21199. Doi:10.1029/95JE02133

[68] A. Wang, K. Kuebler, B. Jolliff, L.A. Haskin, Mineralogy of a Martian meteorite as determined by Raman spectroscopy, Journal of Raman Spectroscopy 35(6) (2004) 504-514. Doi:10.1002/jrs.1175

[69] K.E. Kuebler, B.L. Jolliff, A. Wang, L.A. Haskin, Extracting olivine (Fo–Fa) compositions from Raman spectral peak positions, Geochimica et Cosmochimica Acta 70(24) (2006) 6201-6222. Doi:10.1016/j.gca.2006.07.035

[70] X. Yang, Q. Zhan, Investigation on the electrical and optical properties of forsterite Mg_2SiO_4 under pressure up to 30 GPa, Molecular Simulation 46(11) (2020) 805-811. Doi:10.1080/08927022.2020.1714611

[71] G. Kresse, J. Hafner, Ab initio molecular dynamics for liquid metals, Physical review B 47(1) (1993) 558. Doi:10.1103/PhysRevB.47.558

[72] G. Kresse, D. Joubert, From ultrasoft pseudopotentials to the projector augmented-wave method, Physical review b 59(3) (1999) 1758. Doi:10.1103/PhysRevB.59.1758

[73] L. Xiao, X. Li, X. Yang, Electronic and optical properties of Fe_2SiO_4 under pressure effect: ab initio study, The European Physical Journal B 91 (2018) 1-7. Doi:10.1140/epjb/e2018-80684-9

[74] M. Taran, K. Langer, Electronic absorption spectra of Fe^{2+} ions in oxygen-based rock-forming minerals at temperatures between 297 and 600 K, Physics and Chemistry of Minerals 28 (2001) 199-210. Doi:10.1007/s002690000148

Supplementary information

Mechanochemical synthesis of $(Mg_{1-x}Fe_x)_2SiO_4$ olivine phases relevant to Martian regolith: structural and spectroscopic characterizations

Md. Izzuddin Jundullah Hanafi, M. Mangir Murshed*, Lars Robben, Thorsten M. Gesing

University of Bremen, Institute of Inorganic Chemistry and Crystallography, Leobener Straße 7, D-28359 Bremen, Germany

University of Bremen, MAPEX Center for Materials and Processes, Bibliothekstraße 1, D-28359 Bremen, Germany

*Corresponding author: e-mail: murshed@uni-bremen.de, phone: +49 (0)421 218 63144

ORCID:

MIJH:	0009-0005-7842-6751
MMM:	0000-0002-9063-372X
LR:	0000-0002-0534-9573
TMG:	0000-0002-4119-2219

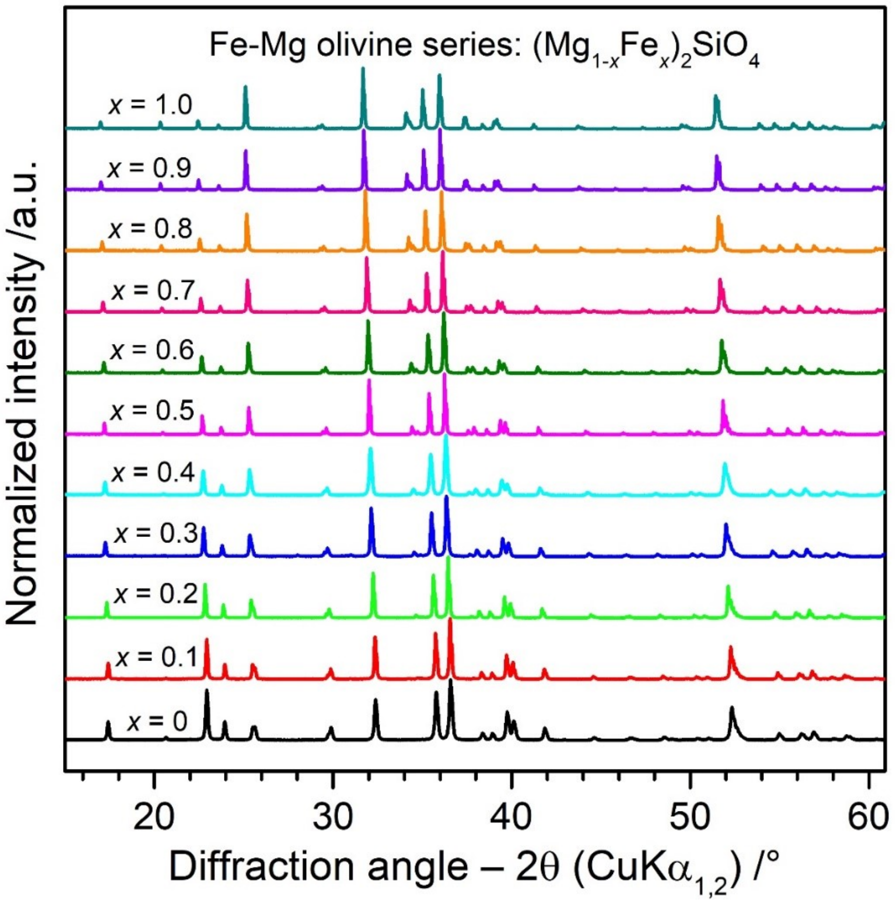

Figure S1. X-ray powder diffraction patterns of $(Mg_{1-x}Fe_x)_2SiO_4$ olivines.

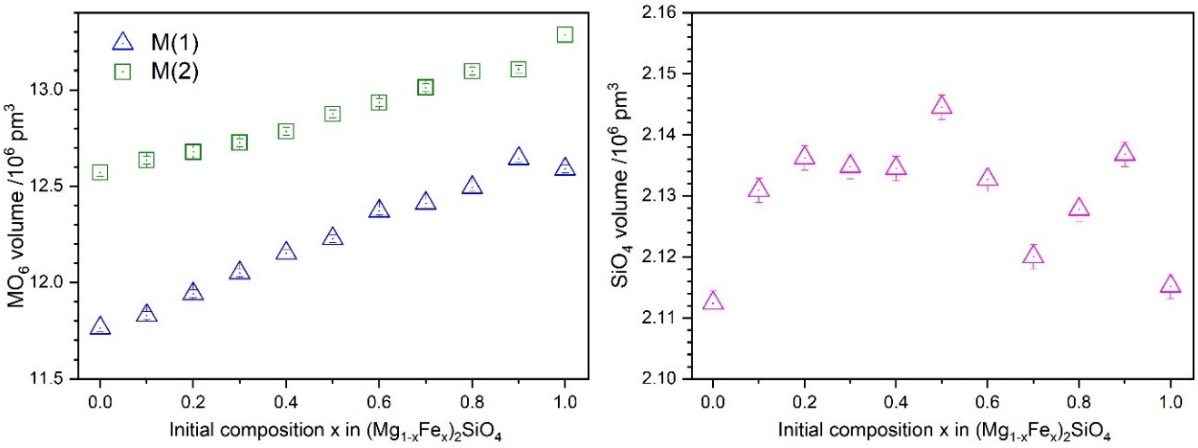

Figure S2. Evolution of polyhedral volume with respect to nominal composition *x* in $(Mg_{1-x}Fe_x)_2SiO_4$.

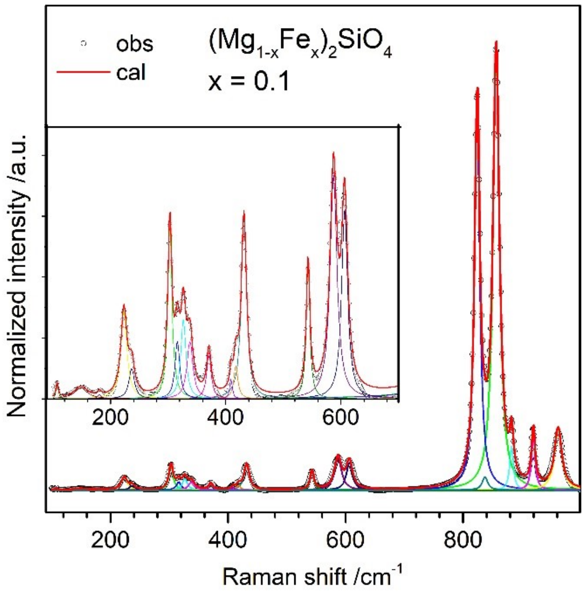

Figure S3. Representative Raman spectroscopic peak fitting of (Mg$_{1-x}$Fe$_x$)$_2$SiO$_4$ for $x = 0.1$.

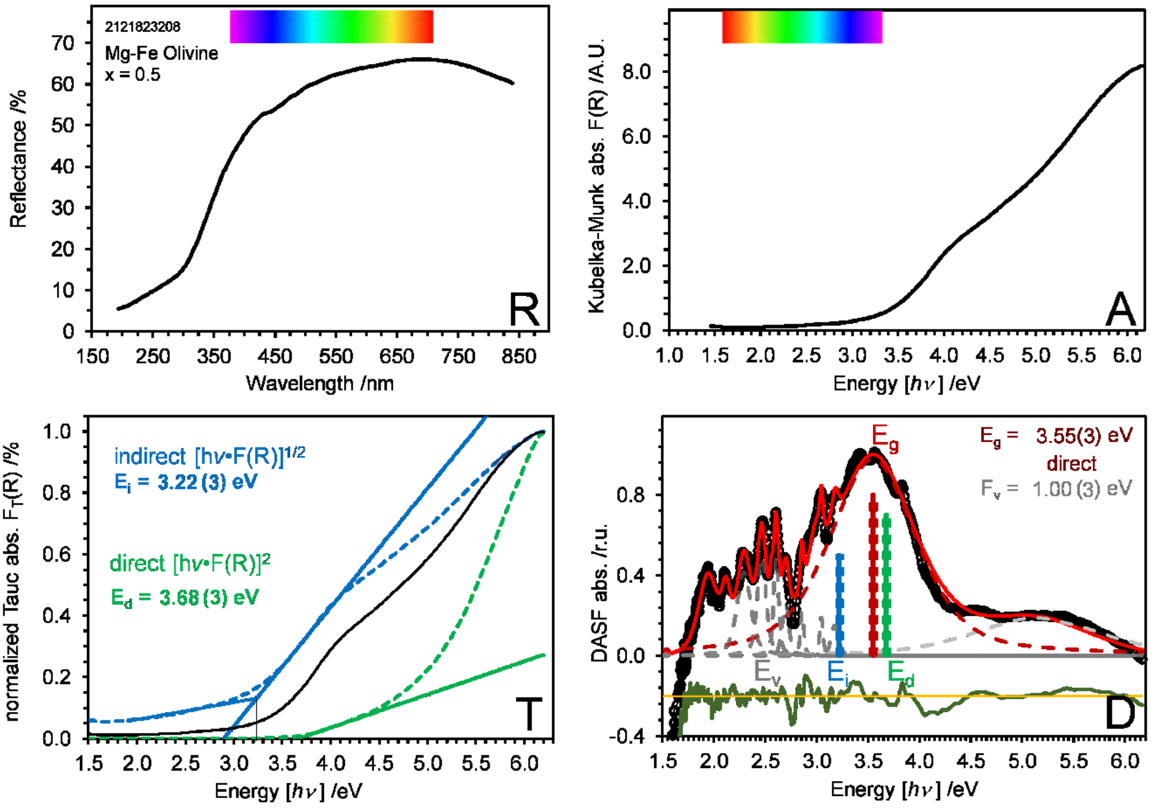

Figure S4. Representative RATD analysis of the UV/Vis diffuse reflectance data of (Mg$_{0.5}$Fe$_{0.5}$)$_2$SiO$_4$. Measured reflectance (top left), calculated Kubelka-Munk absorbance (top right), normalized Tauc plot (bottom left) and normalized DASF plot (bottom right) of (Mg$_{1-x}$Fe$_x$)$_2$SiO$_4$ for $x = 0.5$.

Table S1. Selective interatomic distances and their average values (<*M*-O>) in $(Mg_{1-x}Fe_x)_2SiO_4$ obtained from Bragg-Rietveld refinements along with the structural bond valence sum (BVS).

x	**Bond length /pm**					**BVS /v.u.**
	Si-O(1)	**Si-O(2)**	**Si-O3 (2x)**		**<Si-O>**	
0	159.5(2)	162.7(3)	161.3(1)		161.2(2)	4.13(1)
0.1	160.0(2)	163.8(3)	161.4(1)		161.7(2)	4.08(1)
0.2	160.0(3)	163.6(3)	161.7(2)		161.8(2)	4.07(1)
0.3	160.5(4)	164.0(5)	161.1(3)		161.7(4)	4.08(2)
0.4	160.5(4)	163.2(5)	161.5(3)		161.7(4)	4.08(2)
0.5	160.8(4)	162.9(5)	161.9(3)		161.9(4)	4.06(2)
0.6	159.9(4)	163.7(5)	161.3(3)		161.6(4)	4.10(2)
0.7	160.8(4)	163.0(5)	160.6(4)		161.3(4)	4.13(2)
0.8	160.5(7)	163.2(8)	161.0(6)		161.3(5)	4.11(3)
0.9	160.9(7)	163.1(9)	161.1(5)		161.6(5)	4.09(4)
1	160.0(5)	162.9(5)	160.9(4)		161.2(4)	4.14(2)
	_M_(1)-O(1) (2x)	**_M_(1)-O(2) (2x)**	**_M_(1)-O(3) (2x)**		**<_M_(1)-O>**	
0	209.6(1)	206.7(1)	213.1(1)		209.8(1)	2.01(1)
0.1	209.6(1)	207.4(1)	213.8(2)		210.3(2)	2.01(1)
0.2	210.1(2)	207.9(2)	214.9(2)		211.0(2)	2.00(1)
0.3	210.8(3)	208.7(3)	215.6(3)		211.7(3)	1.98(1)
0.4	211.2(3)	209.2(3)	217.0(3)		212.5(3)	1.96(1)
0.5	211.2(3)	209.7(3)	218.0(3)		213.0(3)	1.96(1)
0.6	212.0(3)	210.4(3)	219.4(3)		213.9(3)	1.93(1)
0.7	212.0(3)	210.9(3)	220.4(3)		214.4(3)	1.93(1)
0.8	212.3(4)	211.0(4)	221.5(4)		214.9(4)	1.93(1)
0.9	212.6(4)	212.4(4)	222.7(5)		215.9(5)	1.90(1)
1	212.7(3)	211.6(3)	223.3(3)		215.9(3)	1.92(1)
	_M_(2)-O(1)	**_M_(2)-O(2)**	**_M_(2)-O(3) (2x)**	**_M_(2)-O(3) (2x)**	**<_M_(2)-O>**	
0	218.8(2)	206.6(3)	208.2(2)	221.4(1)	214.1(2)	1.82(1)
0.1	219.5(2)	206.8(3)	208.0(2)	222.4(1)	214.5(2)	1.82(1)
0.2	219.5(3)	207.8(3)	207.8(2)	223.1(2)	214.9(2)	1.83(1)
0.3	219.3(3)	207.9(3)	208.2(3)	224.0(2)	215.3(3)	1.83(1)
0.4	219.8(4)	209.1(4)	208.0(3)	224.4(3)	215.6(3)	1.83(1)
0.5	220.9(4)	210.0(5)	207.4(3)	226.0(3)	216.3(3)	1.83(1)
0.6	221.7(4)	210.3(5)	207.9(3)	226.2(3)	216.7(3)	1.83(1)
0.7	222.1(4)	211.2(5)	208.4(3)	227.0(3)	217.4(3)	1.82(1)
0.8	223.9(6)	212.5(7)	208.2(5)	227.5(5)	218.0(5)	1.81(1)
0.9	223.5(6)	211.6(8)	207.8(5)	228.8(5)	218.1(5)	1.83(1)
1	225.4(5)	214.4(6)	208.5(4)	229.0(4)	219.1(4)	1.80(1)

Table S2. Refined site occupancy factor (SOF) and their average in $(Mg_{1-x}Fe_x)_2SiO_4$ olivines.

x	Refined SOF				Average SOF	
	4a Fe(1)	**4c Fe(2)**	**4a Mg(1)**	**4c Mg(2)**	**Fe**	**Mg**
0	0.00(1)	0.00(1)	1.00(1)	1.00(1)	0.00(1)	1.00(1)
0.1	0.07(1)	0.07(1)	0.93(1)	0.93(1)	0.07(1)	0.93(1)
0.2	0.18(1)	0.16(1)	0.82(1)	0.84(1)	0.17(1)	0.83(1)
0.3	0.29(1)	0.25(1)	0.71(1)	0.75(1)	0.27(1)	0.73(1)
0.4	0.40(1)	0.36(1)	0.60(1)	0.64(1)	0.38(1)	0.62(1)
0.5	0.49(1)	0.43(1)	0.51(1)	0.57(1)	0.46(1)	0.54(1)
0.6	0.60(1)	0.54(1)	0.40(1)	0.46(1)	0.57(1)	0.43(1)
0.7	0.70(1)	0.64(1)	0.30(1)	0.36(1)	0.67(1)	0.33(1)
0.8	0.78(1)	0.74(1)	0.22(1)	0.26(1)	0.76(1)	0.24(1)
0.9	0.90(1)	0.86(1)	0.10(1)	0.14(1)	0.88(1)	0.12(1)
1	0.97(1)	0.99(1)	0.03(1)	0.01(1)	0.98(1)	0.02(1)

Table S3. Indirect transition energy (E_i), direct transition energy (E_d) and band-gap transition energy (E_g) in $(Mg_{1-x}Fe_x)_2SiO_4$ olivines.

x	E_i /eV	E_d /eV	E_g /eV	Transition type
0	3.68(3)	4.75(3)	4.90(3)	direct
0.1	3.20(3)	4.31(3)	3.88(3)	direct
0.2	3.13(3)	3.82(3)	3.74(3)	direct
0.3	3.19(3)	3.74(3)	3.64(3)	direct
0.4	3.14(3)	3.65(3)	3.60(3)	direct
0.5	3.22(3)	3.68(3)	3.55(3)	direct
0.6	3.16(3)	3.63(3)	3.53(3)	direct
0.7	3.27(3)	3.69(3)	3.50(3)	direct
0.8	3.09(3)	3.53(3)	3.44(3)	direct
0.9	3.07(3)	3.42(3)	3.40(3)	direct
1	2.99(3)	3.46(3)	3.38(3)	direct

Chapter 4

Synthesis, structural and spectroscopic characterization of defect-rich forsterite as a representative phase of Martian regolith

Submitted in: IUCrJ (under review).

Md. Izzuddin Jundullah Hanafi[a,b], Lorenzo Bastonero[b,c], M. Mangir Murshed*[a,b], Lars Robben[a,b], Wilke Dononelli[b,c], Andrea Kirsch[d], Nicola Marzari[b,c], Thorsten M. Gesing[a,b]

[a] University of Bremen, Institute of Inorganic Chemistry and Crystallography, Leobener Straße 7, D-28359 Bremen, Germany

[b] University of Bremen, MAPEX Center for Materials and Processes, Bibliothekstraße 1, D-28359 Bremen, Germany

[c] Bremen Center for Computational Materials Science and Hybrid Materials Interfaces Group, Am Fallturm 1, D-28359 Bremen, Germany

[d] University of Copenhagen, Department of Chemistry and Nanoscience Center, Universitetsparken 5, 2100, Copenhagen, Denmark

Synopsis Ball milling of forsterite (Mg_2SiO_4) was carried out to mimic mechanical weathering processes on Mars. The defective forsterite structure models, capable of describing both long-range and short-range orders, are deduced by density functional theory assisted pair distribution function analysis.

Abstract Regolith draws intensive research attention because of its importance as the basis to fabricate materials for future human space exploration. Martian regolith is predicted to consist of defect-rich crystal structures due to long-lasting space weathering. The present report focuses on the structural differences between defect-rich and defect-poor forsterite (Mg_2SiO_4) -one of the major phases in Martian regolith. Forsterites are synthesized using reverse strike co-precipitation and high-energy ball milling (BM). The subsequent post-processing is also carried out using BM to enhance the defects. The crystal structures of the samples are characterized by X-ray powder diffraction and total scattering using Cu- and synchrotron radiation followed by Rietveld refinement and pair distribution function (PDF) analysis, respectively. The structural models are deduced by density functional theory assisted PDF refinements, describing both long-range and short-range orders caused by defects. The Raman spectral features of the synthetic forsterites complement the *ab-initio* simulation for an in-depth understanding of the associated structural defects.

Keywords: Martian forsterite; crystal structure, defects; DFT-PDF; Raman.

1. Introduction

In recent years, knowledge about Martian regolith has drastically increased due to the availability of *in-situ* X-ray diffraction data from the *Mars Science Laboratory* (MSL) on the Rover *Curiosity* (Bish *et al.*, 2013, Achilles *et al.*, 2017, Vaniman *et al.*, 2014). The analysis of this diffraction data estimated (Certini *et al.*, 2020, Achilles *et al.*, 2017, Vaniman *et al.*, 2014, Demidov *et al.*, 2015, Bish *et al.*, 2013) approximately 28 wt-% to 45 wt-% amorphous fraction in the Martian regolith. A notable amorphous phase content in Martian regolith indicates significant space-weathering due to extreme environmental conditions (Certini *et al.*, 2020). Space-weathering is the alteration of exposed surfaces via their interaction with the space environment (Bennet *et al.*, 2013). It is a combination of mechanical-weathering caused for example by meteorite impacts as well as radiation-weathering from high-energy solar wind radiation. The former process can be simulated by ball milling of terrestrial materials in the laboratory (Yu *et al.*, 2022).

Olivine-type forsterite (Mg_2SiO_4) is one of the major phases found in the crystalline part of Martian regolith (Bish *et al.*, 2013, Achilles *et al.*, 2017). Bish et al. (Bish *et al.*, 2013) reported that approximately 22.4 wt-% of $(Mg_{0.62}Fe_{0.38})_2SiO_4$ (which is called a forsteritic olivine in the forsterite-fayalite (Fe_2SiO_4) solid solution due to the higher Mg content compared to Fe) was found in Martian soil from the *Rocknest Aeolian* bedform in *Gale* crater. Similarly, Achilles et al. (Achilles *et al.*, 2017) found approximately 25.8 wt-% of forsteritic olivine ($(Mg_{0.56}Fe_{0.44})_2SiO_4$) in Martian soil of *Namib* dune called *Gobabeb*. For future use of regolith as a basis to fabricate metals or building materials for human space explorations, a precise analysis of the different defects present in forsterites is of crucial importance. The defect-rich forsterite is expected to have lower formation energy, hence may be desirable for more efficient processing of fabrication in space.

Forsterite belongs to planetary and terrestrial rock-forming minerals (Liu *et al.*, 2022, Váci *et al.*, 2020) and is known for its capability of catalyzing reactions in interstellar durst (Campisi *et* *al.*, 2024). Forsterite is the magnesium endmember of the olivine solid solution $(Mg_{1-x}Fe_x)_2SiO_4$ (Jundullah Hanafi *et al.*, 2024, Rösler, (1991)) and crystallizes in the orthorhombic space group *Pbnm* (Fujino *et al.*, 1981, Müller-Sommer *et al.*, 1997, Lager *et al.*, 1981). The structure, displayed in **Figure 1**, consists of one-dimensional octahedral chains running parallel to the crystallographic ***c***-axis, comparable to those found in the mullite-type phase (Angel & Prewitt, 1986, Bowen *et al.*, 1924, Cong *et al.*, 2010, Fischer *et al.*, (2009), Gogolin *et al.*, 2020). In the mullite-type phase, these octahedral chains are bridged by double-tetrahedra or other double units in the ***ab***-direction (Murshed *et al.*, 2012, Schneider *et al.*, 2012), whereas in olivine, single $(SiO_4)^{4-}$ tetrahedra link the octahedral chains in the ***a***-direction, where the tetrahedral oxygen atoms are shared by three octahedral cations (Zampiva *et al.*, 2017). The respective link in the ***b***-direction is realized by two non-equivalent Mg octahedral sites: the first site (*M*1, chain octahedra) has inversion symmetry, while the other site (*M*2, linking octahedra) possesses mirror symmetry (Yang *et al.*, 2006). Both sites can be occupied by various cations, forming either rich solid solutions or other endmembers such as fayalite (Fe_2SiO_4) (Hanke, 1965, Kudoh & Takeda, 1986, Hazen, 1977), tephroite (Mn_2SiO_4) (Fujino *et al.*, 1981), larnite (Ca_2SiO_4) (Czaya, 1971), liebenbergite (Ni_2SiO_4) (Della Giusta *et al.*, 1990, Lager *et al.*, 1981), and cobalt olivine (Co_2SiO_4) (Morimoto *et al.*, 1974, Müller-Sommer *et al.*, 1997), which enable a wider spectrum of elements extractable from a regolith matrix.

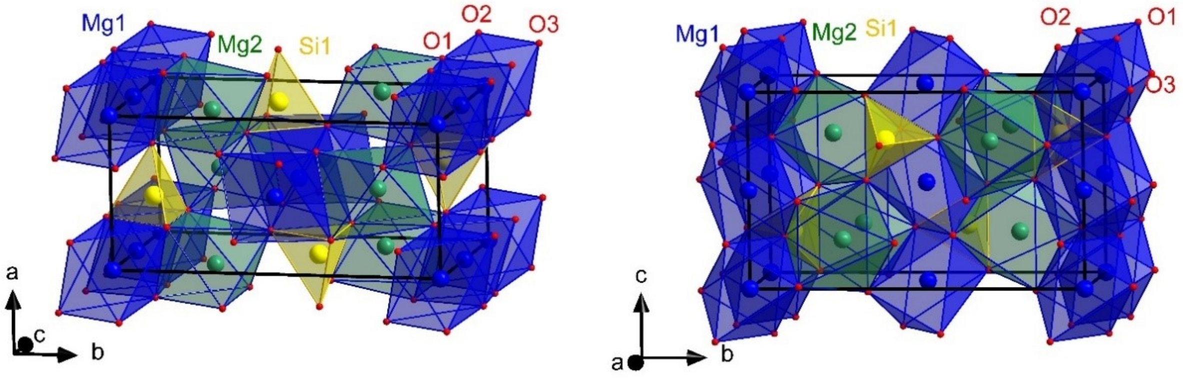

Figure 1 Crystal structure of Mg_2SiO_4 (forsterite).

Forsterite can be synthesized through a variety of synthesis methods including solution combustion technique (Naik *et al.*, 2015, Mondal *et al.*, 2016, Prashantha *et al.*, 2011), sol-gel method (Ni *et al.*, 2007), mechanical activation followed by heat treatment (Fathi & Kharaziha, 2008, Tavangarian & Emadi, 2010, Fathi & Kharaziha, 2009), and reverse strike co-precipitation (RSC) (Zampiva *et al.*, 2017). Despite many studies on the synthesis yielding pure forsterite, to the best of our knowledge, there are no reports on mechanically induced defective-rich forsterites and their associated crystal structures. Defects are commonly defined as a considerable extent of irregularities in the crystal structure (Wagner, 1977), for instance vacancies or dislocated atoms as illustrated in **Figure S1** (Supplementary Information). In an X-ray diffraction pattern, typical strain broadening and lower absolute intensities are expected for defect-rich crystallites (Ungár, 2004, Chauhan & Chauhan, 2014) often accompanied by reflection broadening due to crystallite size effects (Scherrer, 1918, Gesing & Robben, 2024). Similarly, broadening of Raman peaks is a hint to disordered structures in defect-rich materials (Demtröder, 2008, Gouadec & Colomban, 2007). In addition to Rietveld analysis of reciprocal-space X-ray powder diffraction (XRPD) data, real-space investigations of defects and local structures are widely performed by pair distribution function (PDF) analysis (Bini *et al.*, 2012, Malavasi *et al.*, 2011, Proffen *et al.*, 2003).

The present work focuses on the synthesis and characterization of forsterite and its mechanical post treatment to induce various defect concentrations. The derived defect-structure model can serve as a structural representative for the analysis of Martian regolith. To achieve this objective, Mg_2SiO_4 samples were first synthesized by two different routes: RSC method and mechanical activation using high-energy ball milling (BM) with subsequent calcination. In a second step, mechanical post treatment was performed to obtain defect-rich forsterite. We present a detailed comparison of structural features between the samples by using Raman, XRPD and X-ray total scattering techniques. In addition, density functional theory (DFT) is used to optimize defect-rich structures and compare their thermodynamic stability. Finally, the DFT supported PDF analysis (DFT-PDF) is used to refine the defective structural models.

2. Materials and methods

2.1. Synthesis of defect-poor forsterite

2.1.1. Reverse strike co-precipitation (RSC) synthesis

Magnesium nitrate hexahydrate ($Mg(NO_3)_2{\cdot}6H_2O$) 99.9 % and tetraethyl orthosilicate (TEOS) 98 % were purchased from VWR Chemicals and used as received. Similar to a typical RSC synthesis (Zampiva *et al.*, 2017), stoichiometric amounts of $Mg(NO_3)_2{\cdot}6H_2O$ and TEOS were dissolved in a solution of 40 ml of ethanol and 3 ml of HNO_3 (≥ 65 %) under magnetic stirring for 1 h. The precursor solution was slowly dripped into 50 ml of 25 % NH_4OH under continuous stirring. The base solution formed a colloid while the precursor solution was being dripped, until the last drop forming a white precipitate. Simultaneously, several drops of concentrated NH_4OH were added to keep the pH > 8. Thereafter, the precipitate was centrifuged at 60 Hz for 5 min. The supernatant was removed, and ethanol was used to wash the precipitated powder. The centrifugation was repeated three times. Finally, the precipitated solid was placed in a furnace at 473 K for 16 h. The resulting solid was ground in a mortar and calcined at 1373 K for 1 h after reaching the temperature with a heating and cooling rate of 15 K/min and 5 K/min, respectively. The attained powder is further designated as RFO (RSC synthesis forsterite).

2.1.2. Ball milling (BM) synthesis

As starting materials MgO and amorphous SiO_2 powders were used. Magnesium oxide (MgO) > 97 % was purchased from Merck and used as received. Amorphous SiO_2 was obtained from hydrolysis of TEOS (De *et al.*, 2000). Forsterite was synthesized by mechanical activation with a high-energy ball mill (Emax-type, RETSCH GmbH). Stoichiometric amounts of the binary oxides were mixed and placed, together with 60 g tungsten carbide (WC) balls (2 mm diameter), in a WC grinding jar. The ball-to-powder weight ratio was set to 30:1. The powder was milled for 3 h with different rotational frequencies (7 Hz, 12.5 Hz, 15 Hz). Finally, the milled powder was collected from the grinding jar and heated in a corundum crucible at 1373 K with a heating rate of 15 K/min. After a reaction period of 1 h, the powder was cooled down to room temperature with a cooling rate of 5 K/min. The attained powder of Mg_2SiO_4 (PFO) was ground and further used for characterization.

2.2. Synthesis of defect-rich and healed forsterite

Defect-rich forsterite was prepared by crushing a pure as-synthesized forsterite (PFO) by ball milling. The pure forsterite (1 g) was placed into the grinding jar with 20 g WC balls. The powder was milled at 15 Hz for 1 h. Thereafter, one half of the milled powder was kept separately and labeled as crushed forsterite (CFO). The other half was calcined at 1373 K for 1 h under air to heal the introduced defects, hence labeled as healed forsterite (HFO).

2.3. X-ray powder diffraction

X-ray powder diffraction (XRPD) data collection was carried out on a Bruker D8 Discover diffractometer using $CuK_{\alpha1,2}$ radiations ($\lambda_{K\alpha1}$ = 154.05929(5) pm, $\lambda_{K\alpha2}$ = 154.4414(2) pm) in Bragg–Brentano geometry. Data were collected under ambient condition from 5° to 85° 2θ with a step width of 0.0149° 2θ and a measurement time of 0.3 s per step using a multi-strip LynxEye XE-T detector. XRPD data Rietveld refinements were carried out using TOPAS V6.0 (Bruker AXS, Germany). During the Rietveld refinements, the background, sample displacement, metric, atomic positional and profile parameters were optimized. The amorphous fraction of the samples was quantified from the degree of crystallinity (DC) as implemented in the TOPAS software. For these calculations it is assumed that the average scattering power of the crystalline fraction of the sample is identical to the scattering power of the X-ray amorphous fraction. The latter one could either consist of glassy or quantum-crystalline contributions (Gesing *et al.*, 2022). Using the fundamental parameter approach (Cline *et al.*, 2010), the apparent average crystallite size (ACS) was calculated from all observed X-ray reflections, which is described as $L_{Vol}(IB)$ by the TOPAS suite. $L_{Vol}(IB)$ refers to the volume-weighted mean of the coherently diffracting domain size using the integral breadth for the description of the reflection profile. The respective pseudo-Voigt profile function was deconvoluted into Gaussian and Lorentzian components, describing the ACS and the micro-strain (ε_0), respectively. To validate these data and to receive information about the crystallite size distribution an EnvACS analysis (Gesing & Robben, 2024) was performed. For this, data were collected on a Bruker D8 Advance diffractometer using CuK$_{\alpha1}$ radiations ($\lambda_{K\alpha1}$ = 154.05929(5) pm) in Bragg–Brentano geometry. Data were collected under ambient condition from 10° to 135° 2θ with a step width of 0.01449° 2θ and a measurement time of 4.8 s per step using a multi-strip LynxEye XE detector. The information deduced during these (classical) Rietveld refinements are, except the DC, based on the appearance of the Bragg reflections and an ideal arrangement of atoms in the unit-cell only (Rietveld, 1969). To distinguish these calculations from those using total scattering data, we use for the classical method the expression Bragg-Rietveld. The given R_{wp} is the weighted profile R-factor (residual) of the Bragg-Rietveld refinement. To distinguish R_{wp} of Bragg-Rietveld and R_{wp} of PDF refinements the latter one is given as R_{PDF}.

2.4. Raman spectroscopy

Raman spectra were recorded on a LabRam ARAMIS (Horiba Jobin – Yvon) Micro-Raman spectrometer equipped with a green laser (λ_{ex} = 532 nm and < 20 mW power). A 50x objective (Olympus) with a numerical aperture of 0.75 provides a focus spot of 865 nm diameter when closing the confocal hole to 200 µm. Each spectrum ranges between 100 cm^{-1} and 1200 cm^{-1} with a spectral resolution of approximately 1.2 cm^{-1} using a grating of 1800 grooves/mm and a thermoelectrically cooled CCD detector (Synapse, 1024 x 256 pixels).

2.5. Theoretical Raman calculations

The theoretical Raman spectra calculations were carried out using the aiida-vibroscopy package (Bastonero & Marzari, 2024), which exploits the finite displacements and finite field approach (Souza *et al.*, 2002, Umari & Pasquarello, 2002), and the AiiDA infrastructure (Huber *et al.*, 2020, Uhrin *et al.*, 2021) to automate the submission of the simulations, and the storage of all the data in a reproducible format. The first-order spectrum was calculated in the nonresonant regime using the Placzek approximation. The peak positions associated to the phonon modes were computed in the harmonic approximation via small displacements of the atomic positions (Togo, 2023, Togo *et al.*, 2023) while the Raman tensors, needed for the intensities calculations, were obtained via numerical differentiation of the forces upon the application of small electric fields (Bastonero & Marzari, 2024). Computational details can be found in section 2.8.

2.6. X-ray synchrotron total scattering

Total scattering data were collected using beamline P02.1@PETRA-III, DESY, Hamburg (Dippel *et al.*, 2015) with a fixed energy of 60 keV (λ = 20.734(2) pm). The beamline was equipped with a Varex XRD 4343CT detector (pixel size 150 µm x 150 µm, 2880 x 2880 pixels). Each sample was measured in 1 mm Kapton capillaries and exposed to the radiation for 300 s within a set-up particularly optimized for rapid *in-situ* measurement. PDF data processing was conducted using the PDFGetX3 software (Juhás *et al.*, 2013). For all samples, Q_{max} was set to 1.95 nm^{-1}. Structure model fitting against PDF data was performed using PDFgui (Farrow *et al.*, 2007). During the refinement process, instrumental parameters Q_{damp} and Q_{broad} were refined to the CeO_2 standard data set, and then kept fixed with Q_{damp} = 0.035693 and Q_{broad} = 0.001 for all the samples. The scale factor, lattice parameters, atomic displacement parameters (ADP), atomic motion correlation factor, and atomic coordinates were refined. Representative processed data *I(Q)*, *S(Q)*, *F(Q)*, and *G(r)* of pure forsterite are shown in **Figure S2** in the supplementary information. Stack plots of *I(Q)* and *S(Q)* of all samples are given in **Figure S3**.

2.7. DFT-PDF refinement

Combined DFT-PDF refinements of defective forsterite in the spirit of ref. (Dononelli, 2023, Kløve *et al.*, 2023) were performed. Instead of globally optimizing the structure with GOFEE algorithm (Bisbo & Hammer, 2020, 2022, Kløve *et al.*, 2023), several types of defects, namely vacancies, Frenkel-, and Schottky-defects were introduced to each atom site during the simulations. DFT was used as a tool to optimize every defect-type structure to their local minimum in the potential energy surface (PES). The geometry-optimized structures were further optimized with a BFGS algorithm by considering *G(r)* data from measurements and minimizing the R_{PDF}. Finally, the structures were refined against experimental data using PDFgui. The schematic workflow of DFT-PDF refinements is illustrated in **Figure 2**.

Local structure optimizations have been performed using the electronic structure code GPAW (Enkovaara *et al.*, 2010) in the framework of the atomistic simulation environment (ASE) (Larsen *et al.*, 2017). The exchange-correlation interaction was treated by the generalized gradient approximation (GGA) using the Perdew–Burke–Ernzerhof (PBE) functional (Perdew *et al.*, 1996) with a 3×5×3 *k*-points sampling of Monkhorst and Pack (Monkhorst & Pack, 1976). Note, that these calculations were not meant to give very precise energetics or exact bond lengths. All structures optimized with such settings are later post processed in PDF-Rietveld refinements to fit to experimentally observed bond lengths.

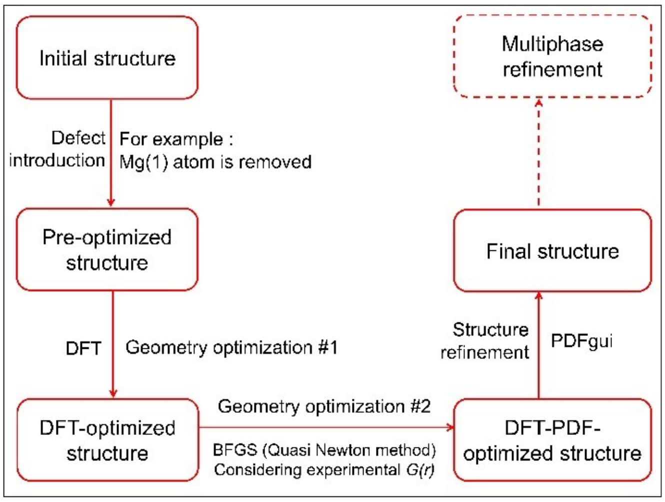

Figure 2 Schematic workflow maintained during the DFT-PDF refinement for different forsterite structures.

2.8. Energy calculations

To verify the favorite defective intrinsic candidate, the *ab-initio* formation energy was investigated using DFT calculations. Exploiting the supercell approach, the defect formation energy in a charge state q can be computed as: (Zhang & Northrup, 1991, Van de Walle *et al.*, 1993, Alkauskas *et al.*, (2011), Freysoldt *et al.*, 2014)

$$E^f[X;q] = E[X,q] - E[bulk] - \sum_i n_i\mu_i + q(\varepsilon_v + \varepsilon_F).$$

$E[X,q]$ indicates the total energy of the supercell calculation of defect X in the charge state q, and $E[bulk]$ is the total energy of the pristine crystal structure scaled to match the size of the defective supercell. Each defect is referenced to a chemical potential μ_i corresponding to its species i, while the integer n_i indicates the atoms of type i in excess ($n_i > 0$) or removed ($n_i < 0$). For charged states, the chemical potential for the extra electrons is given by the Fermi energy ε_F. referred to the valence band maximum ε_v of the pristine bulk supercell (Komsa *et al.*, 2012). The Fermi energy can be found by the condition of charge neutrality at a specific temperature when all the relevant defects are considered. In the following we consider $\varepsilon_F = 0$. To understand the defect formation in the diluted limit (very low defect concentrations) an additional correction term needs to be added due to the periodic boundary conditions, which is described in more detail in the SI.

Different defect types along with their nominal and neutral charge states, as well as both relaxed and non-relaxed geometry of the supercells were thoroughly investigated. Four different supercell sizes, 2x1x2, 3x1x2, 3x2x2, and 3x3x2 were selected, as well as the single unit cell. For the interstitials, an algorithm introduced by Zimmermann et al. (Zimmermann *et al.*, 2017) was used to find suitable atomic positions; 11 different positions are found for each species as possible candidates. Interestingly, the interstitials proposed by this pure geometric analysis for the magnesium atoms are found to be in tetrahedral coordination, as found in (Walker *et al.*, 2009), but here without the explicit energy calculation. The vacancies were instead generated using the space group symmetries of forsterite, which greatly limits the number of positions.

To carry out the calculations, the Quantum ESPRESSO package (Giannozzi *et al.*, 2009, Giannozzi *et al.*, 2017, Giannozzi *et al.*, 2020) was used and the PBEsol (Terentjev *et al.*, 2018) functional was employed using pseudo-potentials from the precision SSSP library (version 1.1) (Prandini *et al.*, 2018). The wave-function and charge-density expansions were truncated with an energy cutoff of 80 Ry and 960 Ry, respectively. The Brillouin zone was sampled using a uniform Monkhorst-Pack grid using a 4x2x3 *k*-points mesh. The geometry and atomic positions of forsterite were therefore relaxed till the total energy and forces are below 10^{-6} Ry/atom and 10^{-5} Ry/Bohr, respectively. Supercell calculations were carried out using a gamma-point sampling, after having verified for a 2x1x2 supercell that the total energy changed by only 2 meV/atom. The geometry and the atomic positions of each defective supercell were optimized with lower thresholds for total energy and forces, respectively 10^{-4} Ry/atom and 10^{-3} Ry/Bohr.

3. Results and discussion

3.1. Synthesis

Impure forsterite was obtained from BM synthesis with 7 Hz (IFO-7) and 12.5 Hz (IFO-12). On the other hand, pure forsterite was successfully obtained by RSC synthesis (Zampiva *et al.*, 2017) (RFO) and BM synthesis at 15 Hz (PFO). Both synthesis techniques yielded white forsterite powder. To introduce defects into the material, the attained PFO powder was mechanically post-processed by BM at 15 Hz for 1 h resulting in crushed forsterite (CFO). CFO possesses a slightly greyish color, due to trace amounts of WC abraded from the mill and might hint the presence of defects. However, we estimated the amount to be lower than the detection limit (0.5(1) wt-%) as we cannot observe any WC signal in the XRD (nor Raman) data. Finally, a small amount of CFO was re-calcined at 1373 K obtaining white powder of healed forsterite (HFO) with expected lower defect concentrations. The synthesized samples and their respective ID are listed in **Table 1.** The detail information about phase quantification for impure forsterites determined from Rietveld refinements are given in the **section 3.2**.

Table 1 List of synthesized samples and their abbreviations

Sample ID	Material
RFO	RSC synthesis forsterite
IFO-7	Impure forsterite from 7 Hz BM
IFO-12	Impure forsterite from 12.5 Hz BM
PFO	Pure forsterite from 15 Hz BM
CFO	Crushed forsterite (post-processed PFO)
HFO	Healed forsterite (re-calcined CFO)

3.2. X-ray powder diffraction

XRPD data Bragg-Rietveld refinements confirm that IFO-7 contains impurities of MgO, $MgSiO_3$, and SiO_2 in two modifications (α-cristobalite and α-quartz), while IFO-12 possesses only MgO as minor impurity. This indicates that the ball milling frequencies of 7 Hz and 12.5 Hz are not sufficient to form an intimate mixture of the reactants before the calcination process. On the contrary, pure forsterite was obtained from RSC synthesis (RFO) and BM synthesis at 15 Hz (PFO). All reflections in the diffraction pattern of both samples can be indexed to olivine-type Mg_2SiO_4 with space group *Pbnm* (Müller-Sommer *et al.*, 1997). The mechanically treated sample (CFO) is also characterized as a pure forsterite. However, broadening of the Bragg reflections along with significantly lower intensity maxima is observed, as seen in **Figure 3**. Moreover, CFO exhibits notable lower average crystallite size (ACS) (25(1) nm) and DC (60(5) %), compared to those of PFO (ACS = 77(1) nm and DC = 98(5) %). Inversely, the micro-strain is increased from 0.031(1) to 0.140(4) upon ball milling. The re-calcination process of CFO led to re-crystallization, forming a crystalline forsterite with ACS, ε_0 and DC of 77(2) nm, 0.140(4) and 90(5) %, respectively, like those of PFO. Comparable values are observed when analyzing the ACS using the EnvACS (Gesing & Robben, 2024) approach. Nevertheless, the crystallite size distribution gives additional information on the defect formation and the respective defect healing. Whereas for the synthesized samples (RFO and PFO) the crystallite size distribution (CSD) is narrow, a much broader CSD is observed for CFO. This is not surprising, as it is assumed that not only defects are introduced but during the reduction of the ACS due to crystallite cracking not all crystallites are homogeneously destroyed. For the heated CFO portion resulting in the HFO sample it is obvious that the distribution narrows again by a factor of two but did not reach the narrow distribution of the as synthesized PFO. Interestingly, meaningful results could only be obtained by refining also a scale factor in the EnvACS (Gesing & Robben, 2024) approach, which would represent the distribution of two different phases, namely the crystalline forsterite and the amorphous forsterite respectively. The obtained scale factors correlate quite well with the DC obtained by the Bragg-Rietveld refinements. A complete list of XRPD characterization results is given in **Table 2**. The stack plots of X-ray powder diffraction patterns of all samples can be seen in **Figure S4**.

Table 2 Average crystallite size (ACS) and micro-strain (ε_0) of forsterites, and the degree of crystallinity (DC) of the synthesized samples obtained from Bragg-Rietveld refinements of XRPD data. Additionally, the ACS and the crystallite size distribution factor (CSD), correlating the smallest (0.01) and broadest (1) distribution of spherical crystallites, are given. Both values were refined with a fixed to 1 and a variable scale factor, considering perfect and reduced DC, respectively.

Sample ID	Bragg-Rietveld					EnvACS		
	Phase fraction /%		ACS /nm	ε_0	DC /%	ACS /nm	CSD factor	scale factor
IFO-7	Mg_2SiO_4	62(2)	58(1)	0.048(2)	95(5)	-	-	-
	MgO	23(2)	-	-	-	-	-	-
	$MgSiO_3$	8(2)	-	-	-	-	-	-
	SiO_2 α-cristobalite	6(2)	-	-	-	-	-	-
	SiO_2 α-quartz	1(2)	-	-	-	-	-	-
IFO-12	Mg_2SiO_4	98(2)	61(1)	0.053(5)	93(5)	-	-	-
	MgO	2(2)	-	-	-	-	-	-
RFO	Mg_2SiO_4	100(2)	89(1)	0.027(1)	95(5)	85.5(5)	0.01(1)	1
						87.1(5)	0.01(1)	0.98(1)
PFO	Mg_2SiO_4	100(2)	77(1)	0.031(1)	98(5)	88.3(5)	0.01(1)	1
						89.0(5)	0.01(1)	0.99(1)
CFO	Mg_2SiO_4	100(2)	25(1)	0.140(4)	60(5)	33.3(2)	0.01(1)	1
						57.6(3)	0.17(1)	0.68(1)
HFO	Mg_2SiO_4	100(2)	77(2)	0.046(1)	90(5)	74.9(6)	0.01(1)	1
						75.4(4)	0.07(1)	0.95(1)

Refined forsterite crystal data, along with comparative literature (Smyth & Hazen, 1973), are presented in **Table S1**. The respective Bragg-Rietveld refinements converged with lower R_{wp} values for RFO (11 %) and PFO (11 %) compared to CFO (15 %) and HFO (15 %) (see **Figure 3** and **Table S1**). Moreover, structure refinements indicate that RFO and PFO can be classified as defect-poor forsterites, as their refined atomic positions possess only small changes ($\Delta z \leq 0.003$) compared to pristine forsterite. In contrast, noticeable structural changes are observed in both HFO and CFO. As an example, the O(3) in HFO slightly deviates from its initial position ($\Delta z \leq 0.010$) while CFO shows even stronger changes ($\Delta z \leq 0.018$). The strength of these observed structural changes is proportional to the expected defect concentration in the crystal, which is described in more detail in **section 3.3.**

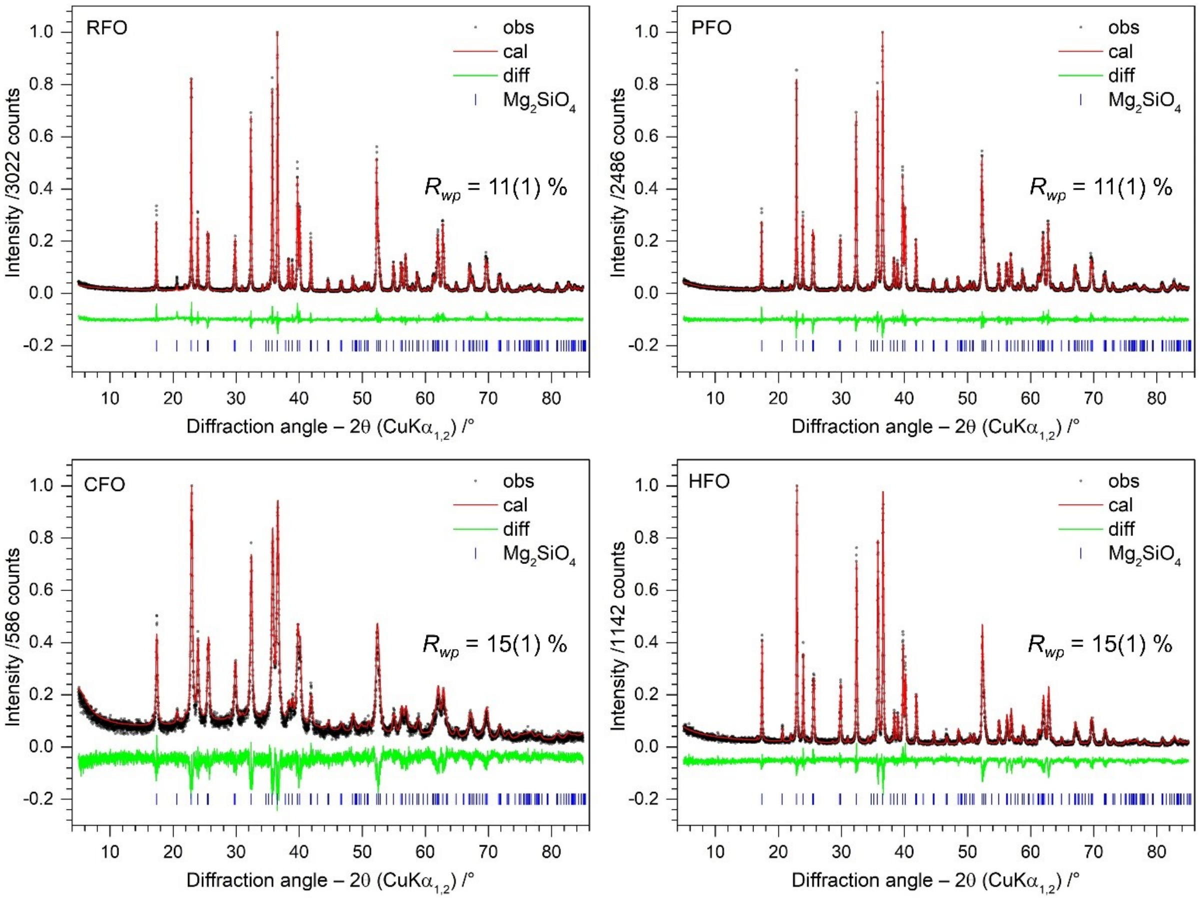

Figure 3 X-ray powder diffraction data Rietveld plots of different forsterites.

3.3. Raman spectroscopy

The factor group analysis predicts that orthorhombic Mg_2SiO_4 has 84 normal vibrational modes (11 A_g + 11 B_{1g} + 7 B_{2g} + 7 B_{3g} + 10 A_u + 10 B_{1u} + 14 B_{2u} + 14 B_{3u}), among which A_g, B_{1g}, B_{2g}, and B_{3g} modes are Raman-active (Iishi, 1978, Hofmeister, 1987). Raman spectra of different forsterites are shown in **Figure 4**. Peak fitting was performed for each experimental spectrum, representatively shown in **Figure S5** for PFO. The peak maxima along with comparative experimental reference data (Kolesov & Geiger, 2004) and theoretical calculations (Stangarone *et al.*, 2017, McKeown *et al.*, 2010) are given in **Table S2**. The observed band frequencies are in good agreement with those of the reported ones (Kolesov & Geiger, 2004, Stangarone *et al.*, 2017, McKeown *et al.*, 2010) and our own theoretical calculation. Typically, Raman spectra of olivine-type Mg_2SiO_4 can be classified into three regions: <400 cm^{-1}, 400 cm^{-1} - 700 cm^{-1} and >700 cm^{-1}. The lower region bands are attributed to the vibrational modes from Mg (M(2)-site) and negligible contribution from lighter silicon (Stangarone *et al.*, 2017, Chopelas, 1991). Peaks between 400 cm^{-1} and 700 cm^{-1} are mainly contributed from bending motion of the Mg(2) with oxygen (Stangarone *et al.*, 2017). The high-frequency region (> 700 cm^{-1}) can be attributed to the internal Si-O stretching vibrations of the SiO_4 tetrahedra (Chopelas, 1991, Stangarone *et al.*, 2017). The most dominant characteristic forsterite spectral range lies at around 820 cm^{-1} and 860 cm^{-1} (Chopelas, 1991, Iishi, 1978, Wang *et al.*, 1995, Wang *et al.*, 2004).

Some vibrational features from optical phonons are clearly distinguishable between the defect-poor samples (RFO and PFO) and the defect contained samples (CFO and HFO). Global red-shifts of ±1 cm^{-1} along with peak broadening (ΔFWHM $\leq$ 2 cm^{-1}) are observed in HFO. Moreover, greater red-shifts of approximately 3(1) cm^{-1} as well as peak broadening (ΔFWHM $\leq$ 4 cm^{-1}) are observed in CFO. The dominant two intense modes related to Si-O are further shifted to 825(1) cm^{-1} and 857(1) cm^{-1}, with FWHM of 11(1) cm^{-1} and 13(1) cm^{-1}, respectively. In general, peak shifting and broadening in Raman can be attributed to crystallite size effects and the degree of disorder in a structure (Swamy *et al.*, 2006, Islam *et al.*, 2005, Gouadec &

Colomban, 2007, Demtröder, 2008). Here, the Raman peak broadening and shifts are proportional to the defect concentration in the structure. This finding further indicates that the CFO sample exhibits local structural disorder with the highest concentration.

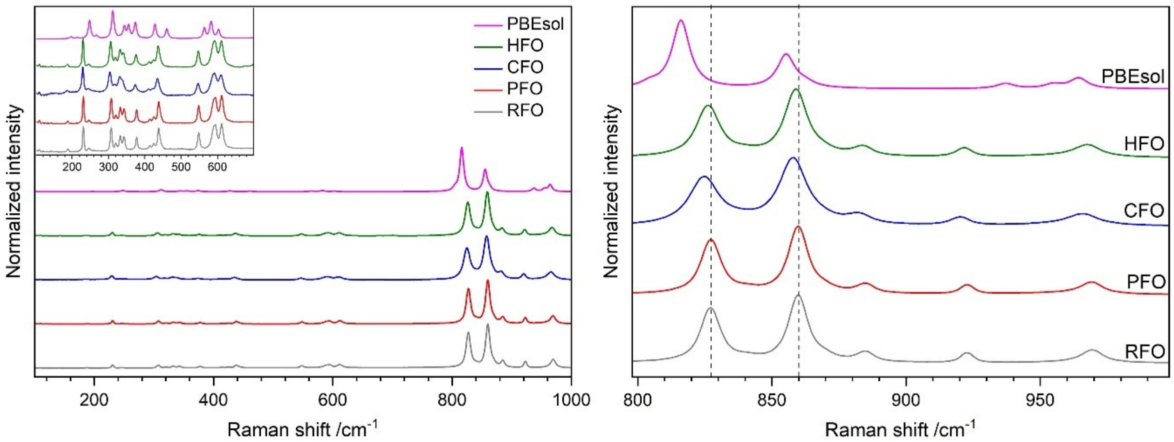

Figure 4 Raman spectra of different forsterites collected at ambient condition and PBEsol calculation (left). Magnified view of the high-frequency region (right), where the vertical dashed lines are guide for the eyes.

3.4. PDF analysis

To further investigate the defects and local structures of the samples, total scattering experiments were carried out (beamline P02.1@PETRA-III, DESY, Hamburg). The analysis of the total scattering data allows extracting information from both Bragg and diffuse scattering contributions. Bragg scattering contribution can be analyzed by conventional approach in reciprocal space and provides information on the average and long-range periodic structure, whereas the diffuse scattering which lies between and beneath the Bragg reflections (Egami & Billinge, (2003)) yields information regarding the short-range order and local structure deviations. Each measurement was integrated, background corrected, and Fourier transformed to obtain the reduced pair distribution function *G(r)*. The *G(r)* describes the probability of finding two atoms separated by a distance of *r* (Teck *et al.*, 2017). While the observed PDFs (*G*(*r*)) of RFO, PFO, and HFO are very similar, the one of CFO shows significant discrepancies, e.g. broadened signals, clear shoulders and lower intensities, as seen in **Figure 5**.

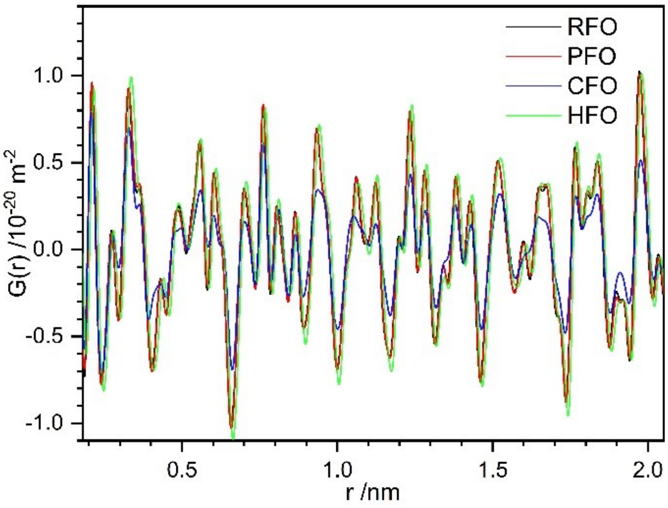

Figure 5 Observed *G(r)* for different forsterites.

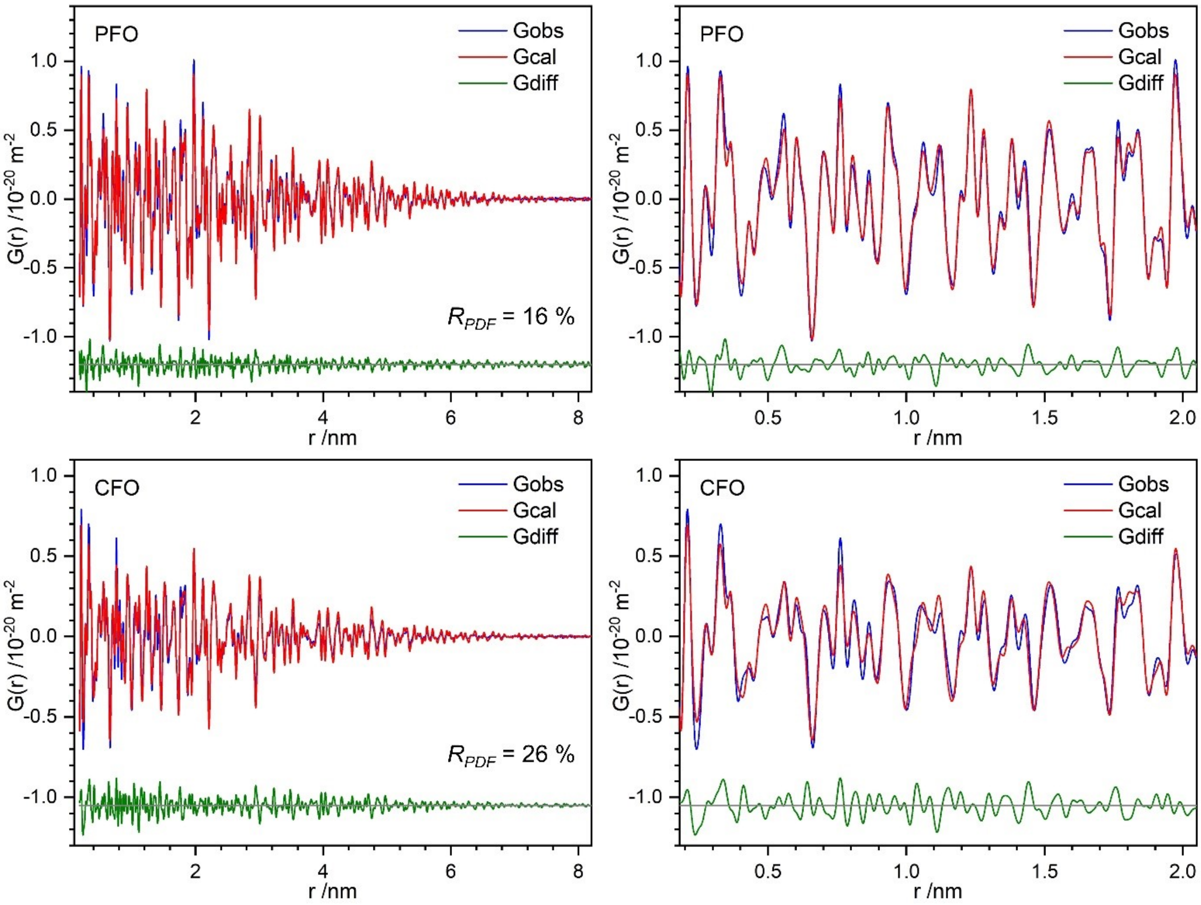

Figure 6 Representative PDF-Rietveld refinement plots of PFO and CFO in the long (left) and short to medium (right) range.

Defect-free, symmetry-constrained structural models of Mg_2SiO_4 were fitted against the experimental PDFs using a small box modelling approach including symmetry constrains (PDF-Rietveld). Representative PDF-Rietveld refinements of the investigated forsterites are shown in **Figure 6**. The refinements of CFO converged with R_{PDF} = 26 %, significantly higher compared to those of RFO, PFO (R_{PDF} = 16 %) and HFO (R_{PDF} = 18 %). The higher R_{PDF} of CFO indicates that a simple PDF-Rietveld refinement using an ideal average crystal structure model struggles in describing the defect-rich local nature of the post-milled sample. As such, a more advanced defect-rich structure model based on DFT-PDF refinements is proposed in this work, which is described in more detail in **section 3.5**.

The bond lengths obtained from Bragg- and PDF-Rietveld refinements are compared in **Table S3** within each of the forsterite samples**.** Based on Bragg-Rietveld refinements, the average bond lengths (further notated as <Mg(1)-O>, <Mg(2)-O>, and <Si-O>) of RFO and PFO are virtually identical, while bond lengths of HFO only differ by a maximum of 0.1 pm. Interestingly, <Mg(1)-O> and <Mg(2)-O>) of CFO are slightly longer than those of the defect-poor forsterites (∆1 pm (<Mg(1)-O>) and ∆0.5 pm (<Mg(2)-O>)). On the contrary, the <Si-O> of CFO is the shortest among all forsterites (∆2 pm). As a consequence, the bond valence sum (BVS) (Brese & O'Keeffe, 1991) of Si in the CFO is found to show over bonding (4.19(2) v.u.). Unlike the Bragg-Rietveld refinements, which suggest shorter <Si-O> bond lengths for CFO, the <Si-O> bonds determined through PDF-Rietveld refinements consistently display similar values. This results in a Si BVS of 3.84(3) v.u. across all forsterites. We attribute the different interatomic distances obtained from PDF-Rietveld and Bragg-Rietveld analyses to ACS limitation effects of the short synchrotron wavelength due to maximal observable average crystallite size (MOACS, (Gesing & Robben, 2024)) and the repeated observation. Furthermore, Rietveld refinements often describe local distortions, such as atom displacement, with an increase in the Debye-Waller factor (Abeykoon *et al.*, 2009).

3.5. DFT-PDF refinement

3.5.1. Single phase refinement

Small box (single unit cell)

In **section 3.4** the fitting results against crystalline Mg_2SiO_4 for all samples have been given. To receive a better fit of the structure model against the experimental PDF data of CFO, DFT-assisted PDF refinements (DFT-PDF) were implemented. As initial step, a geometry-optimized structure model of Mg_2SiO_4 without defects (GOSWD) was selected. Single-phase DFT-PDF refinements using this symmetry-free structure model showed a slightly better fit (R_{PDF} = 23 %) compared to the original (symmetry-constraint) model for defect-free, crystalline Mg_2SiO_4 (R_{PDF} = 26 %). Then, 17 structure models containing vacancy, Schottky, and Frenkel defects (see **Figure S1**) were generated from the DFT-PDF workflow (**section 2.7**). Furthermore, each DFT-PDF-generated structure model was individually selected for DFT-PDF refinement. Overall, the new defective structure models gave R_{PDF} in the range of 22 % - 28 %, where defects involving oxygen show the lowest values.

Large box (2x2x2 unit cells)

To realize lower concentrations of defects, larger systems (2x2x2 unit cells) were employed. To begin with, DFT-PDF refinements of a pristine 2x2x2 structure without further structure variation gave R_{PDF} of 37 %, while its GOSWD converged with R_{PDF} of 27 %. The significant mismatch observed between these refinements offers additional indications that the crystalline structure is unable to accommodate the defect-rich characteristics of the CFO sample. As before, 17 defective 2x2x2 models containing vacancy, Frenkel, and Schottky defects were generated from DFT-PDF optimization. The refinements converged with R_{PDF} in the range of 19 - 22 %. Nine of them (4 different vacancies, 2 Frenkel and 3 Schottky defects) have almost identical R_{PDF} values of 19 %.

Point defect (2x1x2 unit cells)

In a third approach, charge defect analysis was in focus. Both charged and neutral defects are considered for this calculation, for which the size of 2x1x2 unit cells was selected. In total, 10 defective 2x1x2 structure models were investigated: Mg interstitial and vacancy, O interstitial and vacancy, as well as Si interstitial. The refinements converged with R_{PDF} of 25-28 %, showing trends like the values for the single unit cells used. **Table S4** summarizes the R_{PDF} values of all defective structure candidates.

3.5.2. Stability of defective structure candidates

The calculated formation energies of the defective structure candidates are reported in **Table S4**. Positive numbers indicate metastable or unfavorable structures, whereas negative values indicate spontaneous or favorable formation of the structures. It can be observed that most of the structures have positive formation energies. Especially Schottky defects show the highest formation energies (>8 eV), and therefore those structures should be discarded as possible candidates. **Table 3** shows selected defective structure candidates (CIFs can be found in **SI**) with formation energies < 5 eV. Note, the formation energies in **Table 3** were not corrected to account for the formation of a single defect in the dilute limit, since we expect high defect concentrations in CFO. A complete list of formation energies at different defect concentrations and extrapolated for the dilute limit can be found in **Table S5**.

The interpretation of formation energies is not straightforward, since they strongly depend on the calculation scheme and the defect concentration/size of the simulation cell. Earlier studies by Walker et al. (Walker *et al.*, 2009, Walker *et al.*, 2003) did not consider the possible interaction between the defects, i.e. they performed a “mere” energy difference, hence the interaction of charged defects is long-ranged and sizeable. As improvement, we extrapolated the free energy of formation to infinite volume, i.e. to the dilute limit (using the formula shown in the **SI**). Nevertheless, similarly we found that Mg(1) Frenkel defects are energetically stable with a formation energy of 2.98 eV. In addition, we performed vacancy and interstitial supercell calculations with charged point defects and found comparable results to the available literature (Walker *et al.*, 2009, Walker *et al.*, 2003). At high defect concentrations, both Si^{4+} and Mg^{2+} interstitials seem to be the most energetically favorable. However, oxygen vacancies are found to be the most favorable defects in the extrapolated dilute limit (very low concentration). This could be the generalized gradient approximation (GGA) trend to overestimating oxygen bonds. **Table S5** summarizes the formation energy of charge defect structures computed using different fixed supercell sizes and extrapolated dilute limits.

Table 3 Selected defective structure candidates along with their symmetry analysis upon cell relaxation, formation energy, and R_{PDF} values. GOSWD = Geometry Optimized Structure Without Defect, F = Frenkel, I = Interstitial, V = Vacancy.

Defective structure candidate	Unit cell size	Symmetry analysis	Formation energy /eV	R_{PDF} /%
GOSWD	1	$Pbnm$ (62)*	0.01	23
Mg(1) F	1	$P\bar{1}$ (2)	2.98	25
Mg I +0	2x1x2	$P1$ (1)	3.73	27
Mg I +2	2x1x2	$P1$ (1)	-5.25	27
O I +0	2x1x2	$P1$ (1)	1.37	27
O V +2	2x1x2	$P1$ (1)	1.49	27
Si I +4	2x1x2	$P1$ (1)	-9.07	28

3.5.3. Multi-phase refinement

Ultimately, all structure motifs with favorable energy (as listed in **Table 3**) were used in combined multi-phase refinements. In principle, the respective defective structure is treated as a secondary phase alongside the crystalline one (GOSWD). The refined defective phases showing a negative scale factor were removed one at a time from the refinements. The best fit is finally achieved using a combination of a single unit cell of GOSWD and Mg(1) Frenkel, along with 2x1x2 Mg^{2+} interstitial defect structures which converge to R_{PDF} of 18 %, as illustrated in **Figure 7**. This fitting indicates that crushed forsterite (CFO) consists of 67(3) wt-%

GOSWD, 23(3) wt-% Mg Frenkel and 10(3) wt-% of Mg^{2+} interstitial. The optimized defective forsterite structure models are shown in **Figure 8**. Note, however, that any defect summarized in **Table 3** might possibly be present in defective Mg_2SiO_4, but not in the CFO sample with defects mechanically induced by ball milling. Although Si^{4+} interstitials might be favorable from an energetic point of view, this motif does not improve the PDF fit of CFO. Therefore, the presence of this type of defect is rather unlikely, and most probably prevented by the atmospheric reaction condition leading to a high concentration of oxygen-rich phases.

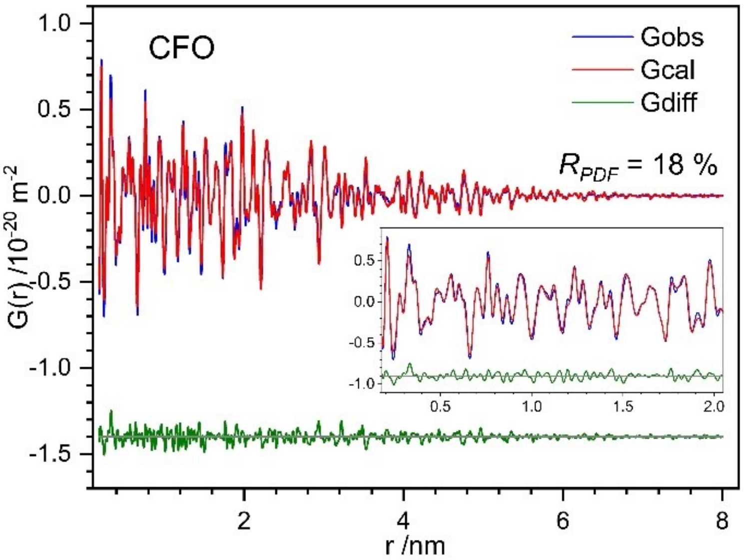

Figure 7 Multi-phase DFT-PDF refinement plot of crushed forsterite (CFO) in the long and short to medium (inset) range.

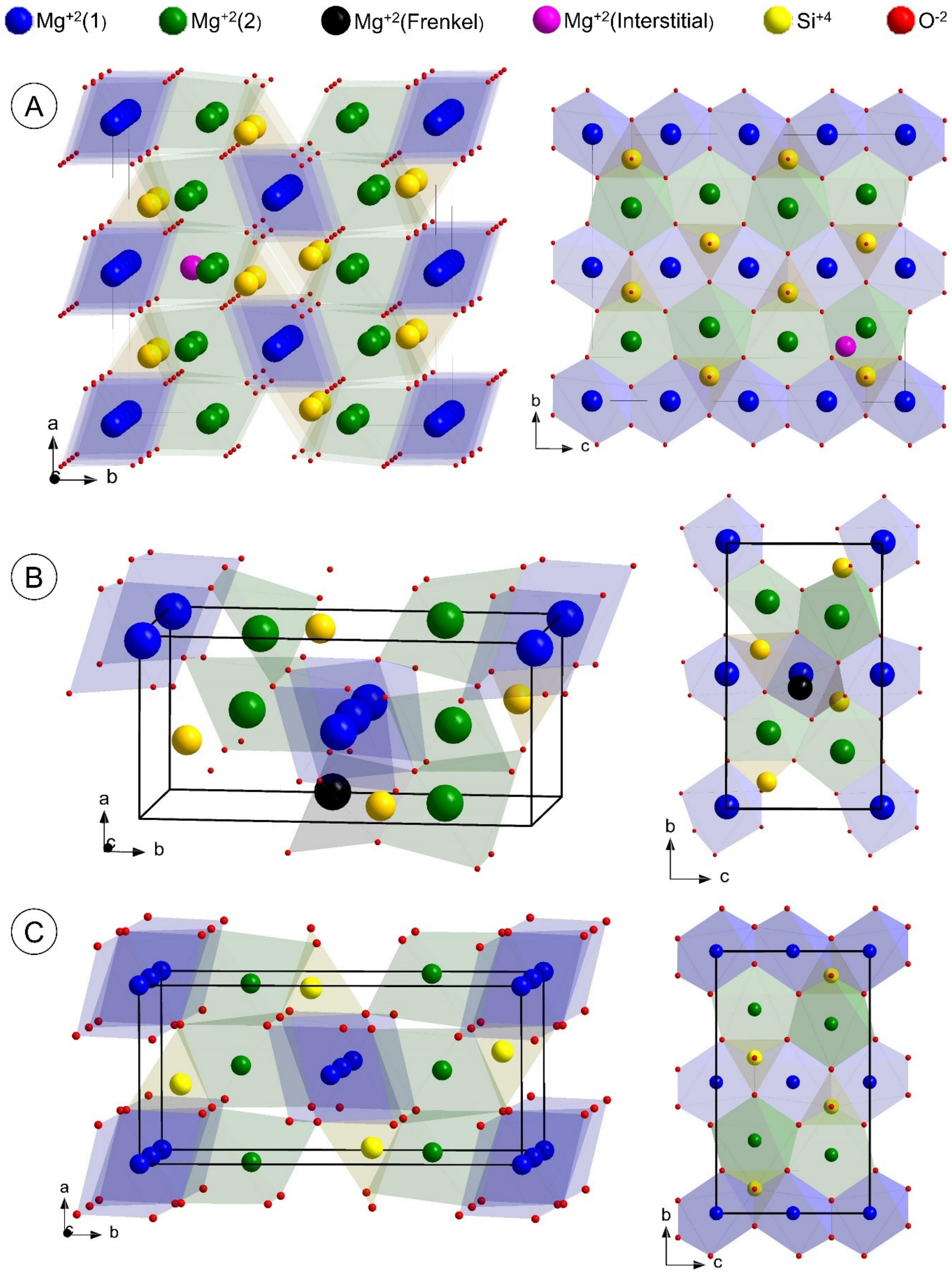

Figure 8 DFT-PDF optimized crystal structure of **(A)** 2x1x2 Mg^{2+} interstitial and **(B)** single unit cell Mg(1) Frenkel defects in comparison with **(C)** pristine forsterite structure.

4. Conclusion and outlook

Structural differences between defect-poor and defect-rich forsterite (Mg_2SiO_4) were investigated. Mechanically induced defect-rich forsterite was obtained by ball milling of defect-poor (pristine) forsterite. Implementing PDF-Rietveld refinements on X-ray synchrotron data indicated a complex disorder structure in the defect-rich forsterite. Raman peaks broadening and global red-shifts complemented the structural features of the defective phases. The defect-rich structure models were simulated using the DFT-PDF method to better describe the disorder in the local structure. DFT-PDF refinements indicate that post-processed forsterite contains Mg Frenkel-type and Mg^{2+} interstitial defects with concentrations of 23(3) and 10(3) wt-%, respectively. DFT calculations confirmed that the defective structure models are energetically stable. This finding is an important starting point to characterize and quantify defect-rich Martian regolith. Further investigations involving a larger number of phases are necessary as a stepwise strategy to structurally describe multi-phase Martian regolith. Additionally, a comparative study between radiation-induced defects and the mechanically induced defects described here would be of high demand to understand the mechanism of space weathering effects.

Acknowledgements We acknowledge support by the state of Bremen within the "Humans on Mars" initiative for APF "Materials on demand", Prof. Dr. Lucio Colombi Ciacchi, University of Bremen and Dr. Sokseiha Muy, EPFL Switzerland, for fruitful discussion on the project. We acknowledge DESY (Hamburg, Germany), a member of the Helmholtz Association HGF, for the provision of experimental facilities. Parts of this research were carried out at PETRA III and we would like to thank Dr. Alexander Schökel for assistance in using P02.1 Powder Diffraction and Total Scattering Beamline. AK acknowledges the Danish Research Council for covering travel expenses in relation to the synchrotron experiment (DanScatt) and the Deutsche Forschungsgemeinschaft (DFG, German science foundation) for funding of the project KI2427/1-1 (# 429360100). The authors gratefully acknowledge support from the Deutsche Forschungsgemeinschaft (DFG) under Germany's Excellence Strategy (EXC 2077, No. 390741603, University Allowance, University of Bremen), as well as computing time granted by the Resource Allocation Board and provided on the supercomputer Lise and Emmy at NHR@ZIB and NHR@Göttingen as part of the NHR infrastructure. The calculations for this research were conducted with computing resources under the project hbi00059. N.M. acknowledges support by the NCCR MARVEL, a National Centre of Competence in Research, funded by the Swiss National Science Foundation (grant number 205602).

Conflicts of interest The authors hereby state no conflict of interest.

Data availability The raw data can be obtained on request from the corresponding author.

References

Abeykoon, A. M., Donner, W., Brunelli, M., Castro-Colin, M., Jacobson, A. J. & Moss, S. C. (2009). *Journal of the American Chemical Society* **131**, 13230-13231.

Achilles, C. N., Downs, R. T., Ming, D. W., Rampe, E. B., Morris, R. V., Treiman, A. H., Morrison, S. M., Blake, D. F., Vaniman, D. T., Ewing, R. C., Chipera, S. J., Yen, A. S., Bristow, T. F., Ehlmann, B. L., Gellert, R., Hazen, R. M., Fendrich, K. V., Craig, P. I., Grotzinger, J. P., Des Marais, D. J., Farmer, J. D., Sarrazin, P. C. & Morookian, J. M. (2017). *Journal of Geophysical Research: Planets* **122**, 2344-2361.

Alkauskas, A., Deák, P., Neugebauer, J., Pasquarello, A. & Van de Walle, C. G. ((2011)). *Advanced calculations for defects in materials: Electronic structure methods*. John Wiley & Sons.

Angel, R. J. & Prewitt, C. T. (1986). *American Mineralogist* **71**, 1476-1482.

Bastonero, L. & Marzari, N. (2024). *Npj Computational Materials* **10**, 55.

Bennett, C. J., Pirim, C. & Orlando, T. M. (2013). Chemical reviews **113**, 9086-9150.

Bini, M., Ferrari, S., Capsoni, D., Mustarelli, P., Spina, G., Del Giallo, F., Lantieri, M., Leonelli, C., Rizzuti, A. & Massarotti, V. (2012). *RSC advances* **2**, 250-258.

Bisbo, M. K. & Hammer, B. (2020). *Physical review letters* **124**, 086102.

Bisbo, M. K. & Hammer, B. (2022). *Physical Review B* **105**, 245404.

Bish, D. L., Blake, D. F., Vaniman, D. T., Chipera, S. J., Morris, R. V., Ming, D. W., Treiman, A. H., Sarrazin, P., Morrison, S. M., Downs, R. T., Achilles, C. N., Yen, A. S., Bristow, T. F., Crisp, J. A., Morookian, J. M., Farmer, J. D., Rampe, E. B., Stolper, E. M. & Spanovich, N. (2013). *Science* **341**, 1238932.

Bowen, N., Greig, J. & Zies, E. (1924). *Journal of the Washington Academy of Sciences* **14**, 183-191.

Brese, N. & O'Keeffe, M. (1991). *Acta Crystallographica Section B: Structural Science* **47**, 192-197.

Campisi, D., Tielens, A. G. G. M. & Dononelli, W. (2024). *Monthly Notices of the Royal Astronomical Society* **533**, 2282-2293.

Certini, G., Karunatillake, S., Zhao, Y.-Y. S., Meslin, P.-Y., Cousin, A., Hood, D. R. & Scalenghe, R. (2020). *Planetary and Space Science* **186**,

Chauhan, A. & Chauhan, P. (2014). *J Anal Bioanal Tech* **5**, 1-5.

Chopelas, A. (1991). *American Mineralogist* **76**, 1101-1109.

Cline, J. P., Black, D. R., Gil, D., Henins, A. & Windover, D. (2010). *Materials Science Forum* **651**, 201-219.

Cong, R., Yang, T., Li, K., Li, H., You, L., Liao, F., Wang, Y. & Lin, J. (2010). *Acta Crystallographica Section B: Structural Science* **66**, 141-150.

Czaya, R. (1971). *Acta Crystallographica Section B* **27**, 848-849.

De, G., Karmakar, B. & Ganguli, D. (2000). *Journal of Materials Chemistry* **10**, 2289-2293.

Della Giusta, A., Ottonello, G. & Secco, L. (1990). *Acta Crystallographica Section B* **46**, 160-165.

Demidov, N., Bazilevskii, A. & Kuz'Min, R. (2015). *Solar System Research* **49**, 209-225.

Demtröder, W. (2008). *Laser spectroscopy: Vol. 1: Basic principles*. Springer Berlin Heidelberg, .

Dippel, A.-C., Liermann, H.-P., Delitz, J. T., Walter, P., Schulte-Schrepping, H., Seeck, O. H. & Franz, H. (2015). *Journal of Synchrotron Radiation* **22**, 675-687.

Dononelli, W. (2023). *Bunsen-Magazin* **6**, 204-207.

Egami, T. & Billinge, S. J. ((2003)). *Underneath the bragg peaks: Structural analysis of complex materials*. Elsevier.

Enkovaara, J., Rostgaard, C., Mortensen, J. J., Chen, J., Dułak, M., Ferrighi, L., Gavnholt, J., Glinsvad, C., Haikola, V. & Hansen, H. (2010). *Journal of physics: Condensed matter* **22**, 253202.

Farrow, C., Juhas, P., Liu, J., Bryndin, D., Božin, E., Bloch, J., Proffen, T. & Billinge, S. (2007). *Journal of Physics: Condensed Matter* **19**, 335219.

Fathi, M. H. & Kharaziha, M. (2008). *Materials Letters* **62**, 4306-4309.

Fathi, M. H. & Kharaziha, M. (2009). *Journal of Alloys and Compounds* **472**, 540-545.

Fischer, R. X., Schneider, H. & Gesing, T. M. ((2009)). *Acta Crystallographica A-Foundation and Advances*, pp. 232-233.

Freysoldt, C., Grabowski, B., Hickel, T., Neugebauer, J., Kresse, G., Janotti, A. & Van de Walle, C. G. (2014). *Reviews of modern physics* **86**, 253-305.

Fujino, K., Sasaki, S., Takeuchi, Y. & Sadanaga, R. (1981). *Acta Crystallographica Section B* **37**, 513-518.

Gesing, T. M., Murshed, M. M., Schuh, S., Thüringer, O., Krämer, K., Neudecker, T., Mendive, C. B. & Robben, L. (2022). *Journal of Materials Science* **57**, 1-20.

Gesing, T. M. & Robben, L. (2024). *Journal of Applied Crystallography*.

Giannozzi, P., Andreussi, O., Brumme, T., Bunau, O., Nardelli, M. B., Calandra, M., Car, R., Cavazzoni, C., Ceresoli, D. & Cococcioni, M. (2017). *Journal of physics: Condensed matter* **29**, 465901.

Giannozzi, P., Baroni, S., Bonini, N., Calandra, M., Car, R., Cavazzoni, C., Ceresoli, D., Chiarotti, G. L., Cococcioni, M. & Dabo, I. (2009). *Journal of physics: Condensed matter* **21**, 395502.

Giannozzi, P., Baseggio, O., Bonfà, P., Brunato, D., Car, R., Carnimeo, I., Cavazzoni, C., De Gironcoli, S., Delugas, P. & Ferrari Ruffino, F. (2020). *The Journal of chemical physics* **152**,

Gogolin, M., Murshed, M. M., Ende, M., Miletich, R. & Gesing, T. M. (2020). *Journal of Materials Science* **55**, 177-190.

Gouadec, G. & Colomban, P. (2007). *Progress in crystal growth and characterization of materials* **53**, 1-56.

Hanke, K. (1965). *Beiträge zur Mineralogie und Petrographie* **11**, 535-558.

Hazen, R. M. (1977). *American Mineralogist* **62**, 286-295.

Hofmeister, A. M. (1987). *Physics and Chemistry of Minerals* **14**, 499-513.

Huber, S. P., Zoupanos, S., Uhrin, M., Talirz, L., Kahle, L., Häuselmann, R., Gresch, D., Müller, T., Yakutovich, A. V. & Andersen, C. W. (2020). *Scientific data* **7**, 300.

Iishi, K. (1978). *American Mineralogist* **63**, 1198-1208.

Islam, N., Pradhan, A. & Kumar, S. (2005). *Journal of Applied Physics* **98**, 024309-024309.

Juhás, P., Davis, T., Farrow, C. L. & Billinge, S. J. (2013). *Journal of Applied Crystallography* **46**, 560-566.

Jundullah Hanafi, M. I., Murshed, M. M., Robben, L. & Gesing, T. M. (2024). *Zeitschrift für Kristallographie - Crystalline Materials*.

Kløve, M., Sommer, S., Iversen, B. B., Hammer, B. & Dononelli, W. (2023). *Advanced Materials* 2208220.

Kolesov, B. & Geiger, C. (2004). *Physics and Chemistry of Minerals* **31**, 142-154.

Komsa, H.-P., Rantala, T. T. & Pasquarello, A. (2012). *Physical Review B—Condensed Matter and Materials Physics* **86**, 045112.

Kudoh, Y. & Takeda, H. (1986). *Physica B+C* **139-140**, 333-336.

Lager, G. A., Ross, F. K., Rotella, F. J. & Jorgensen, J. D. (1981). *Journal of Applied Crystallography* **14**, 137-139.

Larsen, A. H., Mortensen, J. J., Blomqvist, J., Castelli, I. E., Christensen, R., Dułak, M., Friis, J., Groves, M. N., Hammer, B. & Hargus, C. (2017). *Journal of Physics: Condensed Matter* **29**, 273002.

Liu, Y., Tice, M., Schmidt, M., Treiman, A., Kizovski, T., Hurowitz, J., Allwood, A., Henneke, J., Pedersen, D. & VanBommel, S. (2022). *Science* **377**, 1513-1519.

Malavasi, L., Orera, A., Slater, P. R., Panchmatia, P. M., Islam, M. S. & Siewenie, J. (2011). *Chemical Communications* **47**, 250-252.

McKeown, D. A., Bell, M. I. & Caracas, R. (2010). *American Mineralogist* **95**, 980-986.

Mondal, K., Kumari, P. & Manam, J. (2016). *Current Applied Physics* **16**, 707-719.

Monkhorst, H. J. & Pack, J. D. (1976). *Physical review B* **13**, 5188.

Morimoto, N., Tokonami, M., Watanabe, M. & Koto, K. (1974). *American Mineralogist* **59**, 475-485.

Müller-Sommer, M., Hock, R. & Kirfel, A. (1997). *Physics and Chemistry of Minerals* **24**, 17-23.

Murshed, M. M., Nénert, G. & Gesing, T. M. (2012). *Zeitschrift für Kristallographie-New Crystal Structures* **227**, 285-286.

Naik, R., Prashantha, S. C., Nagabhushana, H., Sharma, S. C., Nagaswarupa, H. P., Anantharaju, K. S., Nagabhushana, B. M., Premkumar, H. B. & Girish, K. M. (2015). *Spectrochim Acta A Mol Biomol Spectrosc* **140**, 516-523.

Ni, S., Chou, L. & Chang, J. (2007). *Ceramics International* **33**, 83-88.

Perdew, J. P., Burke, K. & Ernzerhof, M. (1996). *Physical review letters* **77**, 3865.

Prandini, G., Marrazzo, A., Castelli, I. E., Mounet, N. & Marzari, N. (2018). *npj Computational Materials* **4**, 72.

Prashantha, S. C., Lakshminarasappa, B. N. & Nagabhushana, B. M. (2011). *Journal of Alloys and Compounds* **509**, 10185-10189.

Proffen, T., Billinge, S., Egami, T. & Louca, D. (2003). *Zeitschrift für Kristallographie-Crystalline Materials* **218**, 132-143.

Rietveld, H. M. (1969). *Journal of applied Crystallography* **2**, 65-71.

Rösler, H. J. ((1991)). *Lehrbuch der mineralogie*. Dt. Verlag für Grundstoffindustrie.

Scherrer, P. (1918). *Nachrichten von der Gesellschaft der Wissenschaften zu Göttingen, mathematisch-physikalische Klasse* **1918**, 98-100.

Schneider, H., Fischer, R. X., Gesing, T. M., Schreuer, J. & Muehlberg, M. (2012). *International journal of materials research* **103**, 422-429.

Smyth, J. R. & Hazen, R. M. (1973). *American Mineralogist* **58**, 588-593.

Souza, I., Íniguez, J. & Vanderbilt, D. (2002). *Physical review letters* **89**, 117602.

Stangarone, C., Böttger, U., Bersani, D., Tribaudino, M. & Prencipe, M. (2017). *Journal of Raman Spectroscopy* **48**, 1528-1535.

Swamy, V., Muddle, B. C. & Dai, Q. (2006). *Applied Physics Letters* **89**, 163118.

Tavangarian, F. & Emadi, R. (2010). *Materials Research Bulletin* **45**, 388-391.

Teck, M., Murshed, M. M., Schowalter, M., Lefeld, N., Grossmann, H. K., Grieb, T., Hartmann, T., Robben, L., Rosenauer, A., Mädler, L. & Gesing, T. M. (2017). *Journal of Solid State Chemistry* **254**, 82-89.

Terentjev, A. V., Constantin, L. A. & Pitarke, J. M. (2018). *Physical Review B* **98**, 214108.

Togo, A. (2023). *Journal of the Physical Society of Japan* **92**, 012001.

Togo, A., Chaput, L., Tadano, T. & Tanaka, I. (2023). *Journal of Physics: Condensed Matter* **35**, 353001.

Uhrin, M., Huber, S. P., Yu, J., Marzari, N. & Pizzi, G. (2021). *Computational Materials Science* **187**, 110086.

Umari, P. & Pasquarello, A. (2002). *Physical Review Letters* **89**, 157602.

Ungár, T. (2004). *Scripta Materialia* **51**, 777-781.

Váci, Z., Agee, C. B., Herd, C. D., Walton, E., Tschauner, O., Ziegler, K., Prakapenka, V. B., Greenberg, E. & Monique- Thomas, S. (2020). *Meteoritics & Planetary Science* **55**, 1011-1030.

Van de Walle, C. G., Laks, D., Neumark, G. & Pantelides, S. (1993). *Physical Review B* **47**, 9425.

Vaniman, D. T., Bish, D. L., Ming, D. W., Bristow, T. F., Morris, R. V., Blake, D. F., Chipera, S. J., Morrison, S. M., Treiman, A. H., Rampe, E. B., Rice, M., Achilles, C. N., Grotzinger, J. P., McLennan, S. M., Williams, J., Bell, J. F. I., Newsom, H. E., Downs, R. T., Maurice, S., Sarrazin, P., Yen, A. S., Morookian, J. M., Farmer, J. D., Stack, K., Milliken, R. E., Ehlmann, B. L., Sumner, D. Y., Berger, G., Crisp, J. A., Hurowitz, J. A., Anderson, R., Des Marais, D. J., Stolper, E. M., Edgett, K. S., Gupta, S., Spanovich, N. & Team, M. S. (2014). *Science* **343**,

Wagner, C. (1977). *Annual Review of Materials Science* **7**, 1-24.

Walker, A. M., Woodley, S. M., Slater, B. & Wright, K. (2009). *Physics of the Earth and Planetary Interiors* **172**, 20-27.

Walker, A. M., Wright, K. & Slater, B. (2003). *Physics and Chemistry of Minerals* **30**, 536-545.

Wang, A., Jolliff, B. L. & Haskin, L. A. (1995). *Journal of Geophysical Research: Planets* **100**, 21189-21199.

Wang, A., Kuebler, K., Jolliff, B. & Haskin, L. A. (2004). *Journal of Raman Spectroscopy* **35**, 504-514.

Yang, H., Shi, J., Gong, M. & Cheah, K. W. (2006). *Journal of Luminescence* **118**, 257-264.

Yu, W., Zeng, X., Li, X., Wei, G. & Fang, J. (2022). Earth and Space Science **9**, e2020EA001347.

Zampiva, R. Y. S., Acauan, L. H., dos Santos, L. M., de Castro, R. H. R., Alves, A. K. & Bergmann, C. P. (2017). *Ceramics International* **43**, 16225-16231.

Zhang, S. & Northrup, J. E. (1991). *Physical review letters* **67**, 2339.

Zimmermann, N. E., Horton, M. K., Jain, A. & Haranczyk, M. (2017). *Frontiers in Materials* **4**, 34.

Supporting information

Synthesis, structural and spectroscopic characterization of defect-rich forsterite as a representative phase of Martian regolith

Md. Izzuddin Jundullah Hanafi[a,b], Lorenzo Bastonero[b,c], M. Mangir Murshed[a,b*], Lars Robben[a,b], Wilke Dononelli[b,c], Andrea Kirsch[d], Nicola Marzari[b,c], Thorsten M. Gesing[a,b]

[a] University of Bremen, Institute of Inorganic Chemistry and Crystallography, Leobener Straße 7, D-28359 Bremen, Germany

[b] University of Bremen, MAPEX Center for Materials and Processes, Bibliothekstraße 1, D-28359 Bremen, Germany

[c] Bremen Center for Computational Materials Science and Hybrid Materials Interfaces Group, Am Fallturm 1, D-28359 Bremen, Germany

[d] University of Copenhagen, Department of Chemistry and Nanoscience Center, Universitetsparken 5, 2100, Copenhagen, Denmark

*Corresponding author: e-mail: murshed@uni-bremen.de, phone: +49 (0)421 218 63144

ORCID:

MIJH:	0009-0005-7842-6751
LB:	0000-0001-9374-1876
MMM:	0000-0002-9063-372X
LR:	0000-0002-0534-9573
WD:	0000-0001-7577-421X
AK:	0000-0003-2602-7415
NM:	0000-0002-9764-0199
TMG:	0000-0002-4119-2219

S1. Defect formation energy in the dilute limit

The dilute limit for (point) defects assumes that a single defect is present in an infinite perfect crystal. This is a good approximation when its concentration is limited to a few percentage (Freysoldt *et al.*, 2014). When the defect is charge, the simulation in periodic boundary conditions (PBC) comes with a number of cautions to take into account. The major issue is the slow decay of the long-range nature of the Coulomb interaction, which decays as the inverse of the cell size L (Komsa *et al.*, 2012), or equivalently as the inverse cube root of the cell volume Ω. To extrapolate the value in the dilute limit, one could adopt a correction scheme (Komsa *et al.*, 2012) or alternatively extract the value from a series of supercells calculations. The formation energy can be written as a function of the defective supercell volume (subject to PBC), as:

$$E^f[\Omega] = E^f{}_{\infty} + \frac{a}{\Omega^{1/3}} + \frac{b}{\Omega}$$

where $E^f{}_{\infty}$, a, and b are parameters to fit. In particular, $E^f{}_{\infty}$ represents the formation energy in the dilute limit, i.e. when $\Omega \to \infty$. Using the formation energies in **Table S5**, $E^f{}_{\infty}$ is extrapolated for all the presented charged defects. A rigorous treatment of the electrostatic should also account for the misalignment of the average potential with the reference pristine bulk (Freysoldt *et al.*, 2014). Nevertheless, this results in small energy corrections, usually lower than 1 eV/atom (Freysoldt *et al.*, 2014). Since our calculated formation energies are well separated in energy and considering we do not need such accuracy for screening the type of defects for the further refinement, we neglect this extra term in the prediction of the formation energy in the dilute limit in this study.

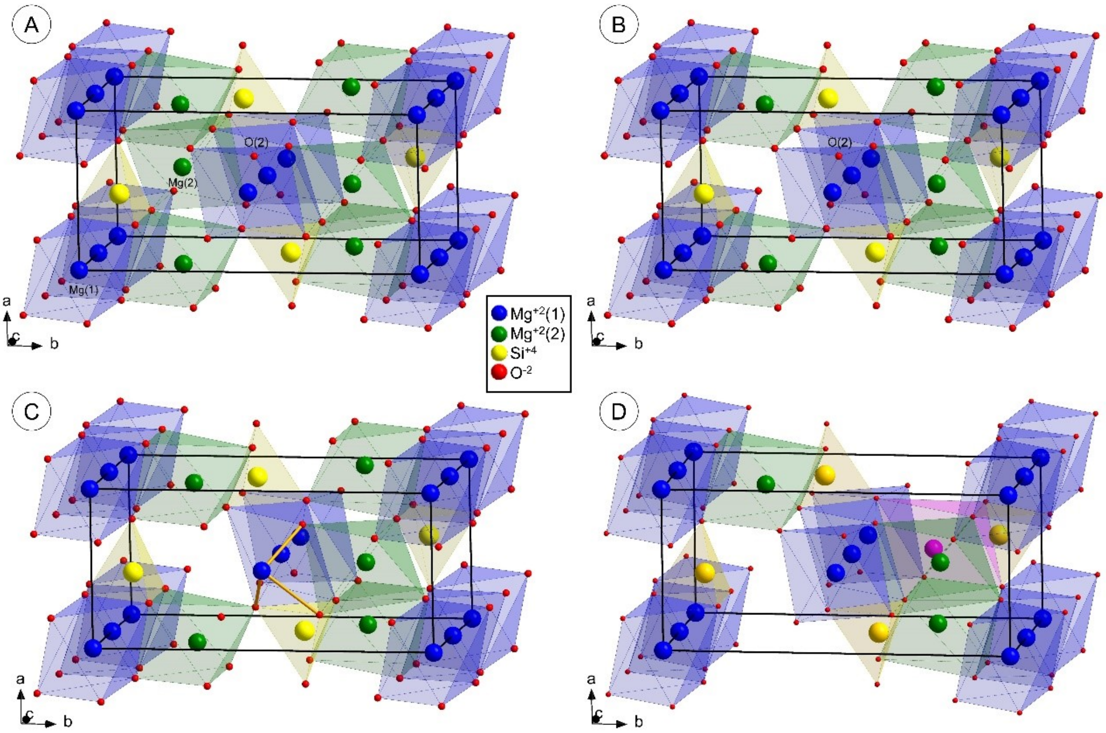

Figure S1 Crystal structure of **(A)** pristine forsterite, defective forsterite with **(B)** vacancy in Mg(2)-site. **(C)** Schottky Mg(2)-O(2) where both atoms are missing, and **(D)** Frenkel where Mg(2) is dislocated (coloured in pink) close to another Mg(2)-site.

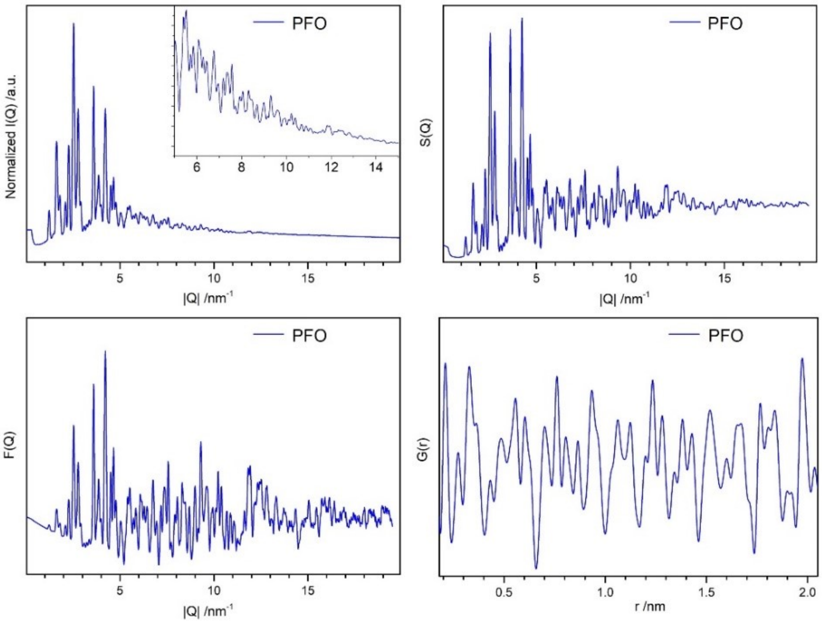

Figure S2 Powder X-ray diffraction data of PFO, showing plots of *I(Q)*, *S(Q)*, *F(Q)*, and *G(r)*.

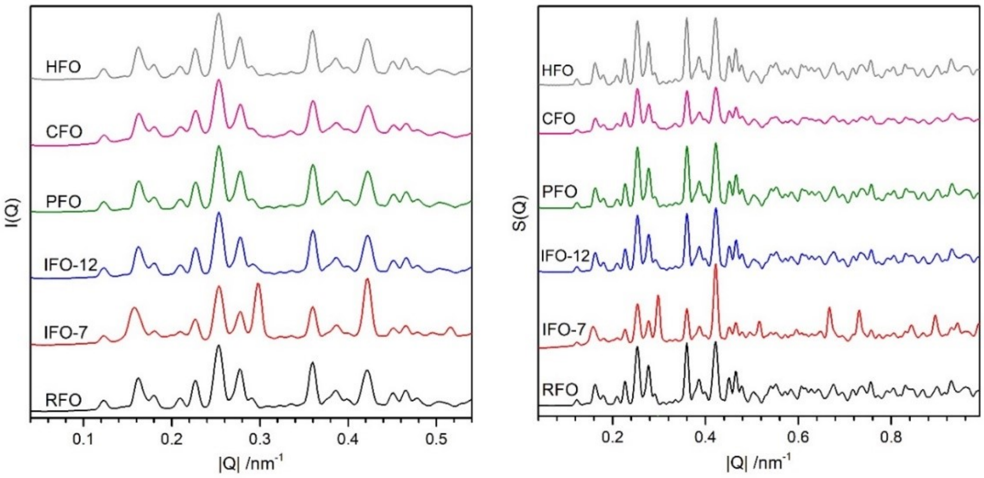

Figure S3 *I(Q)* and *S(Q)* of all synthesized samples.

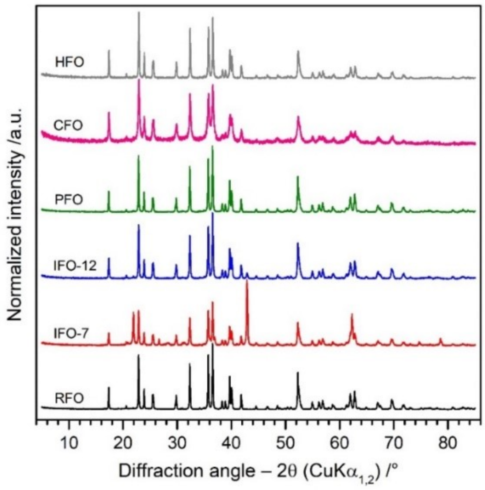

Figure S4 X-ray powder diffraction patterns of synthesized samples.

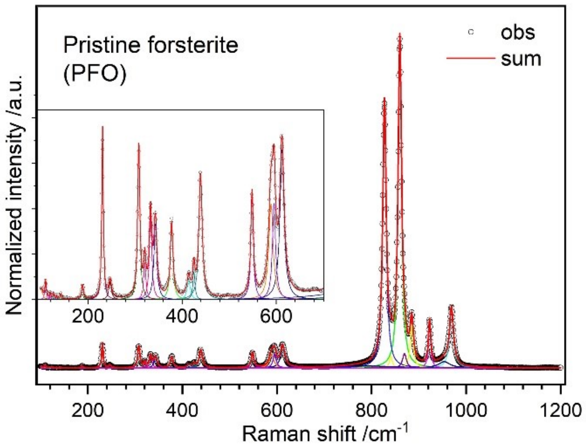

Figure S5 Representative peak fitting of a forsterite Raman spectrum synthesized by ball mill method.

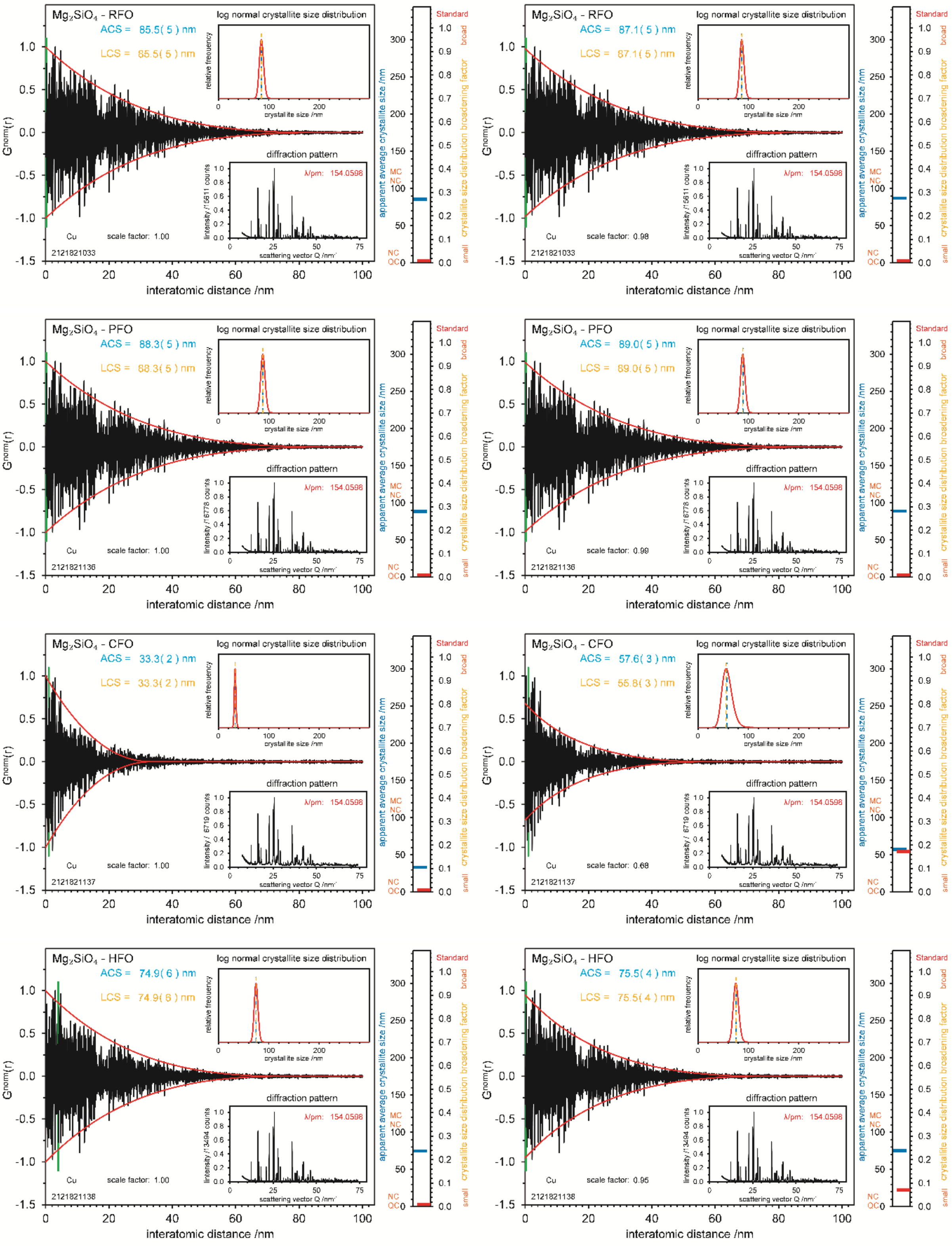

Figure S6 EnvACS plots of refinements without (left) and with (right) including a variable scale factor for RFO, PFO, CFO and HFO.

Table S1 Comparative metric and structural parameters of forsterites obtained from Bragg-Rietveld refinements of XRPD data.

Atom	Site	x	y	z	B_{iso} /10^4 pm^2
Literature (Smyth & Hazen, 1973), *Pbnm*, a = 475.6(1) pm, b = 1020.7(1) pm, c = 598.0(1) pm					
Mg(1)	4a	0	0	0	0.26(1)
Mg(2)	4c	0.9915(2)	0.2774(1)	0.25	0.22(1)
Si	4c	0.4262(1)	0.0940(1)	0.25	0.08(1)
O(1)	4c	0.7657(3)	0.0913(2)	0.25	0.27(2)
O(2)	4c	0.2215(4)	0.4474(2)	0.25	0.24(2)
O(3)	8d	0.2777(2)	0.1628(1)	0.0331(2)	0.27(2)
RFO sample, *Pbnm*, a = 475.15(1) pm, b = 1021.26(2) pm, c = 598.54(1) pm, R_{wp} = 11(1) %					
Mg(1)	4a	0	0	0	0.81(4)
Mg(2)	4c	0.9919(4)	0.2775(1)	0.25	0.81(4)
Si	4c	0.4272(3)	0.0941(2)	0.25	0.57(4)
O(1)	4c	0.7626(5)	0.0922(3)	0.25	0.40(5)
O(2)	4c	0.2195(5)	0.4500(3)	0.25	0.40(5)
O(3)	8d	0.2804(4)	0.1617(2)	0.0357(3)	0.40(5)
PFO sample, *Pbnm*, a = 475.30(1) pm, b = 1020.84(2) pm, c = 598.48(1) pm, R_{wp} = 11(1) %					
Mg(1)	4a	0	0	0	0.95(4)
Mg(2)	4c	0.9929(4)	0.2775(2)	0.25	0.95(4)
Si	4c	0.4268(3)	0.0940(2)	0.25	0.76(4)
O(1)	4c	0.76226)	0.0923(3)	0.25	0.54(5)
O(2)	4c	0.2205(6)	0.4501(4)	0.25	0.54(5)
O(3)	8d	0.2802(4)	0.1621(2)	0.0358(4)	0.54(5)
CFO sample, *Pbnm*, a = 475.46(5) pm, b = 1020.48(1) pm, c = 598.40(7) pm, R_{wp} = 15(1) %					
Mg(1)	4a	0	0	0	2.74(11)
Mg(2)	4c	0.9840(1)	0.2766(4)	0.25	2.74(11)
Si	4c	0.4300(9)	0.0983(4)	0.25	2.89(13)
O(1)	4c	0.7578(15)	0.0878(9)	0.25	2.20(14)
O(2)	4c	0.2211(15)	0.4490(11)	0.25	2.20(14)
O(3)	8d	0.2762(11)	0.1546(6)	0.0510(10)	2.20(14)
HFO sample, *Pbnm*, a = 475.24(2) pm, b = 1020.30(4) pm, c = 598.23(2) pm, R_{wp} = 15(1) %					
Mg(1)	4a	0	0	0	3.18(7)
Mg(2)	4c	0.9915(7)	0.2769(2)	0.25	3.18(7)
Si	4c	0.4275(5)	0.0949(3)	0.25	2.95(8)
O(1)	4c	0.7616(9)	0.0907(5)	0.25	2.68(9)
O(2)	4c	0.2162(8)	0.4518(6)	0.25	2.68(9)
O(3)	8d	0.2833(6)	0.1583(4)	0.0435(6)	2.68(9)

Table S2 Raman frequencies (cm^{-1}) of the deconvoluted peak maxima of different forsterites are compared with those of theoretical (PBEsol) and literature values.

Raman shift /cm^{-1}								
RFO	**PFO**	**CFO**	**HFO**	**(Kolesov & Geiger, 2004)**	**(Stangarone *et al.*, 2017)**	**(McKeown *et al.*, 2010)**	**PBEsol**	**Assignment**
-	-	-	-	-	-	-	171	B_{2g}
-	-	-	-	-	-	-	183	A_g
188(1)	188(1)	187(1)	187(1)	184	191	190	186	B_{3g}
-	-	-	-	-	-	-	216	B_{1g}
-	-	-	-	-	-	-	219	A_g
231(1)	231(1)	229(1)	230(1)	227	228	224	240	B_{2g}
247(1)	247(1)	241(1)	246(1)	243	234	246	250	B_{1g}
-	-	-	-	-	-	-	279	B_{3g}
307(1)	308(1)	303(1)	306(1)	304	304	-	304	A_g
-	-	-	-	-	-	-	310	B_{3g}
-	-	-	-	-	-	-	313	B_{1g}
320(1)	320(1)	319(1)	319(1)	316	315	317	318	B_{2g}
332(1)	333(1)	330(1)	332(1)	329	324	332	322	A_g
343(1)	343(1)	338(1)	341(1)	-	336	-	338	A_g
-	-	-	-	-	351	354	348	B_{1g}
-	-	-	-	-	-	-	360	B_{2g}
-	-	-	-	373	372	383	370	B_{3g}
377(1)	377(1)	374(1)	376(1)	-	378	-	375	B_{1g}
-	-	-	-	-	-	-	404	B_{3g}
414(1)	414(1)	412(1)	412(1)	421	424	-	419	A_g
424(1)	425(1)	422(1)	424(1)	434	432	433	430	B_{1g}
439(1)	439(1)	435(1)	437(1)	-	448	443	433	B_{2g}
-	-	-	-	-	-	-	520	A_g
548(1)	549(1)	544(1)	547(1)	544	556	534	556	B_{1g}
-	-	-	-	-	-	-	559	B_{2g}
589(1)	588(1)	-	-	588	594	574	566	B_{3g}
595(1)	595(1)	590(1)	591(1)	-	603	582	586	A_g
612(1)	612(1)	610(1)	611(1)	608	605	600	608	B_{1g}
-	-	-	-	-	-	-	805	A_g
827(1)	827(1)	825(1)	826(1)	824	819	821	817	B_{1g}
841(1)	841(1)	-	840(1)	838	834	-	836	A_g
860(1)	860(1)	857(1)	859(1)	856	857	852	845	B_{1g}
869(1)	869(1)	-	-	866	867	861	863	B_{2g}
885(1)	885(1)	882(1)	884(1)	882	886	880	900	B_{3g}
923(1)	922(1)	920(1)	922(1)	920	929	917	945	A_g
969(1)	969(1)	965(1)	967(1)	966	974	967	956	B_{1g}

Table S3 Selective interatomic distances (/pm) and their average values (<M-O>) in Mg_2SiO_4 obtained from Bragg- and PDF-Rietveld refinements along with the bond valence sum (BVS).

Bond length	Method	Sample			
		RFO	**PFO**	**CFO**	**HFO**
Si-O(1)	Bragg	162.0(1)	162.0(1)	159.2(1)	162.1(1)
	PDF	*162.0(2)*	*162.4(2)*	*161.4(3)*	*162.3(2)*
Si-O(2)	Bragg	163.8(1)	163.8(1)	160.8(1)	163.7(1)
	PDF	*164.2(2)*	*164.2(2)*	*163.9(2)*	*164.7(2)*
Si-O3 (2x)	Bragg	162.0(1)	162.0(1)	161.3(1)	161.9(1)
	PDF	*163.8(2)*	*163.9(2)*	*165.2(2)*	*164.3(2)*
<Si-O>	Bragg	162.6(1)	162.6(1)	160.7(1)	162.4(1)
	PDF	*163.3(2)*	*163.5(2)*	*163.5(3)*	*163.8(2)*
BVS	Bragg	3.99(1)	3.99(2)	4.19(2)	4.00(1)
	PDF	*3.89(2)*	*3.87(2)*	*3.84(3)*	*3.84(1)*
Mg(1)-O(1) (2x)	Bragg	208.5(1)	208.5(1)	210.5(1)	208.4(1)
	PDF	*208.3(1)*	*208.5(2)*	*210.7(8)*	*208.7(2)*
Mg(1)-O(2) (2x)	Bragg	207.2(1)	207.2(1)	207.2(1)	207.2(1)
	PDF	*207.7(1)*	*208.3(1)*	*208.1(7)*	*207.6(2)*
Mg(1)-O(3) (2x)	Bragg	213.3(1)	213.3(1)	214.0(1)	213.3(1)
	PDF	*212.7(2)*	*212.9(2)*	*214.8(8)*	*212.7(2)*
<Mg(1)-O>	Bragg	209.7(1)	209.7(1)	210.6(1)	209.6(1)
	PDF	*209.6(2)*	*209.9(2)*	*211.2(8)*	*209.7(2)*
BVS	Bragg	2.02(1)	2.02(1)	1.97(1)	2.02(1)
	PDF	*2.02(1)*	*2.00(1)*	*1.94(4)*	*2.02(1)*
Mg(2)-O(1)	Bragg	217.1(1)	217.0(1)	217.8(1)	216.9(1)
	PDF	*217.5(3)*	*216.8(4)*	*218.2(4)*	*216.6(2)*
Mg(2)-O(2)	Bragg	206.2(1)	206.1(1)	206.9(1)	206.1(1)
	PDF	*204.8(3)*	*204.5(3)*	*203.0(4)*	*204.7(2)*
Mg(2)-O(3) (2x)	Bragg	208.2(1)	208.2(1)	208.6(1)	208.1(1)
	PDF	*206.3(2)*	*206.4(3)*	*205.7(5)*	*206.4(2)*
Mg(2)-O(3) (2x)	Bragg	220.4(1)	220.4(1)	220.6(1)	220.4(1)
	PDF	*222.5(3)*	*222.4(4)*	*220.5(4)*	*221.9(2)*
<Mg(2)-O>	Bragg	213.4(1)	213.4(1)	213.9(1)	213.3(1)
	PDF	*213.3(3)*	*213.2(4)*	*212.3(5)*	*213.0(2)*
BVS	Bragg	1.85(1)	1.85(1)	1.82(1)	1.85(1)
	PDF	*1.86(2)*	*1.87(2)*	*1.92(2)*	*1.88(1)*

Table S4 Defective structure candidates along with their symmetry analysis, formation energy, and R_{PDF} values. GOSWD = Geometry Optimized Structure Without Defect, F = Frenkel, I = Interstitial, V = Vacancy. Several structure models (noted with *) fall back to the pristine structure upon optimization.

Defective structure candidate	Unit cell size	Space group	Formation energy /eV	R_{PDF} /%
GOSWD	1	$Pbnm$ (62)*	0.01	23
GOSWD	*2x2x2*	$Pbnm$ (62)*	*0.01*	*27*
Frenkel defect				
Mg(1)	1	$P\bar{1}$ (2)	2.98	25
Mg(1)	*2x2x2*	$P1$ (1)	*5.41*	*20*
Mg(2)	1	$Pbnm$ (62)*	0.01	26
Mg(2)	*2x2x2*	$Pbnm$ (62)*	*0.01*	*20*
O(1)	1	$P1$ (1)	7.92	23
O(1)	*2x2x2*	$P1$ (1)	*7.64*	*21*
O(2)	1	$Pbnm$ (62)*	0.01	27
O(2)	*2x2x2*	$P1$ (1)	*7.69*	*19*
O(3)	1	$Pbnm$ (62)*	0.01	27
O(3)	*2x2x2*	$P1$ (1)	*7.69*	*19*
Vacancy defect				
Mg(1)	1	$P1$ (1)	9.06	26
Mg(1)	*2x2x2*	$P1$ (1)	*9.11*	*19*
Mg(2)	1	Pm (6)	10.14	23
Mg(2)	*2x2x2*	Pm (6)	*10.27*	*19*
O(1)	1	Pm (6)	6.44	23
O(1)	*2x2x2*	Pm (6)	*6.51*	*22*
O(2)	1	$P1$ (1)	6.54	22
O(2)	*2x2x2*	$P1$ (1)	*6.56*	*21*
O(3)	1	$P1$ (1)	6.54	23
O(3)	*2x2x2*	$P1$ (1)	*6.56*	*19*
Si	1	$P1$ (1)	12.37	25
Si	*2x2x2*	$P1$ (1)	*12.37*	*19*
Schottky defect				
Mg(1)-O(1)	1	$P1$ (1)	10.59	25
Mg(1)-O(1)	*2x2x2*	$P1$ (1)	*11.64*	*19*
Mg(1)-O(2)	1	$P1$ (1)	8.79	28
Mg(1)-O(2)	*2x2x2*	$P1$ (1)	*9.88*	*19*
Mg(1)-O(3)	1	$P1$ (1)	9.22	28

Mg(1)-O(3)	*2x2x2*	$P1$ (1)	*9.80*	*20*
Mg(2)-O(1)	1	$P1$ (1)	9.69	24
Mg(2)-O(1)	*2x2x2*	$P1$ (1)	*13.99*	*20*
Mg(2)-O(2)	1	$P1$ (1)	9.55	28
Mg(2)-O(2)	*2x2x2*	$P1$ (1)	*10.87*	*19*
Mg(2)-O(3)	1	$P1$ (1)	9.55	28
Mg(2)-O(3)	*2x2x2*	$P1$ (1)	*10.98*	*23*
Charge defect				
Mg I +0	2x1x2	$P1$ (1)	3.73	27
Mg I +2	*2x1x2*	$P1$ (1)	*-5.25*	*27*
Mg V -2	2x1x2	$P1$ (1)	9.05	25
Mg V +0	*2x1x2*	$P1$ (1)	*9.25*	*25*
O I +0	2x1x2	$P1$ (1)	1.37	27
O I -2	*2x1x2*	$P1$ (1)	*10.24*	*23*
O V +2	2x1x2	$P1$ (1)	1.49	27
O V +0	*2x1x2*	$P1$ (1)	*6.66*	*27*
Si I +0	2x1x2	$P1$ (1)	6.39	27
Si I +4	*2x1x2*	$P1$ (1)	*-9.07*	*28*

Table S5 Formation energy of charge defect structures computed using different fixed supercell size and dilute limit*. F = Frenkel, I = Interstitial, V = Vacancy.

Defective structure candidate	**Formation energy /eV Unit cell size**					
	1	**2x1x2**	**3x1x2**	**3x2x2**	**3x2x3**	**Dilute limit**
Mg I +0	3.13	3.73	3.99	4.29	4.24	
Mg I +2	*-6.45*	*-5.25*	*-4.99*	*-4.78*	*-4.90*	*-4.64*
Mg V +0	9.15	9.25	9.27	9.38	11.49	
Mg V -2	*6.46*	*9.05*	*9.38*	*9.80*	*9.77*	*10.21*
O I +0	1.76	1.37	1.38	1.40	1.24	
O I -2	*1.74*	*10.24*	*10.53*	*6.32*	*6.46*	*-9.63*
O V +0	6.45	6.66	6.73	6.72	6.56	
O V +2	*0.77*	*1.49*	*1.65*	*1.87*	*1.71*	*2.00*
Si I +0	4.33	6.39	8.67	6.77	6.68	
Si I +4	*-13.39*	*-9.07*	*-8.14*	*-7.30*	*-7.13*	*-4.92*

Chapter 5

Synthesis and characterizations of plagioclase feldspars $(Ca_{1-x}Na_x)(Al_{2-x}Si_{2+x})O_8$: mechanical weathering relevant to Martian regolith

Manuscript in preparation.

Md. Izzuddin Jundullah Hanafi, M. Mangir Murshed*, Lars Robben, Thorsten M. Gesing

University of Bremen, Institute of Inorganic Chemistry and Crystallography, Leobener Straße 7, D-28359 Bremen, Germany

University of Bremen, MAPEX Center for Materials and Processes, Bibliothekstraße 1, D-28359 Bremen, Germany

*Corresponding author: murshed@uni-bremen.de, phone: +49 (0)421 218 63144

ORCID:

MIJH:	0009-0005-7842-6751
MMM:	0000-0002-9063-372X
LR:	0000-0002-0534-9573
TMG:	0000-0002-4119-2219

ABSTRACT

Plagioclase feldspars draw intensive interplanetary research attentions because of its abundance in the Martian regolith. It is predicted to consist of defect-rich crystal structures due to long-lasting space weathering by mechanical impact from extra-terrestrial objects and the solar wind radiation. For possible future human settlement on Mars, the available plagioclase feldspars would be of crucial importance within the frame of in-situ resource utilization process. As such, the present report focuses on the synthesis of representative plagioclase feldspars and their simulated mechanical weathering using ball milling. A series of $(Ca_{1-x}Na_x)(Al_{2-x}Si_{2+x})O_8$ plagioclase feldspars are synthesized using an established solid-state method with subsequent calcination schemes. The crystal structure of each phase pure sample is characterized by X-ray powder diffraction and Rietveld refinement. The bulk chemical compositions obtained from energy dispersive X-ray spectroscopy have been used to obtain for Al/Si ratio in the sample. The total scattering data are collected using in-house X-ray facilities, and analyzed by pair distribution function refinements. The vibrational modes of the synthetic plagioclase feldspars are evaluated by Raman spectroscopy, complementing the local structural features.

Keywords: plagioclase feldspar, mechanical weathering, SEM/EDX, X-ray, PDF, Raman

1. Introduction

Plagioclase feldspars are volumetrically the most dominant mineral in the Martian crust [1]. The highly-abundant plagioclase feldspars on the Marian surface were detected by thermal infrared [2], visible near-infrared spectroscopy [3, 4], and in-situ X-ray diffraction data from the *Mars Science Laboratory* on the rover *Curiosity* [5, 6]. Bish et al. [5] reported that approximately 41 wt-% of plagioclase feldspar was identified in Martian soil, which is later supported by Achilles et al. [6] who estimates a value between 36 wt-% and 41 wt-%. The X-ray diffraction data analysis suggested an amorphous fraction in Martian regolith, which ranges from 28 wt-% to 45 wt-% [5-8]. Such high concentration of amorphous content in Martian regolith can be understood due to extreme weathering [9] by mechanical impact from extraterrestrial object [10-12], as well as the solar wind radiation [13-15]. Assuming future human settlement on Mars, in-situ resource utilization (ISRU) of these plagioclase feldspars for building materials would be of great research attention. As such, investigation on representative plagioclase feldspars and their simulated mechanical weathering are of crucial importance. Details of their structural and spectroscopic characterizations are necessary prior to human's mission on Mars.

Plagioclase feldspars belong to MT_4O_8 aluminosilicates group, with a structure composed of corner-sharing AlO_4 and SiO_4 tetrahedra (T) linked in an infinite three-dimensional array [16] as shown in **Figure 1**. The tetrahedra are arranged in four-membered rings which are stacked to form crankshafts parallel to the crystallographic **a**–axis. The crankshafts are connected together in an open structure with large cavities to accommodate alkali- or alkaline earth metals (M). The structural complexity of plagioclase feldspar arises from the interplay between the Al/Si ordering among these tetrahedra and the displacive distortions of the entire framework [17]. Due to variation of the Al/Si molar ratio in the $(Ca_{1-x}Na_x)(Al_{2-x}Si_{2+x})O_8$ plagioclase feldspars, a different type of tetrahedra ordering occurs within the solid solution [18-20]. Of particular crystal-chemical aspects, the anorthite ($CaAl_2Si_2O_8$) endmember with Al:Si = 2:2 allows for a complete long range order with $I\overline{1}$ [21] symmetry, whereas the albite ($NaAlSi_3O_8$)

endmember with Al:Si = 1:3 crystallizes in the space group $C\bar{1}$ [22] with short range order. Kroll and Müller [23] suggested that the $I\bar{1} \leftrightarrow C\bar{1}$ transformation occurs between x = 0.3 and x = 0.4. Later, Carpenter and McConnell [24] determined this transformation as a steep line passing through the points ~x = 0.41 at 1273 K and ~x = 0.23 at 1713 K in the anorthite-albite binary phase diagram.

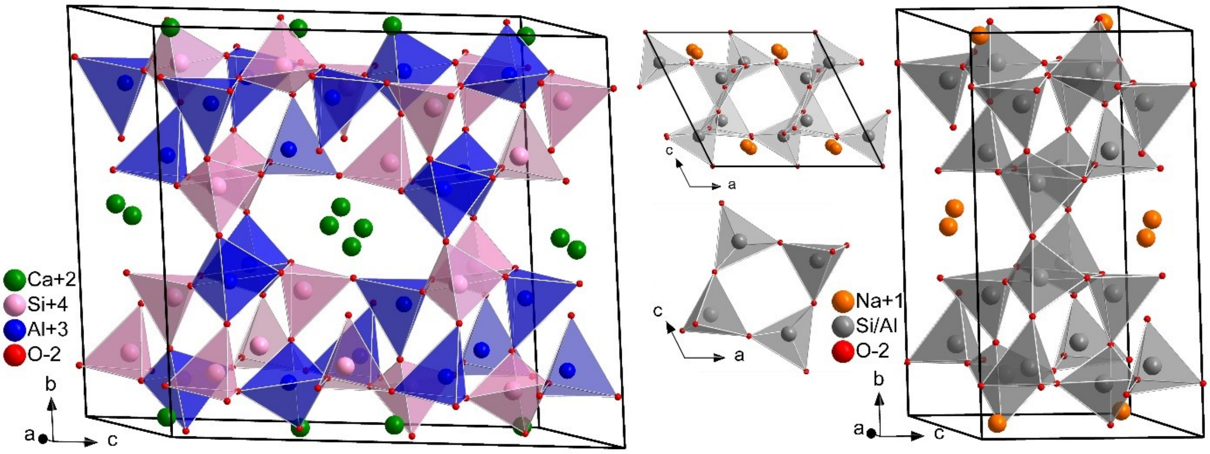

Figure 1. Crystal structures of anorthite (left) and albite (right). The crankshaft chain parallel to **a**–axis (mid-top) are built from stacked four-membered ring (mid-bottom).

Several studies have been conducted on naturally occurred plagioclase feldspars with particular interests on its bulk moduli [25], thermodynamic properties [26] and dissolution rate [27]. Synthesis of both single crystals [28, 29] and polycrystalline plagioclase feldspars ceramics [30-32] by various techniques have been reported earlier. Li et al. [32] reported synthesis of plagioclase feldspars for x = 0, 0.2, 0.4 and 0.67 with focus of the microwave dielectric properties. Krzmanc et al. [31] extended the solid solution for x = 0, 0.2, 0.4, 0.6, 0.67, 0.8 and 1. To the best of our knowledge, a systematic crystal-chemical study is still missing for a complete solid solution of plagioclase feldspars and their post-mechanical weathering effect relevant to Martian regolith.

The present study mainly addresses the synthesis and characterization of plagioclase feldspars $(Ca_{1-x}Na_x)(Al_{2-x}Si_{2+x})O_8$ for $x = 0 – 1.0$ with $\Delta x = 0.1$. Since mechanical stress can simulate mechanical weathering [33], leading to induce defects and amorphous contents [34, 35], selective members are mechanically weathered using high energy ball mill to represent the defect-rich Martian plagioclase feldspars. Details of the structural features of each member of the solid solution is characterized using X-ray powder diffraction (XRPD) and X-ray total scattering, followed by Rietveld and pair distribution function (PDF) [36-38] analysis, respectively. In addition, Raman spectroscopy and SEM/EDX were used as complementary characterization.

2. Materials and methods

2.1. Synthesis

Calcium carbonate ($CaCO_3$, ChemPUR 99 %), sodium carbonate ($NaCO_3$, ORG Laborchemie 99.5 %), Kaolin ($Al_2Si_2O_5(OH)_4$, Sigma-Aldrich) and amorphous SiO_2 (Thermo scientific 99.9 %) were used as starting materials. Stoichiometric amounts of aforementioned starting materials were ground in an agate mortar. The mixed powder was transferred to a porcelain crucible and calcined in a muffle furnace at 1173 K for 12 h. The obtained solid was ground and pressed into a pellet using uniaxial force of 10 kN in a 20 mm diameter cylinder mold for 5 minutes. The pellets were placed on a platinum sheet and calcined in air for 5 days at various final temperature, as listed in **Table 1**, with heating- and cooling rate of 10 and 3 K/min, respectively. The solid was then hammered into coarse pieces and finely ground for further characterization. Selective members of $(Ca_{1-x}Na_x)(Al_{2-x}Si_{2+x})O_8$ plagioclase feldspars ($x = 0$, 0.4 and 1) were mechanically weathered using high energy ball milling to accumulate potential energy and introduce defects on their surface [39]. Each powder was milled with tungsten carbide (WC) jar and balls. The ball to powder ratio was set to 5:1, while milling frequency and time were set for 15 Hz and 1 h, respectively.

Table 1. Final calcination temperature of $(Ca_{1-x}Na_x)(Al_{2-x}Si_{2+x})O_8$ plagioclase feldspars.

x	Calcined temp /K
0.0	1673
0.1	1623
0.2	1583
0.3	1553
0.4	1513
0.5	1473
0.6	1423
0.7	1393
0.8	1363
0.9	1323
1.0	1273

2.2. X-ray powder diffraction

X-ray powder diffraction (XRPD) data collections were carried out on a Bruker D8 Advance diffractometer using $CuK_{\alpha1}$ radiation ($\lambda_{K\alpha1}$ = 154.05929(5) pm) in Bragg–Brentano geometry. Data were collected at ambient condition from 10° to 130° 2θ with a step width of 0.0145° 2θ and a measurement time of 2.1 s per step. XRPD data Rietveld refinements were carried out using TOPAS V6.0 (Bruker AXS, Germany). During the Rietveld refinements, the background parameters, sample displacement, metric, and atomic positional parameters were optimized. The site occupancy factors (SOF) were determined by respective Al/Si-O distances [40]. The amorphous fraction of the samples was quantified from the degree of crystallinity (DC) as implemented in the TOPAS software. For these calculations it was assumed that the average scattering power of the crystalline fraction of the sample is identical to the scattering power of the X-ray amorphous fraction. The latter one could consist of either glassy or quantum-crystalline contributions [41]. Using the fundamental parameter approach [42], the apparent average crystallite size (ACS) was calculated from all observed X-ray reflections, which is described as $L_{Vol}(IB)$ by the TOPAS suite. $L_{Vol}(IB)$ refers to the volume-weighted mean size of the coherently diffracting domains using the integral breadth for the description of the reflection profile. The respective pseudo-Voigt profile function was deconvoluted into Gaussian and Lorentzian components, describing the ACS and the micro-strain (ε_0), respectively. The information deduced during these (classical) Rietveld refinements are, except the DC, based on the appearance of the Bragg reflections and an ideal arrangement of atoms in a unit-cell only [43].

2.3. Total scattering

Total scattering measurements data were collected in order to calculate the respective atomic pair distribution functions (PDF). Powder samples were placed in a borosilicate glass capillary of 0.5 mm outer diameter and 0.01 mm wall thickness. Thereafter, they were mounted on a Stoe STADI MP diffractometer (Stoe & Cie. GmbH, Darmstadt, Germany) in Debye–Scherrer geometry. Homogeneous irradiation of the powders was achieved with a sample spinner. Ge(111) monochromatized Mo$K_{\alpha 1}$ radiation was used for the measurement with a MYTHEN 4K (Dectris) detector from 3° to 105° 2θ and a step width of 0.015° 2θ. The measurement time per data point for pristine- and weathered samples were of 33,390 s and 57,240 s, respectively. Thus, the pristine- and weathered samples total measurement time were of 70 h and 120 h, respectively. Each measured dataset was background corrected with an empty capillary. The pair distribution function $G(r)$ was calculated using the program PDFgetX3.

2.4. Microscopy

Elemental analysis was employed on the synthesized plagioclase feldspars by scanning electron microscopy/energy dispersive X-ray (SEM/EDX) spectroscopy. SEM was carried out using a JMS-6510 (JEOL GmbH, Munich, Germany) equipped with an X-Flash 410-M detector (Bruker) for EDX spectroscopy. A small amount of powder sample was taken on conducting carbon tabs and sputtered with gold for 20 s with a JFC-1200 coater (JEOL). EDX spectra were collected using an excitation voltage of 20 kV.

2.5. Raman spectroscopy

Raman spectra were recorded on a LabRam ARAMIS (Horiba Jobin – Yvon) micro-Raman spectrometer equipped with a green laser (λ_{ex} = 532 nm and < 20 mW power). A 100x objective (Olympus) with a numerical aperture of 0.9 provides a focus spot of 721 nm diameter when closing the confocal hole to 200 µm. Each spectrum ranges between 40 cm^{-1} and 1200 cm^{-1} with a spectral resolution of approximately 1.2 cm^{-1} using a grating of 1800 grooves/mm and a thermoelectrically cooled CCD detector (Synapse, 1024 x 256 pixels).

3. Results and discussion

3.1. Synthesis

The solid-state reactions with the proposed calcination scheme leads to phase pure (> 99 wt.-%) $(Ca_{1-x}Na_x)(Al_{2-x}Si_{2+x})O_8$ plagioclase feldspar solid-solution member. Trace impurities of cristobalite SiO_2 are detected for plagioclase feldspars for $x = 0 - 0.4$, which were calcined at an elevated temperature of ≥ 1513 K. An attempt to have equal final calcination temperature lead to the formation of krotite ($CaAl_2O_4$) as a byphase. Moreover, nepheline ($NaAlSiO_4$) and gehlenite ($Ca_2Al_2SiO_7$) were attained upon calcination below the proposed final temperature within short time (≤ 24 h).

3.2. SEM/EDX

Representative SEM micrographas of synthesized plagioclase feldspars are given in **Figure 2**, showing a non-uniform distribution of agglomerated micro-particles. **Table 2** shows the complete Ca/Na and Al/Si atomic ratio obtained from the SEM/EDX analysis. Within the estimated standard deviation, the obtained Ca/Na and Al/Si values are comparable to those of the respective nominal ones, supporting the phase purity of the samples.

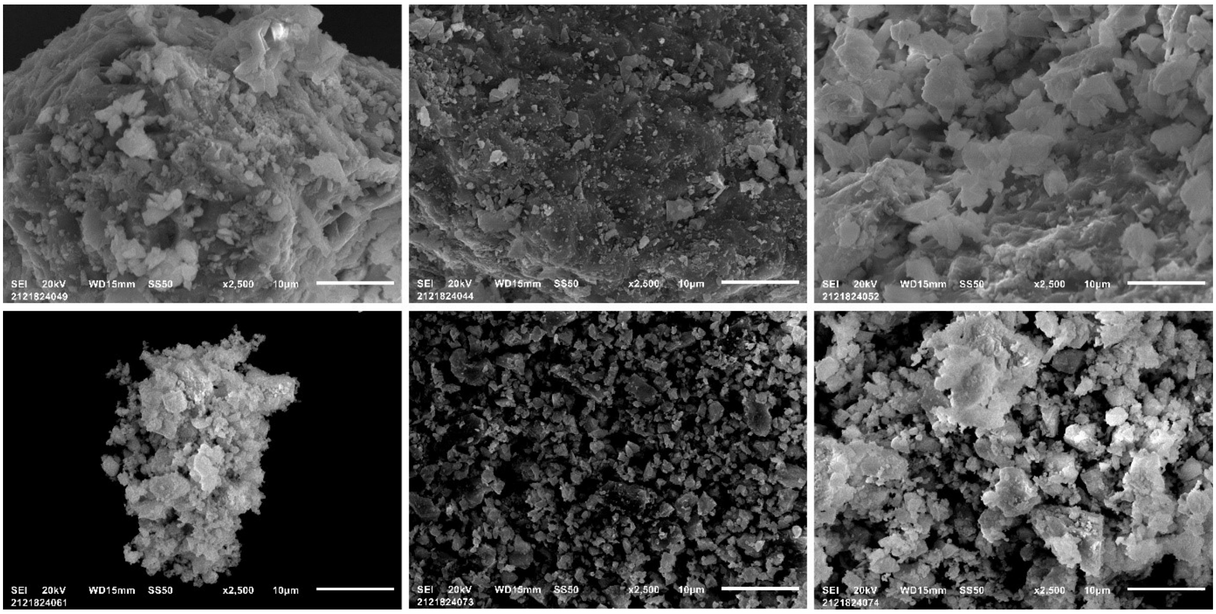

Figure 2. Micrographs of $(Ca_{1-x}Na_x)(Al_{2-x}Si_{2+x})O_8$ plagioclase feldspars with x = 0, 0.4 and 1 (left to right). The first row belongs to the pristine samples, while second row are the ball-milled ones.

Table 2. Ca/Na and Al/Si atomic ratios of $(Ca_{1-x}Na_x)(Al_{2-x}Si_{2+x})O_8$ plagioclase feldspars obtained from SEM/EDX. RV = real value, NV = nominal value. The boldfaced italic rows refer to post-milled samples.

x	**Ca/Na**		**Al/Si**	
	RV	**NV**	**RV**	**NV**
0	-	-	0.94(2)	1
0	***-***	***-***	***0.98(5)***	***1***
0.1	8.68(47)	9.00	0.86(3)	0.90
0.2	3.58(32)	4.00	0.78(5)	0.82
0.3	2.15(27)	2.33	0.76(3)	0.74
0.4	1.55(13)	1.50	0.67(2)	0.67
0.4	***1.64(19)***	***1.50***	***0.66(3)***	***0.67***
0.5	1.05(9)	1.00	0.62	0.60
0.6	0.64(7)	0.67	0.54(2)	0.54
0.7	0.44(4)	0.43	0.49(2)	0.48
0.8	0.26(3)	0.25	0.46(3)	0.43
0.9	0.13(2)	0.11	0.38(2)	0.38
1	0.00	0.00	0.34(2)	0.33
1	***0.00***	***0.00***	***0.33(2)***	***0.33***

3.3. Crystal structure

3.3.1. Plagioclase feldspar solid solution

The XRPD stack plots of all synthesized plagioclase feldspars are shown in **Figure S1** (Supplementary Information). The degree of crystallinity (DC) of the synthesized plagioclase feldspars remain between 73 wt.-% and 84 wt.-%, suggesting substantial amount of diffuse scattering contributions from the associated amorphous contents. A modified anorthite crystal structure [21] with space group $I\overline{1}$ was used for the Rietveld refinement for x = 0 - 0.4, whereas the rest of the solid solution members require a modified albite crystal data [22] with the space group $C\overline{1}$. A representative Rietveld plot of the $Ca(Al_2Si_2)O_8$ anorthite is shown in **Figure 3**. A complete list of synthesized plagioclase feldspars and their XRPD characterization results are given in **Table 3**.

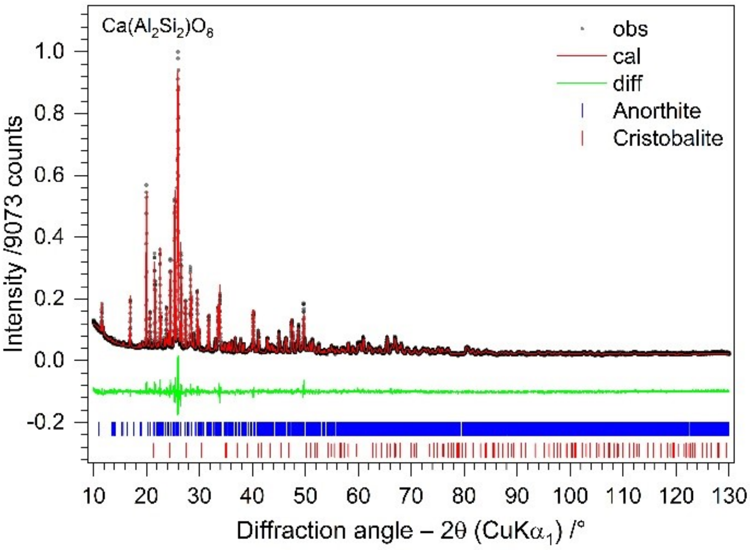

Figure 3. Representative X-ray powder data Rietveld plot of $Ca(Al_2Si_2)O_8$.

The apparent average crystallite size (ACS) and the micro-strain (ε_0) of the synthesized $(Ca_{1-x}Na_x)(Al_{2-x}Si_{2+x})O_8$ plagioclase feldspars are depicted in **Figure 4**. XRPD data Rietveld refinements indicate that anorthite $CaAl_2Si_2O_8$ crystallizes with an ACS of approximately 252(9) nm, while the other endmember albite $NaAlSi_3O_8$ with 145(4) nm. The ACS gradually decreases down to ~ 90 nm for x = 0.6 – 0.7 and slightly increases afterward to the albite endmember. Inversely, the micro-strain (ε_0) exhibits the maximum value for $x = 0.7$. The point of inflection at $x = 0.7$ for both ACS and (ε_0) are also supported by the distinctive XRPD reflections in the *2θ*-range from 27.2° to 28.2° (**Figure S1**).

Table 3. Phase quantification, average crystallite size (ACS) and micro-strain (ε_0) of $(Ca_{1-x}Na_x)(Al_{2-x}Si_{2+x})O_8$ plagioclase feldspars along with the degree of crystallinity (DC) obtained from the XRPD data Rietveld refinements. The boldfaced italic rows refer to post-milled samples.

x	Phase fraction /%		DC /%	ACS /nm	ε_0 /%
0	$CaAl_2Si_2O_8$	99	83(5)	252(9)	0.075(1)
	Cristobalite SiO_2	1	-	-	-
0	***$CaAl_2Si_2O_8$***	***99***	***78(5)***	***56(1)***	***0.044(1)***
	Cristobalite SiO_2	***1***	-	-	-
0.1	$(Ca_{0.9}Na_{0.1})(Al_{1.9}Si_{2.1})O_8$	99	81(5)	228(9)	0.084(1)
	Cristobalite SiO_2	1	-	-	-
0.2	$(Ca_{0.8}Na_{0.2})(Al_{1.8}Si_{2.2})O_8$	99	78(5)	175(6)	0.085(1)
	Cristobalite SiO_2	1	-	-	-
0.3	$(Ca_{0.7}Na_{0.3})(Al_{1.7}Si_{2.3})O_8$	99	80(5)	164(5)	0.092(1)
	Cristobalite SiO_2	1	-	-	-
0.4	$(Ca_{0.6}Na_{0.4})(Al_{1.6}Si_{2.4})O_8$	99	84(5)	122(3)	0.094(1)
	Cristobalite SiO_2	1	-	-	-
0.4	***$(Ca_{0.6}Na_{0.4})(Al_{1.6}Si_{2.4})O_8$***	***99***	***82(5)***	***63(1)***	***0.077(1)***
	Cristobalite SiO_2	***1***	-	-	-
0.5	$(Ca_{0.5}Na_{0.5})(Al_{1.5}Si_{2.5})O_8$	100	73(5)	100(3)	0.097(1)
0.6	$(Ca_{0.4}Na_{0.6})(Al_{1.4}Si_{2.6})O_8$	100	74(5)	86(2)	0.111(1)
0.7	$(Ca_{0.3}Na_{0.7})(Al_{1.3}Si_{2.7})O_8$	100	75(5)	89(3)	0.154(1)
0.8	$(Ca_{0.2}Na_{0.8})(Al_{1.2}Si_{2.8})O_8$	100	75(5)	135(5)	0.129(1)
0.9	$(Ca_{0.1}Na_{0.9})(Al_{1.1}Si_{2.9})O_8$	100	79(5)	133(4)	0.105(1)
1	$NaAlSi_3O_8$	100	81(5)	145(4)	0.090(1)
1	***$NaAlSi_3O_8$***	***100***	***79(5)***	***86(1)***	***0.066(1)***

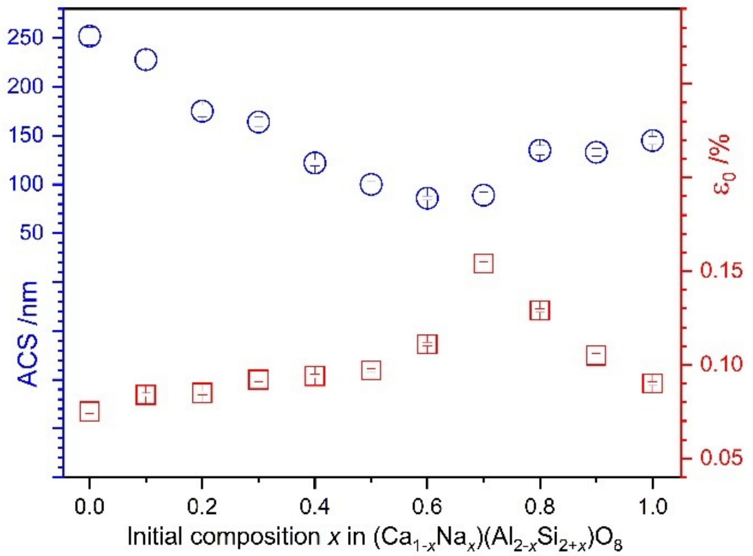

Figure 4. Changes of the average crystallite size (ACS) and micro-strain (ε_0) with respect to chemical composition x in $(Ca_{1-x}Na_x)(Al_{2-x}Si_{2+x})O_8$ plagioclase feldspars.

Figure 5 illustrates the evolution of metric parameters in changing the compositional x in $(Ca_{1-x}Na_x)(Al_{2-x}Si_{2+x})O_8$ plagioclase feldspars. The *a*-lattice parameter follows similar trend to those of ACS, i.e. $x = 0.7$ possesses the lowest value. Lattice parameter *b*, *c* and volume are in general increasing with respect to CaAl → NaSi chemical composition changes. For a triclinic crystal system, the lattice angles are important to be taken into account, mainly the γ-angle. It is a well-known function which is sensitive to the occupancy of the Si/Al within tetrahedral site [44]. In other words, the Al/Si ordering state of plagioclase feldspar can be examined by the γ-angle [45-48]. The apparent γ-angle are pronouncedly declining until $x = 0.5$ followed by moderate decrease to albite endmember. The synthesized anorthite possesses relatively lower γ of 91.125 ° comparable to the reported value of 91.280 ° [17, 21]. In contrast, synthesized albite keeps γ of 90.243(2) ° which is close to the maximum value of high albite (90.25 °) with ordering parameter of 0 [47].

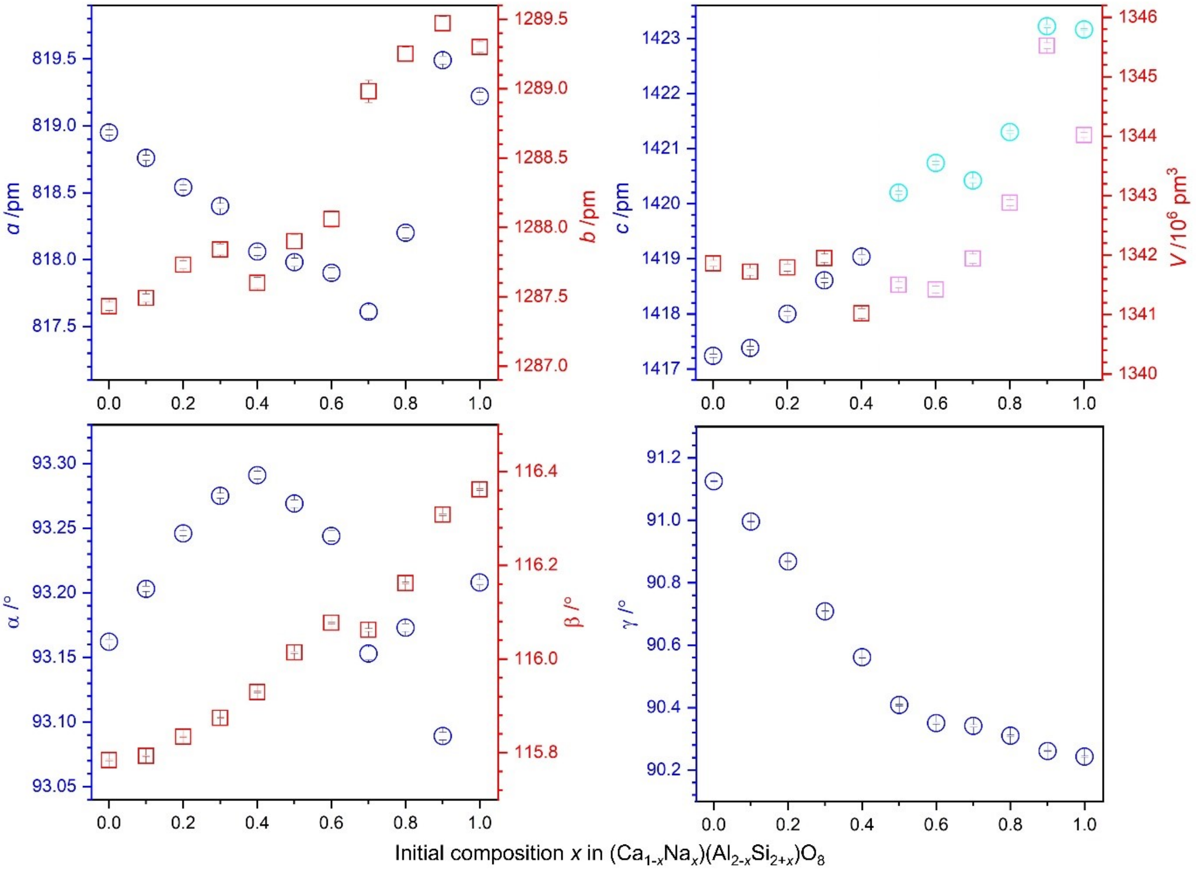

Figure 5. Evolution of the metric parameters while changing the compositional x in $(Ca_{1-x}Na_x)(Al_{2-x}Si_{2+x})O_8$ plagioclase feldspars. A modified anorthite crystal structure was used for refinement of x = 0-0.4, whereas x = 0.5-1 were refined using albite crystal data (c and V values are doubled for good comparison).

During Rietveld refinements, the average *T*-O bond length is restrained between 174 pm (correspond to Al-O) and 162 pm (correspond to Si-O) for each tetrahedral geometry, which certainly (indirectly) correlates the site occupancy factor (SOF) of Al/Si in the tetrahedral sites. That is, a longer *T*-O indicates higher Al-content and the shorter the predominance of the Si-content in the tetrahedral sites. The change of the average bond length and the Al/Si SOFs are listed in **Table 4** and **Table 5**, respectively. Note that high values of estimated standard deviations (ESDs) are obtained from refinement of the fractional atomic positions altogether. Indeed, an isomorphic substitution of Al^{3+} with Si^{4+} shows linear decreasing trend of the grand average *T*-O bond length (<*T*-O>) irrespective to the symmetry and, the cationic radius of the Na^+ and Ca^{2+} [49] in the series.

Table 4. Evolution of average bond length (*Tn*-O) in tetrahedral sites and its grand average (<*T*-O>) of synthesized $(Ca_{1-x}Na_x)(Al_{2-x}Si_{2+x})O_8$ plagioclase feldspars.

x	*T*1-O	*T*2-O	*T*3-O	*T*4-O	*T*5-O	*T*6-O	*T*7-O	*T*8-O	<T-O>
0	168.0(27)	170.1(28)	167.6(31)	168.3(29)	168.4(32)	167.4(33)	167.3(32)	167.2(32)	168.0(30)
0.1	168.7(30)	170.0(35)	166.0(32)	169.1(33)	167.9(29)	167.5(28)	168.1(32)	165.5(31)	167.8(30)
0.2	168.9(31)	169.7(32)	166.3(36)	169.8(28)	167.2(32)	166.7(34)	167.2(32)	164.4(33)	167.5(31)
0.3	168.8(32)	168.8(34)	167.9(34)	167.4(31)	166.2(32)	165.7(32)	168.0(34)	165.0(33)	167.2(32)
0.4	166.6(33)	167.6(34)	168.6(34)	166.6(35)	166.4(32)	166.4(31)	167.3(34)	165.1(35)	166.8(33)
0.5	166.7(11)	166.7(12)	166.3(13)	166.3(12)	-	-	-	-	166.5(12)
0.6	166.3(13)	166.3(12)	166.2(14)	166.1(13)	-	-	-	-	166.2(13)
0.7	166.0(14)	166.0(13)	165.9(15)	165.9(13)	-	-	-	-	165.9(14)
0.8	165.8(12)	165.6(11)	165.3(12)	165.7(12)	-	-	-	-	165.6(12)
0.9	165.2(12)	165.7(11)	165.9(12)	164.8(11)	-	-	-	-	165.4(12)
1	164.9(11)	164.8(11)	165.5(10)	164.9(11)	-	-	-	-	165.0(11)

Table 5. Site occupancy factor of Al in tetrahedral sites (*Tn*) and its average (<*T*>) of synthesized $(Ca_{1-x}Na_x)(Al_{2-x}Si_{2+x})O_8$ plagioclase feldspars.

x	*T*1	*T*2	*T*3	*T*4	*T*5	*T*6	*T*7	*T*8	<T>
0	0.503(9)	0.678(11)	0.465(9)	0.521(9)	0.532(10)	0.450(9)	0.442(8)	0.434(8)	0.503(9)
0.1	0.558(9)	0.664(13)	0.335(6)	0.595(12)	0.493(8)	0.455(8)	0.505(10)	0.295(5)	0.487(9)
0.2	0.574(11)	0.644(12)	0.357(8)	0.647(11)	0.430(8)	0.388(8)	0.430(8)	0.197(4)	0.458(8)
0.3	0.569(11)	0.571(12)	0.489(10)	0.452(8)	0.350(7)	0.307(6)	0.496(10)	0.251(5)	0.435(8)
0.4	0.380(8)	0.468(9)	0.552(11)	0.384(8)	0.364(7)	0.370(7)	0.439(9)	0.261(6)	0.402(8)
0.5	0.387(3)	0.395(3)	0.360(3)	0.360(3)	-	-	-	-	0.376(3)
0.6	0.361(3)	0.355(3)	0.350(3)	0.340(3)	-	-	-	-	0.351(3)
0.7	0.330(3)	0.331(3)	0.324(3)	0.324(3)	-	-	-	-	0.327(3)
0.8	0.315(2)	0.299(2)	0.271(2)	0.306(2)	-	-	-	-	0.298(2)
0.9	0.268(2)	0.309(2)	0.325(2)	0.236(2)	-	-	-	-	0.285(2)
1	0.243(2)	0.232(2)	0.295(2)	0.244(2)	-	-	-	-	0.253(2)

3.3.2. Milled Plagioclase Feldspars

XRPD data Rietveld refinements confirm that selective (x = 0, 0.4 and 1) post-milled $(Ca_{1-x}Na_x)(Al_{2-x}Si_{2+x})O_8$ plagioclase feldspars, as shown in **Figure 6**, possess identical phase fractions to its pristine form. **Figure S2** depicts how the further ball milling broadens the Bragg reflections along with significantly lower intensity. As a consequence, the post-milled plagioclase feldspars exhibit notable lower degree of crystallinity (DC), smaller average crystallite size (ACS), and lower micro-strain (ε_0) (**Tab. 3**). The post-milled anorthite maintains the biggest difference of DC (ΔDC ~ 5 %) compared to other plagioclase feldspars (ΔDC ~ 2 %). Alike, for the post-milled intermediate member of x = 0.4, both the ACS and the ε_0 decrease from 122(3) to 63(1) nm) and from (0.094(1) to 0.077(1) %), respectively. Rather small differences are observed for the endmember albite with ΔACS of 59(5) nm and $\Delta\varepsilon_0$ of 0.024(2) %. These results indicate for a given mechanical weathering, the microstructural features are more susceptible to the anorthite than the albite.

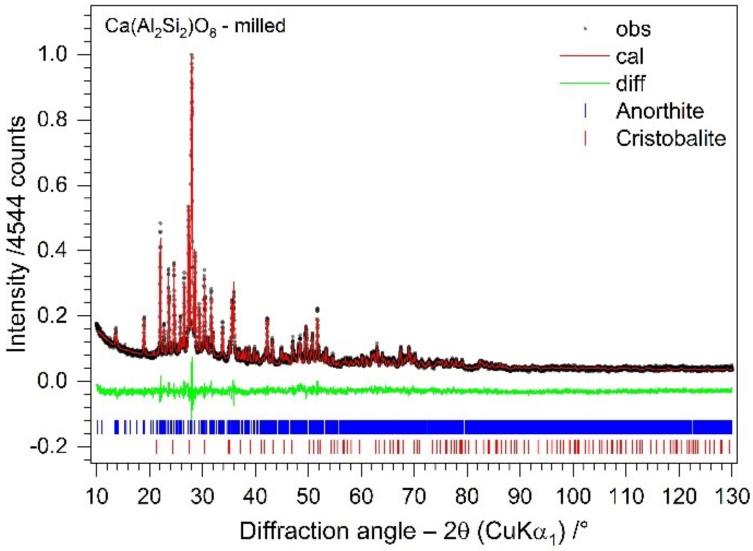

Figure 6. Representative X-ray powder data Rietveld plot of milled anorthite $Ca(Al_2Si_2)O_8$.

3.4. Pair distribution function (PDF) analysis

Total scattering measurements were carried out to further investigate the defects and local structures of the plagioclase feldspars. The analysis of the total scattering data allows extracting information from both Bragg and diffuse scattering contributions. Bragg scattering contribution can be analyzed by conventional approach in reciprocal space and provides information on the average and long-range periodic structure, whereas the diffuse scattering which mostly lies beneath the Bragg reflections [50] yields information regarding the short-range order and local structure deviations. While the observed PDFs of prior- and post-milled anorthite are almost similar, one of intermediate plagioclase feldspars for $x = 0.4$ shows notable differences such as better resolved peaks for the post-milled samples as seen in **Figure 7**. Such a greater difference is observed for the albite endmember, suggesting that the mechanical weathering create more disordered structure for plagioclase feldspar with higher Si/Al ratio.

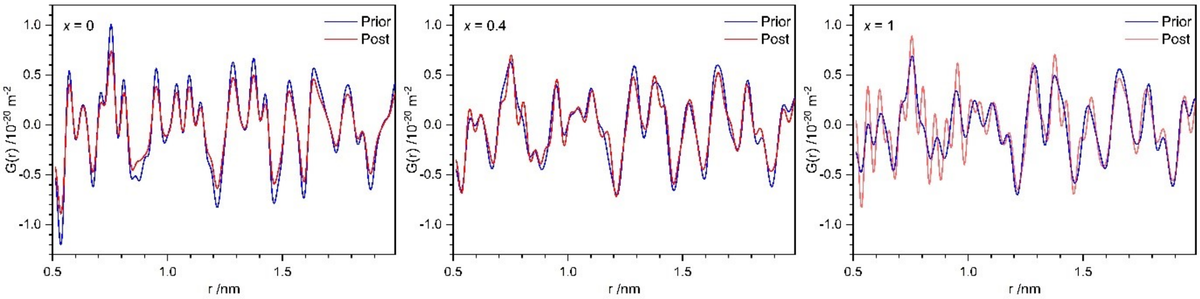

Figure 7. Observed G(r) of prior- and post-milled $(Ca_{1-x}Na_x)(Al_{2-x}Si_{2+x})O_8$ plagioclase feldspars.

Symmetry-constrained structural models obtained from Rietveld refinement of the selective plagioclase feldspars were fitted against their experimental PDFs. PDF-Rietveld refinements of the investigated plagioclase feldspars are shown in **Figure 8**. The refinements of prior-milled anorthite converged with R_{PDF} = 17 %, noticeably higher compared to that of post-milled one (R_{PDF} = 25 %). Analogically, the same behaviors are observed in albite and intermediate plagioclase feldspar of $x = 0.4$. The refinements of prior-milled intermediate feldspar and albite converged with R_{PDF} of 15 % and 23 %, whereas their post-milled possess higher R_{PDF} of 26 % and 46 %, respectively. The R_{PDF} differences between prior- and post-milled samples (ΔR_{PDF}) are increasing with respect to Si/Al ratio. The higher R_{PDF} indicates that a simple PDF-Rietveld refinement using an ideal average crystal structure model can hardly describe the local nature of the post-milled sample, in particular, for the albite endmember.

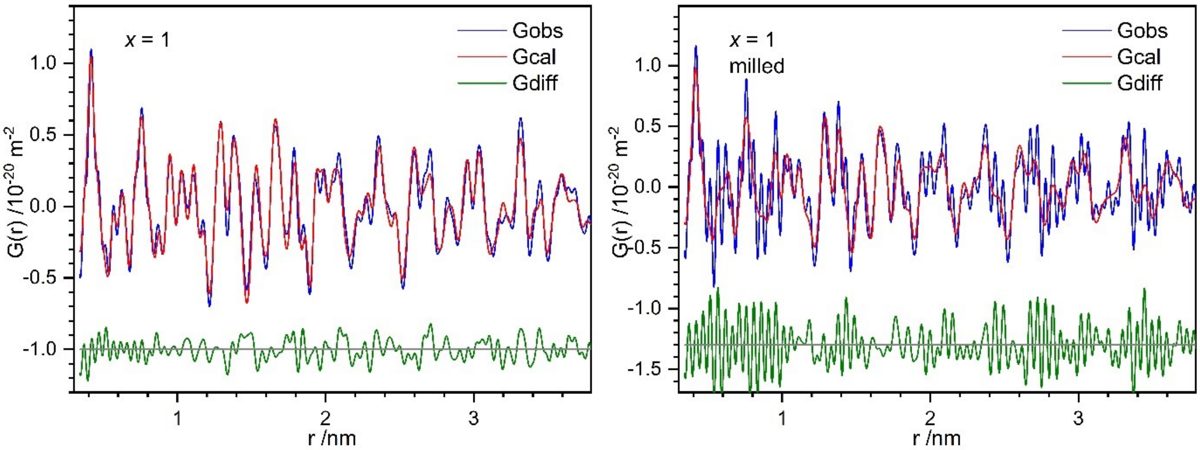

Figure 8. Representative PDF-Rietveld refinement plots of prior- (left) and post-milled albite (right).

3.5. Vibrational properties

3.5.1. Plagioclase feldpsar solid solution

Raman spectra of the synthesized $(Ca_{1-x}Na_x)(Al_{2-x}Si_{2+x})O_8$ plagioclase feldspars are shown in **Figure 9**. The changes in chemical composition have strong influence on the Raman modes. Factor group analysis predicts 39 and 78 Raman active modes [51], respectively for albite-rich ($C\bar{1}$) and anorthite-rich structure ($I\bar{1}$) samples. Peak fitting was performed for each experimental spectrum. The characteristic peak maxima along with comparative experimental reference data of anorthite [51-53] and albite [51, 52, 54] endmembers are given in **Table 6**.

Typically, the Raman spectra of plagioclase feldspar can be categorized into five regions: < 200 cm^{-1}, 200 cm^{-1} - 450 cm^{-1}, 450 cm^{-1} - 600 cm^{-1}, 600 cm^{-1} - 800 cm^{-1}, and > 800 cm^{-1}. The low-frequency region (< 200 cm^{-1}) are associated with the cage-shear modes [55, 56] with medium intensities. The second region (200 cm^{-1} - 450 cm^{-1}) show similar intensities than those in the lower region. The spectral intensity in this region is mainly contributed by the rotation–translation modes of the four-membered rings [55, 56]. The third region (450 cm^{-1} - 600 cm^{-1}) spectra can be attributed to ring-breathing modes of tetrahedra four-membered rings [52, 55, 56]. The most intense feature in the plagioclase feldspar Raman spectra is the doublet within this region. The exact position and the distance between the two peaks vary with chemical composition. For instance, the two strongest bands are observed at 486 cm^{-1} and 504 cm^{-1} in anorthite. The distance gets wider upon changes to Na-rich composition, with those of albite are observed at 476 cm^{-1} and 509 cm^{-1}. The peaks observed at fourth (600 cm^{-1} - 800 cm^{-1}) and fifth region (> 800 cm^{-1}) are correspond to deformation- and vibrational stretching modes of the tetrahedral [51, 52, 55-57], respectively. The Raman peaks within these regions tend to be relatively weak, in particular of albite-rich composition. The measured Raman spectra suggest that the phase transition occurred at $x = 0.4$, as illustrated by selective Raman peak shifts in **Figure 10.**

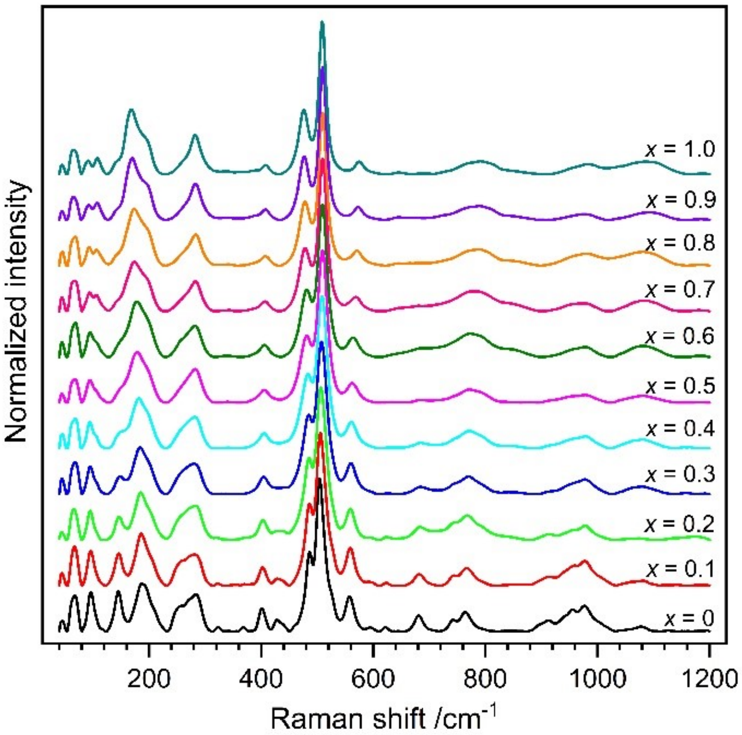

Figure 9. Raman spectra of plagioclase feldspars collected at ambient condition for $(Ca_{1-x}Na_x)(Al_{2-x}Si_{2+x})O_8$.

Table 6. Characteristic Raman frequencies of anorthite ($CaAl_2Si_2O_8$) and albite ($NaAlSi_3O_8$) in this study compared with those of literature values.

	Raman shift /cm^{-1}			
Anorthite $CaAl_2Si_2O_8$				
This work	401(1)	486(1)	504(1)	557(1)
Bersani et al. [51]	402	488	504	555
Freeman et al. [52]	402	488	505	556
Xie et al. [53]	401	487	504	558
Albite $NaAlSi_3O_8$				
This work	408(1)	476(1)	509(1)	574(1)
Bersani et al. [51]	407	478	507	578
Freeman et al. [52]	406	480	508	576
Bendel [54]	408	480	508	580

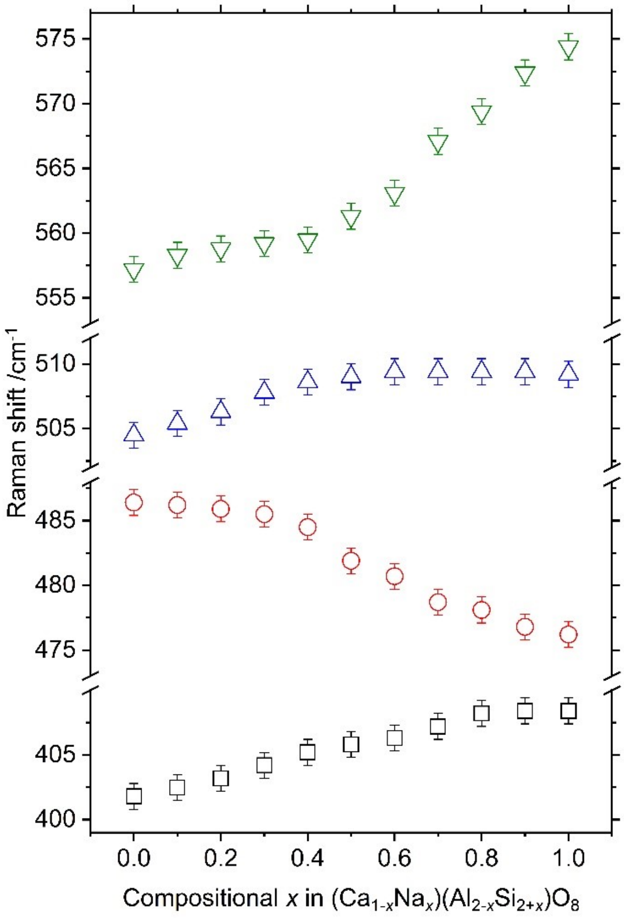

Figure 10. Selective Raman peak shifts with respect to compositional *x* in $(Ca_{1-x}Na_x)(Al_{2-x}Si_{2+x})O_8$ plagioclase feldspar.

3.5.2. Milled plagioclase feldpsars

The vibrational features of some optical phonons can be clearly distinguished between the prior- and the post-milled plagioclase feldspars as depicted in **Figure 11**. The full-width at half-maximum (*FWHM*) of the resolved peaks significantly broadens for the post-milled samples, which eventually shifts the peaks within the estimated uncertainty, as given in **Table 7**. For albite, the peak slightly broadens ($\Delta FWHM \leq 3$ cm^{-1}) accompanied by a negligible frequency shift. A greater peak broadening ($\Delta FWHM \leq 4.5$ cm^{-1}) and shifts are observed in intermediate member of $x = 0.4$. Any additional Raman peaks attributed to defects are not so far resolved within our experimental datasets. However, the noticeable peak broadening clearly indicates the differences in crystallite size and the degree of disorder [58-61] before and after the milling. In contrast, the Raman spectra of the post-milled anorthite possesses prominent difference from its pristine counterparts. In general, global red-shifts together with significant peak broadening ($\Delta FWHM \leq 16$ cm^{-1}) are observed in post-milled anorthite. The dominant two intense modes related to four-membered ring-breathing of Al/Si tetrahedra are further shifted to 482(1) cm^{-1} and 501(1) cm^{-1}, with *FWHM* of 22(1) cm^{-1} and 24(1) cm^{-1}, respectively. In addition, stronger intensities of two bands at 181(1) cm^{-1} and 257(1) cm^{-1} are clearly perceived.

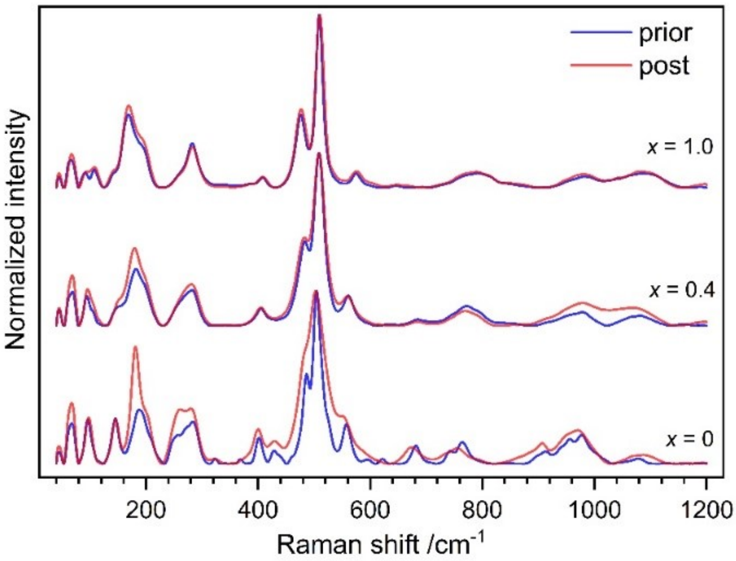

Figure 11. Raman spectra of prior- and post-milled $(Ca_{1-x}Na_x)(Al_{2-x}Si_{2+x})O_8$ plagioclase feldspars collected at ambient condition.

Table 7. Selective Raman frequencies (ω_i /cm^{-1}) and their full-width at half-maximum (*FWHM* /cm^{-1}) of the deconvoluted peak maxima of different $(Ca_{1-x}Na_x)(Al_{2-x}Si_{2+x})O_8$ plagioclase feldspars and their respective milled representatives.

Sample	ω_i	***FWHM***	ω_i	***FWHM***	ω_i	***FWHM***	ω_i	***FWHM***
				$CaAl_2Si_2O_8$				
Prior	401.1(2)	12.6(5)	486.1(2)	15.6(5)	504.5(2)	11.7(5)	556.9(2)	18.5(5)
Post-milled	***399.5(2)***	***21.4(5)***	***481.7(2)***	***22.3(5)***	***500.6(2)***	***23.7(5)***	***552.4(2)***	***34.4(5)***
				$(Ca_{0.6}Na_{0.4})(Al_{1.6}Si_{2.4})O_8$				
Prior	405.2(2)	23.4(5)	484.4(2)	24.2(5)	508.6(2)	17.9(5)	559.5(2)	24.1(5)
Post-milled	***405.0(2)***	***25.0(5)***	***484.2(2)***	***25.1(5)***	***508.8(2)***	***22.5(5)***	***558.8(2)***	***26.6(5)***
				$NaAlSi_3O_8$				
Prior	408.4(2)	12.2(5)	476.2(2)	23.5(5)	509.2(2)	12.8(5)	574.4(2)	18.8(5)
Post-milled	***408.2(2)***	***15.1(5)***	***476.3(2)***	***23.8(5)***	***509.4(2)***	***15.1(5)***	***574.7(2)***	***21.7(5)***

4. Summary and outlook

The plagioclase feldspar $(Ca_{1-x}Na_x)(Al_{2-x}Si_{2+x})O_8$ solid solution was successfully synthesized by solid-state methods. SEM/EDX analysis indicates that synthesis with the desired chemical compositions were attained. Structural analysis was performed on X-ray powder diffraction data by means of Rietveld refinements. The synthesized plagioclase feldspars exhibit degrees of crystallinity of 73 wt.-% – 84 wt.-%, suggesting substantial amount of the amorphous scattering contents. Selective plagioclase feldspar members (x = 0, 0.4 and 1) were mechanically weathered using high-energy ball milling. Implementing PDF-Rietveld refinements on X-ray Mo data indicates a complex disorder structure, in particular of post-milled albite endmember. Raman peaks broadening and frequency shifts complemented the structural features of the defective phases. This finding is an important step to characterize and quantify defect-rich Martian regolith. Further investigations involving other phases are necessary as a stepwise strategy to describe multi-phase Martian regolith. Additionally, a comparative study between radiation-weathering and the mechanical-weathering described here would be of high demand to understand the mechanism of space weathering effects.

ACKNOWLEDGEMENT

We acknowledge support by the state of Bremen within the “Humans on Mars” initiative for APF “Materials on demand” S1P3.

Reference

[1] K.A. Milam, H.Y. McSween Jr, J. Moersch, P.R. Christensen, Distribution and variation of plagioclase compositions on Mars, Journal of Geophysical Research: Planets 115(E9) (2010).

[2] A.D. Rogers, H. Nekvasil, Feldspathic rocks on Mars: Compositional constraints from infrared spectroscopy and possible formation mechanisms, Geophysical Research Letters 42(8) (2015) 2619-2626.

[3] J. Flahaut, V. Payet, F. Fueten, M. Guitreau, M. Barthez, G. Ito, P. Allemand, New Detections of Feldspar-Bearing Volcanic Rocks in the Walls of Valles Marineris, Mars, Geophysical Research Letters 50(2) (2023) e2022GL100772.

[4] M. Barthez, J. Flahaut, M. Guitreau, G. Ito, R. Pik, Understanding VNIR Plagioclase Signatures on Mars Through Petrographic, Geochemical, and Spectral Characterization of Terrestrial Feldspar-Bearing Igneous Rocks, Journal of Geophysical Research: Planets 128(8) (2023) e2022JE007680.

[5] D.L. Bish, D.F. Blake, D.T. Vaniman, S.J. Chipera, R.V. Morris, D.W. Ming, A.H. Treiman, P. Sarrazin, S.M. Morrison, R.T. Downs, C.N. Achilles, A.S. Yen, T.F. Bristow, J.A. Crisp, J.M. Morookian, J.D. Farmer, E.B. Rampe, E.M. Stolper, N. Spanovich, X-ray Diffraction Results from Mars Science Laboratory: Mineralogy of Rocknest at Gale Crater, Science 341(6153) (2013) 1238932. Doi:10.1126/science.1238932

[6] C.N. Achilles, R.T. Downs, D.W. Ming, E.B. Rampe, R.V. Morris, A.H. Treiman, S.M. Morrison, D.F. Blake, D.T. Vaniman, R.C. Ewing, S.J. Chipera, A.S. Yen, T.F. Bristow, B.L. Ehlmann, R. Gellert, R.M. Hazen, K.V. Fendrich, P.I. Craig, J.P. Grotzinger, D.J. Des Marais, J.D. Farmer, P.C. Sarrazin, J.M. Morookian, Mineralogy of an active eolian sediment from the Namib dune, Gale crater, Mars, Journal of Geophysical Research: Planets 122(11) (2017) 2344-2361. Doi:10.1002/2017je005262

[7] D.T. Vaniman, D.L. Bish, D.W. Ming, T.F. Bristow, R.V. Morris, D.F. Blake, S.J. Chipera, S.M. Morrison, A.H. Treiman, E.B. Rampe, M. Rice, C.N. Achilles, J.P. Grotzinger, S.M. McLennan, J. Williams, J.F.I. Bell, H.E. Newsom, R.T. Downs, S. Maurice, P. Sarrazin, A.S. Yen, J.M. Morookian, J.D. Farmer, K. Stack, R.E. Milliken, B.L. Ehlmann, D.Y. Sumner, G. Berger, J.A. Crisp, J.A. Hurowitz, R. Anderson, D.J. Des Marais, E.M. Stolper, K.S. Edgett, S. Gupta, N. Spanovich, M.S. Team, Mineralogy of a Mudstone at Yellowknife Bay, Gale Crater, Mars, Science 343 (2014). Doi:10.1126/science.1243480.

[8] N. Demidov, A. Bazilevskii, R. Kuz'Min, Martian soils: Varieties, structure, composition, physical properties, drillability, and risks for landers, Solar System Research 49(4) (2015) 209-225. Doi:10.1134/S0038094615040024

[9] G. Certini, S. Karunatillake, Y.-Y.S. Zhao, P.-Y. Meslin, A. Cousin, D.R. Hood, R. Scalenghe, Disambiguating the soils of Mars, Planetary and Space Science 186 (2020). Doi:10.1016/j.pss.2020.104922

[10] J.R. Michalski, P.B. Niles, Deep crustal carbonate rocks exposed by meteor impact on Mars, Nature Geoscience 3(11) (2010) 751-755. Doi:10.1038/ngeo971

[11] P.A. Bland, T.B. Smith, Meteorite Accumulations on Mars, Icarus 144(1) (2000) 21-26. Doi:10.1006/icar.1999.6253

[12] S.J. Wentworth, E.K. Gibson, M.A. Velbel, D.S. McKay, Antarctic Dry Valleys and indigenous weathering in Mars meteorites: Implications for water and life on Mars, Icarus 174(2) (2005) 383-395. Doi:10.1016/j.icarus.2004.08.026

[13] N.A. Schwadron, J.F. Cooper, M. Desai, C. Downs, M. Gorby, A.P. Jordan, C.J. Joyce, K. Kozarev, J.A. Linker, Z. Mikíc, P. Riley, H.E. Spence, T. Török, L.W. Townsend, J.K. Wilson, C. Zeitlin, Particle Radiation Sources, Propagation and Interactions in Deep Space, at Earth, the Moon, Mars, and Beyond: Examples of Radiation Interactions and Effects, Space Science Reviews 212(3) (2017) 1069-1106. Doi:10.1007/s11214-017-0381-5

[14] L.J. Steele, M.R. Balme, S.R. Lewis, A. Spiga, The water cycle and regolith–atmosphere interaction at Gale crater, Mars, Icarus 289 (2017) 56-79. Doi:10.1016/j.icarus.2017.02.010

[15] G. De Angelis, J.W. Wilson, M.S. Clowdsley, G.D. Qualls, R.C. Singleterry, Modeling of the Martian environment for radiation analysis, Radiation Measurements 41(9) (2006) 1097-1102. Doi:10.1016/j.radmeas.2006.04.032

[16] P.H. Ribbe, The Crystal Structures of the Aluminum-Silicate Feldspars, in: I. Parsons (Ed.), Feldspars and their Reactions, Springer Netherlands, Dordrecht, 1994, pp. 1-49.

[17] R. Angel, High-pressure structure of anorthite, American Mineralogist 73(9-10) (1988) 1114-1119.

[18] E.R. Myers, V. Heine, M.T. Dove, Thermodynamics of Al/Al avoidance in the ordering of Al/Si tetrahedral framework structures, Physics and Chemistry of Minerals 25 (1998) 457-464. Doi:10.1007/s002690050136

[19] V.L. Vinograd, The description of Al, Si ordering in aluminosilicates using the cluster variation method, American Mineralogist 84(3) (1999) 311-324. Doi:10.2138/am-1999-0314

[20] V.L. Vinograd, A. Putnis, A two-dimensional spin model of Al/Si order in feldspars: visualization of short-range and long-range order, European Journal of Mineralogy 13(2) (2001) 273-288. Doi:10.1127/0935-1221/01/0013-0273

[21] R.J. Angel, M. Carpenter, L. Finger, Structural variation associated with compositional variation and order-disorder behavior in anorthite-rich feldspars, American Mineralogist 75(1-2) (1990) 150-162.

[22] N. Organova, I. Marsii, N. Zakharov, V. Nasedkin, S. Borisovskii, I. Rozhdestvenskaya, T. Ivanova, Structures of the K-and Na-components of two-phase feldspar from Primorskii Krai, Crystallography Reports 44 (1999). Doi:10.1134/1.171098

[23] H. Kroll, W.F. Müller, X-ray and electron-optical investigation of synthetic high-temperature plagioclases, Physics and Chemistry of Minerals 5 (1980) 255-277. Doi:10.1007/BF00348574

[24] M.A. Carpenter, J.D.C. McConnell, Experimental delineation of the C 1⇋ I 1 transformation in intermediate plagioclase feldspars, American Mineralogist 69(1-2) (1984) 112-121.

[25] R.J. Angel, Equations of state of Plagioclase Feldspars, Contributions to Mineralogy and Petrology 146(4) (2004) 506-512. Doi:10.1007/s00410-003-0515-5

[26] M.A. Carpenter, J.D.C. McConnell, A. Navrotsky, Enthalpies of ordering in the plagioclase feldspar solid solution, Geochimica et Cosmochimica Acta 49(4) (1985) 947-966. Doi:10.1016/0016-7037(85)90310-2

[27] A. Perez, D. Daval, M. Fournier, M. Vital, J.-M. Delaye, S. Gin, Comparing the reactivity of glasses with their crystalline equivalents: The case study of plagioclase feldspar, Geochimica et Cosmochimica Acta 254 (2019) 122-141. Doi:10.1016/j.gca.2019.03.030

[28] W. Flehmig, The synthesis of feldspars at temperatures between 0–80 C, their ordering behaviour and twinning, Contributions to Mineralogy and Petrology 65(1) (1977) 1-9. Doi:10.1007/BF00373564

[29] G. Lofgren, An experimental study of plagioclase crystal morphology; isothermal crystallization, American journal of Science 274(3) (1974) 243-273.

[30] M.M. Krzmanc, M. Valant, D. Suvorov, A structural and dielectric characterization of $Na_xCa_{1-x}Al_{2-x}Si_{2+x}O_8$ (x=0 and 1) ceramics, Journal of the European Ceramic Society 25(12) (2005) 2835-2838. Doi:10.1016/j.jeurceramsoc.2005.03.151

[31] M.M. Krzmanc, M. Valant, B. Jancar, D. Suvorov, Sub-Solidus Synthesis and Microwave Dielectric Characterization of Plagioclase Feldspars, Journal of the American Ceramic Society 88(9) (2005) 2472-2479. Doi:10.1111/j.1551-2916.2005.00461.x

[32] W. Li, Z.X. Yue, F. Zhao, J. Pei, L.T. Li, Structure and Microwave Properties of $Na_xCa_{1-x}Al_{2-x}Si_{2+x}O_8$ (0< x< 0.67) Plagioclase Feldspar, Key Engineering Materials 368 (2008) 185-187. Doi:10.4028/scientific.net/KEM.368-372.185

[33] M.-C.M. Eppes, Mechanical Weathering: A Conceptual Overview, Treatise on Geomorphology 3 (2022) 30-45. Doi:10.1016/B978-0-12-818234- 5.00200-5

[34] J. López-García, V. Sánchez-Alarcos, V. Recarte, J.A. Rodríguez-Velamazán, I. Unzueta, J. García, F. Plazaola, P. La Roca, J. Pérez-Landazábal, Effect of high-energy ball-milling on the magnetostructural properties of a Ni45Co5Mn35Sn15 alloy, Journal of Alloys and Compounds 858 (2021) 158350. Doi:10.1016/j.jallcom.2020.158350

[35] W. Ashraf, A. Khan, S. Bansal, M. Khanuja, Mechanical ball milling: A sustainable route to induce structural transformations in tungsten disulfide for its photocatalytic applications, Physica E: Low-dimensional Systems and Nanostructures 140 (2022) 115152. Doi:10.1016/j.physe.2022.115152

[36] M. Bini, S. Ferrari, D. Capsoni, P. Mustarelli, G. Spina, F. Del Giallo, M. Lantieri, C. Leonelli, A. Rizzuti, V. Massarotti, Pair distribution function analysis and Mössbauer study

of defects in microwave-hydrothermal $LiFePO_4$, RSC advances 2(1) (2012) 250-258. Doi:10.1039/C1RA00525A

[37] L. Malavasi, A. Orera, P.R. Slater, P.M. Panchmatia, M.S. Islam, J. Siewenie, Local structure investigation of oxide ion and proton defects in Ge-apatites by pair distribution function analysis, Chemical Communications 47(1) (2011) 250-252. Doi:10.1039/C0CC00523A

[38] T. Proffen, S. Billinge, T. Egami, D. Louca, Structural analysis of complex materials using the atomic pair distribution function—A practical guide, Zeitschrift für Kristallographie-Crystalline Materials 218(2) (2003) 132-143. Doi:10.1524/zkri.218.2.132.20664

[39] B. Szczęśniak, S. Borysiuk, J. Choma, M. Jaroniec, Mechanochemical synthesis of highly porous materials, Materials Horizons 7(6) (2020) 1457-1473. Doi:10.1039/D0MH00081G

[40] H. Kroll, P.H. Ribbe, Determining (Al, Si) distribution and strain in alkali feldspars using lattice parameters and diffraction-peak positions; a review, American Mineralogist 72(5-6) (1987) 491-506.

[41] T.M. Gesing, M.M. Murshed, S. Schuh, O. Thüringer, K. Krämer, T. Neudecker, C.B. Mendive, L. Robben, Nano-crystalline precursor formation, stability, and transformation to mullite-type visible-light photocatalysts, Journal of Materials Science 57 (2022) 1-20. Doi:10.1007/s10853-022-07854-w

[42] J.P. Cline, D. Black, D. Gil, A. Henins, D. Windover, The Application of the Fundamental Parameters Approach as Implemented in TOPAS to Divergent Beam Powder Diffraction Data, in: P. Scardi, R.E. Dinnebier (Eds.), Extending the Reach of Powder Diffraction Modelling by User Defined Macros2010, pp. 201-219.

[43] H.M. Rietveld, A profile refinement method for nuclear and magnetic structures, Journal of applied Crystallography 2(2) (1969) 65-71. Doi:10.1107/S0021889869006558

[44] J.V. Smith, W.L. Brown, Feldspar Minerals, 2 ed., Springer Berlin, Heidelberg1988.

[45] C. Prewitt, S. Sueno, J. Papike, The crystal structures of high albite and monalbite at high temperatures, American Mineralogist 61(11-12) (1976) 1213-1225.

[46] H. Kroll, P. Ribbe, Lattice parameters, composition and Al, Si order in alkali feldspars, Feldspar mineralogy 2 (1983) 57-100.

[47] H. Kroll, P. Ribbe, Lattice parameters and determinative methods for plagioclase and ternary feldspars, Mineralogical Society of America Reviews in Mineralogy 2 (1983) 101-119.

[48] P. Ribbe, Aluminum-silicon order in feldspars: Domain textures and diffraction patterns, Mineralogical Society of America Reviews in Mineralogy 2 (1983) 21-55.

[49] R.D. Shannon, Revised effective ionic radii and systematic studies of interatomic distances in halides and chalcogenides, Acta crystallographica section A: crystal physics, diffraction, theoretical and general crystallography 32(5) (1976) 751-767. Doi:10.1107/S0567739476001551

[50] T. Egami, S.J. Billinge, Underneath the Bragg peaks: structural analysis of complex materials, Elsevier2003.

[51] D. Bersani, I. Aliatis, M. Tribaudino, L. Mantovani, A. Benisek, M.A. Carpenter, G.D. Gatta, P.P. Lottici, Plagioclase composition by Raman spectroscopy, Journal of Raman Spectroscopy 49(4) (2018) 684-698. Doi:10.1002/jrs.5340

[52] J.J. Freeman, A. Wang, K.E. Kuebler, B.L. Jolliff, L.A. Haskin, Characterization of natural feldspars by Raman spectroscopy for future planetary exploration, The Canadian Mineralogist 46(6) (2008) 1477-1500. Doi:10.3749/canmin.46.6.1477

[53] T. Xie, G.R. Osinski, S.R. Shieh, Raman study of shock effects in lunar anorthite from the Apollo missions, Meteoritics & Planetary Science 56(9) (2021) 1633-1651. Doi:10.1111/maps.137281633

[54] V. Bendel, B.C. Schmidt, Raman spectroscopic characterisation of disordered alkali feldspars along the join $KAlSi_3O_8$-$NaAlSi_3O_8$: application to natural sanidine and anorthoclase, European Journal of Mineralogy 20(6) (2008) 1055. Doi:10.1127/0935-1221/2009/0021-1856

[55] V. Fuertes de la Llave, A. del Campo, J. Fernández, E. Enríquez, Structural insights of hierarchically engineered feldspars by confocal Raman microscopy, Journal of Raman Spectroscopy 50(5) (2019) 741-754. Doi:10.1002/jrs.5556

[56] T. Xie, G.R. Osinski, S.R. Shieh, Raman study of shock features in plagioclase feldspar from the Mistastin Lake impact structure, Canada, Meteoritics & Planetary Science 55(7) (2020) 1471-1490. Doi:10.1111/maps.13523

[57] S.K. Sharma, B. Simons, H. Yoder, Raman study of anorthite, calcium Tschermak's pyroxene, and gehlenite in crystalline and glassy states, American Mineralogist 68(11-12) (1983) 1113-1125.

[58] N. Islam, A. Pradhan, S. Kumar, Effects of crystallite size distribution on the Raman-scattering profiles of silicon nanostructures, Journal of Applied Physics 98 (2005) 024309-024309. Doi:10.1063/1.1980537

[59] V. Swamy, B.C. Muddle, Q. Dai, Size-dependent modifications of the Raman spectrum of rutile TiO_2, Applied Physics Letters 89(16) (2006) 163118. Doi:10.1063/1.2364123

[60] G. Gouadec, P. Colomban, Raman Spectroscopy of nanomaterials: How spectra relate to disorder, particle size and mechanical properties, Progress in crystal growth and characterization of materials 53(1) (2007) 1-56. Doi:10.1016/j.pcrysgrow.2007.01.001

[61] W. Demtröder, Laser Spectroscopy: Vol. 1: Basic Principles, Springer Berlin Heidelberg, 2008.

Supplementary information

Synthesis and characterizations of plagioclase feldspars $(Ca_{1-x}Na_x)(Al_{2-x}Si_{2+x})O_8$: mechanical weathering relevant to Martian regolith

Md. Izzuddin Jundullah Hanafi, M. Mangir Murshed*, Lars Robben, Thorsten M. Gesing

University of Bremen, Institute of Inorganic Chemistry and Crystallography, Leobener Straße 7, D-28359 Bremen, Germany

University of Bremen, MAPEX Center for Materials and Processes, Bibliothekstraße 1, D-28359 Bremen, Germany

*Corresponding author: murshed@uni-bremen.de, phone: +49 (0)421 218 63144

ORCID:

MIJH: 0009-0005-7842-6751

MMM: 0000-0002-9063-372X

LR: 0000-0002-0534-9573

TMG: 0000-0002-4119-2219

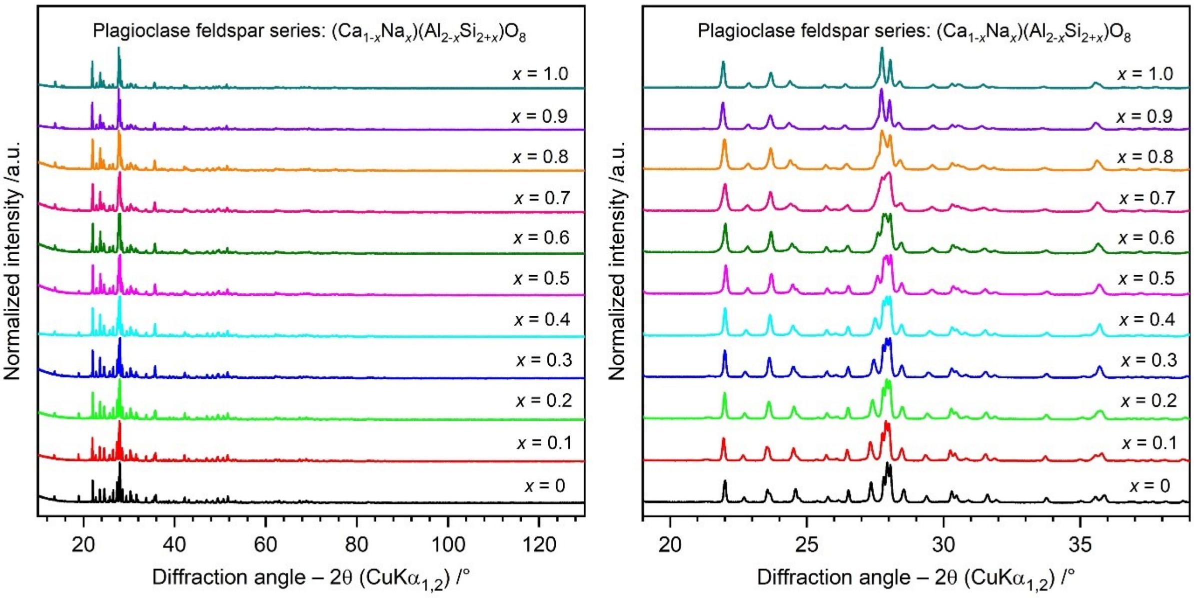

Figure S1. X-ray powder diffraction patterns of $(Ca_{1-x}Na_x)(Al_{2-x}Si_{2+x})O_8$ plagioclase feldspars.

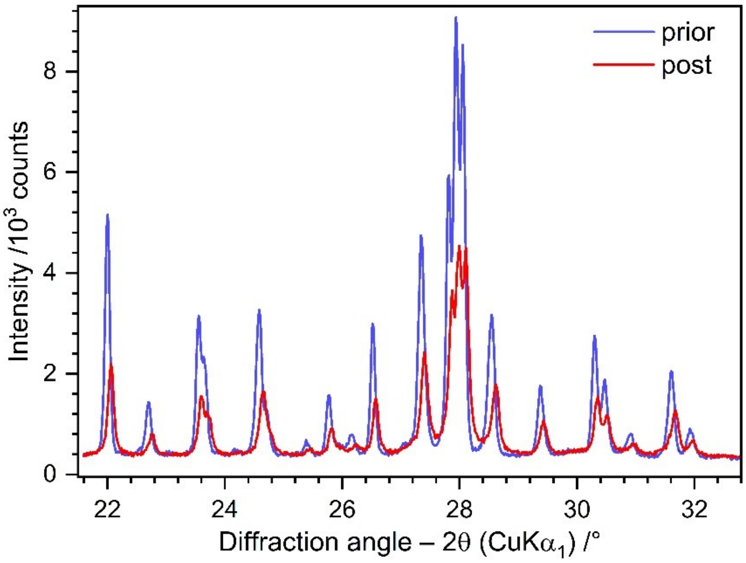

Figure S2. X-ray powder diffraction patterns of prior- and post-milled anorthite ($CaAl_2Si_2O_8$).

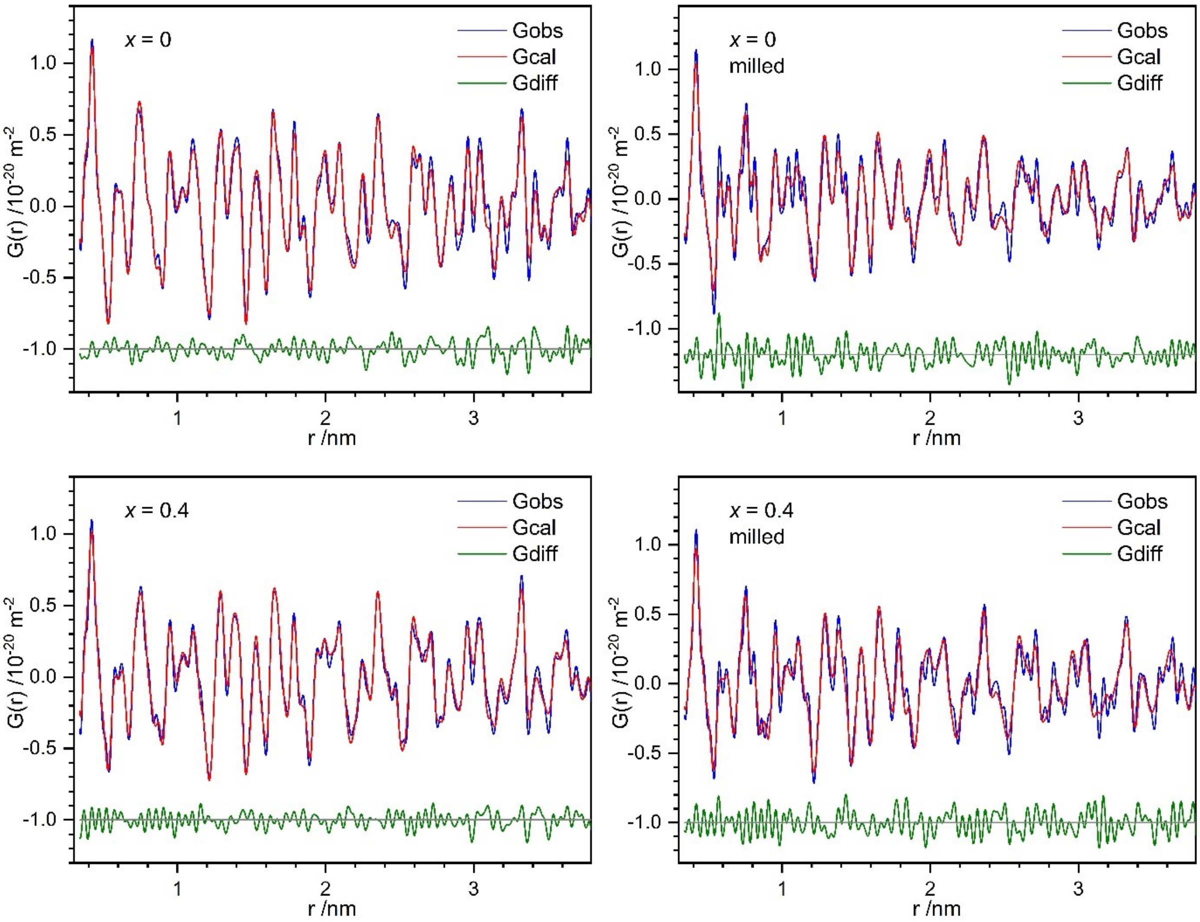

Figure S3. PDF-Rietveld refinement plots of prior- (left) and post-milled (right) $(Ca_{1-x}Na_x)(Al_{2-x}Si_{2+x})O_8$ plagioclase feldspars.

Chapter 6 – Outlook

Within the scope of this thesis, two solid solutions of Martian regolith phase constituents, $(Mg_{1-x}Fe_x)_2SiO_4$ olivines and $(Ca_{1-x}Na_x)(Al_{2-x}Si_{2+x})O_8$ plagioclase feldspars were successfully synthesized. Additionally, selective defect-rich structure investigations were conducted to study mechanical weathering process occurred on Mars. The samples are characterized using X-ray powder diffraction Rietveld refinement, X-ray total scattering pair distribution function analysis, SEM/EDX, Raman- and UV/Vis spectroscopy.

Mechanochemical synthesis of $(Mg_{1-x}Fe_x)_2SiO_4$ olivine solid solution (**Chapter 3**) was carried out to cover the wide range of olivine composition on Mars. The synthesized olivines exhibit relatively low amount of the amorphous scattering contents with DC of 92 wt.-% – 97 wt.-%. Nevertheless, synthesis of high-amorphous olivine phases would mimic closer condition to the real Martian regolith and provide better understanding of their crystal chemical properties. Moreover, the third olivine endmember in the form of tephroite (Mn_2SiO_4) might also be present despite of their small fraction on Martian regolith. Additional synthesis of their combination series, i.e. full solid solution of $(Mg_{1-x}Mn_x)_2SiO_4$ and $(Fe_{1-x}Mn_x)_2SiO_4$ olivines would expand the data base for complete preparation prior humans' mission on Mars.

Investigation on the defect-rich and highly-amorphous Mg_2SiO_4 (forsterite, **Chapter 4**) was fulfilled to study mechanical weathering impact using high-energy ball mill. The X-ray powder diffraction data and vibrational Raman spectroscopy indicated the presence of high-amorphous and disorder structure. PDF-Rietveld refinement confirmed the existence of the defect-rich structure. Systematic study involving greater range of defect concentration in forsterite would be of interesting future studies. That is, extensive research to explore possibility of other defect-rich structural motifs with lower formation energy.

The plagioclase feldspar $(Ca_{1-x}Na_x)(Al_{2-x}Si_{2+x})O_8$ solid solution (**Chapter 5**) was successfully synthesized by solid-state methods. The synthesized plagioclase feldspars exhibit substantial amount of the amorphous scattering contents with DC of 73 wt.-% – 84 wt.-%. Due to similar X-ray scattering power of Al and Si, the Al/Si and Ca/Na site occupancy factors (SOFs) were determined from the grand average Al/Si-O bond lengths within their tetrahedral sites. While this method is able to provides reasonable refinements and structure fittings of the series, the structure solution remains open for mechanically-weathered samples, in particular of the high standard deviation yielded. Thus, neutron diffraction on each member of the $(Ca_{1-x}Na_x)(Al_{2-x}Si_{2+x})O_8$ series and selective mechanically-weathered plagioclase feldspar would clarify this issue and provide more reliable refinements.

Overall, these findings are important starting point to characterize and quantify defect-rich Martian regolith. In contrast to naturally occurring minerals, the synthesized samples have an advantage of providing high-purity materials (≥99 %) for further experiments of extraterrestrial metal fabrications on Mars. Further investigations involving a larger number of phases are necessary as a stepwise strategy to structurally describe multi-phase Martian regolith.

In addition, a study of radiation-induced defects would complement the research. Selective pristine and post-mechanical weathering samples should be irradiated with proton to simulate billion years of radiation damage. The samples will be analyzed again with multi-tool structural and spectroscopic characterization techniques. Comparative results between mechanical-, radiation-, and total-weathering process would be of high demand to understand the mechanism of space weathering effects. The overall simulation would mimic the Martian weathering process, leading to representative samples to shed light on the feasibilities of the ISRU.